ISSN 1590-8844
Vol. 10 No 01
2009

International Journal of Mechanics and Control

Editor: Andrea Manuello Bertetto

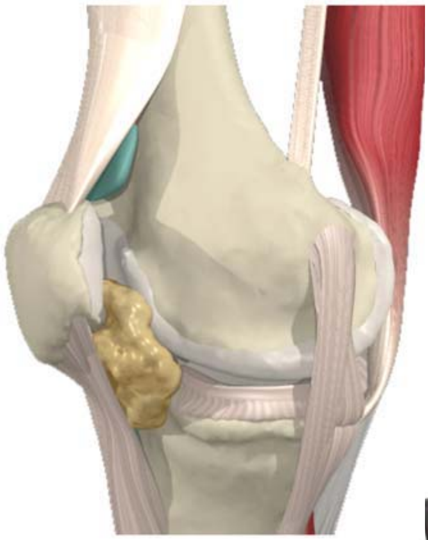

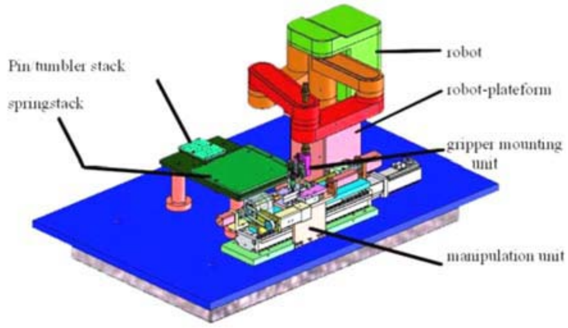

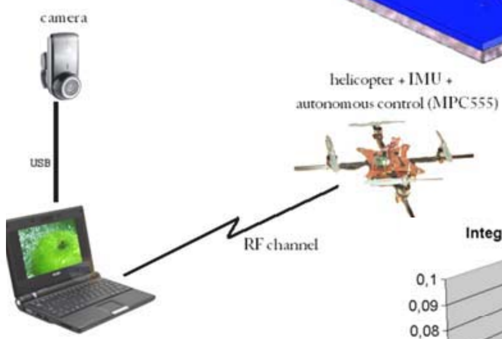

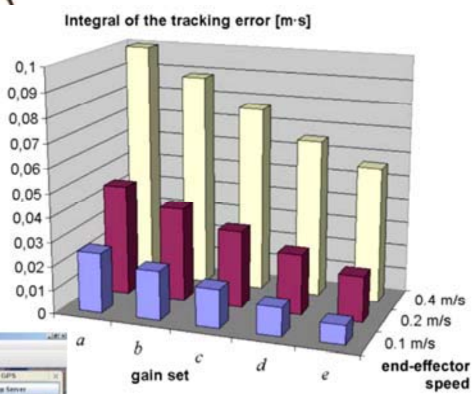

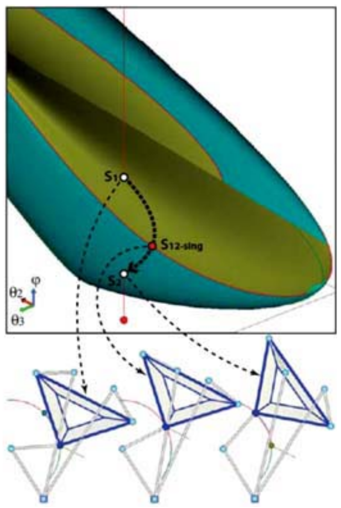

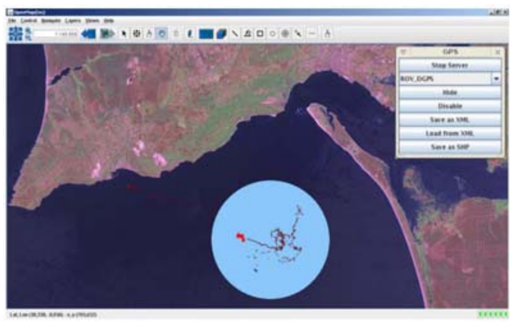

LIBRERIA EDITRICE UNIVERSITARIA
LEVROTTO & BELLA
TORINO

Official Torino Italy Court Registration
n.5390, 5th May 2000

Deposito presso il Tribunale di Torino
numero 5390 del 5 maggio 2000
Direttore responsabile:
Andrea Manuello Bertetto

ISSN 1590-8844
International Journal of Mechanics and Control, Vol. 10, No. 01, 2009

PREFACE

The RAAD08, International Workshop on Robotics in Alpe-Adria-Danube Region has been the 17-th event of a series that has been started in 1992 as a conference activity with family character mainly for promoting Robotics topics in Central Europe as in Alpe-Adria-Danube Region. The RAAD Workshop is held every year in a different country of the Region. The 2008 RAAD Workshop has come to Technical University of Marche Region, Italy, in May 2008

RAAD Workshop aim was decided at the funding meeting in 1992 as: a conference stimulating integration between communities from Mechanical Engineering and Automation; a forum for facilitating contacts among research people, professionals, and students; and a match conference for communities from IFToMM (International Federation for the Promotion of Mechanism and Machine Science) and IEEE (the Institute of Electrical and Electronics Engineers) in Central Europe. Thus, since 2003 IFToMM has supported the RAAD events with a patronage too.

The aim of RAAD Workshop is to bring together researchers, industry professionals, and students from the broad ranges of disciplines referring to Mechatronics and Robotics, in an intimate, collegial, and stimulating environment. Nevertheless, RAAD Workshops have received an increased attention, as can be seen by the fact that the Proceedings contain contributions by authors even from all around the world.

Beside publication of the proceedings, that since few year are distributed as CD volumes, special issues in journal have been published occasionally. Since this year it has been decided that at each RAAD Workshop a selection of paper will be published in a special issue of this journal with the aim to give more visibility to very good results. This special Journal issue has been obtained as a result of a second review process and selection, but all the papers that have been accepted for RAAD08 are of good quality with interesting contents suitable for Journal publication and it has been hard to decided for the selection. Perhaps some papers did not receive due attention for this special issue from reviewers but we hope that the authors have decided for a submission to a journal yet.

I would like to express grateful thanks to the members of ISC, the International Scientific Committee for RAAD Workshops and AB, the Advisory Board for co-operating enthusiastically for the success of the RAAD08 event and this special issue. Since 2007 RAAD the leading group has been organized in the two bodies ISC and AB in order to have ISC as a group of people directly responsible for the RAAD planning and organization of RAAD events, and to keep the advices of people who were very active in past RAAD Workshops, in AB both for promoting the community and RAAD events.

The current composition is the following:

- International Scientific Committee (ISC)
G. Belforte, Polytechnic of Turin, Italy
T. Borangiu, Technical University of Bucharest, Romania
M. Ceccarelli, University of Cassino, Italy (Coordinator)
K. Dobrovodsky, Academy of Sciences, Slovakia
M.-W. Han, Technical University Vienna, Austria
N. Ivanescu, Technical University of Bucharest, Romania
K. Jezernik, University of Maribor, Slovenia
Z. Kolíbal, Brno University of Technology, Czech Rep.
I.J. Rudas, Budapest Technical University Hungary

- Advisory Board (AB)
J.F. Bito, Centre of Robotics and Automation, Hungary
P. Kopacek, Technical University Vienna, Austria
B. Heimann, Technical University Hannover, Germany
J. Lenarčič, Jožef Stefan Institute, Ljubljana, Slovenia
D. Noe, University of Ljubljana, Slovenia
A. Rovetta, Polytechnic of Milan, Italy
G. Schmidt, Technical University Munich, Germany

The success of the past RAAD Workshops has enlarged the RAAD community but ISC and AB has worked together with the Organizers of the event to ensure good quality of the paper presentations and to maintain the peculiar character of the RAAD events, as in friendly environment permitting to exchange information and experiences and to start new collaborations.

I will like to thank prof Massimo Callegari of Technical University of Marche Region for having organized a very successful 2008 RAAD Workshop and the publisher with Editorial staff of this journal for accepting and helping the publication of this special issue, since the early step in 2008.

University of Cassino, February 2009.

Prof. Marco Ceccarelli
Coordinator of the International Scientific Committee for RAAD Workshops

ISSN 1590-8844
International Journal of Mechanics and Control, Vol. 10, No. 01, 2009

Dear reader,

I had the pleasure to chair the 17th International Worskhop on Robotics in Alpe-Adria-Danube Region that took place in Ancona from September 15th to 17th, 2008: now I am happy to introduce this special issue of the International Journal of Mechanics and Control entirely devoted to present a selection of the best papers that have been presented at the Conference.

In RAAD08 we have received contributions from 15 different countries and, after a careful revision of the draft papers by 2-4 reviewers, we organized the 66 accepted papers into 14 technical sessions. The variety of topics of the works that have been submitted gives a very interesting view of the activities in research, teaching, and application of Robotics in the Alpe-Adria-Danube Region: humanoids & walking robots; robots in medicine and surgery; robot sensing and control; automation and industrial robotics; robot kinematics and dynamics; mobile robotics; grasping, handling and intelligent manipulation; service robots; mechatronics and motion control; marine robotics; education and training in robotics; towards micro and nano-robots; robot vision. It can be seen by such list that both conventional areas of research and new breakthrough topics are covered, with contributions by universities and research institutions as well as by industrial world.

A few papers among the best research works presented the Conference have been recently selected to be published in this issue of JoMaC and have been therefore revised by their authors and evaluated by the independent reviewers of the journal: in this way I am sure the articles you are going to read are a window on current cutting-edge research in robotics and automation.

Before closing these few lines of presentation, just let me express my gratitude to all the Raadists that presented the results of their valuable researches to the Workshop and of course a special thank goes to the Authors of the present articles, that worked hard twice to have their contributions fit to the standards of this International Journal. In the end I cannot forget the Reviewers of both RAAD08 and JoMaC for their timely evaluations of the papers, that greately contributed to enhancing the quality of the Workshop and of this special issue.

M. Callegari

Massimo Callegari
Chair RAAD 2008

International Journal of Mechanics and Control

Editor: **Andrea Manuello Bertetto**

Honorary editors: **Guido Belforte**
Kazy Yamafuji

General Secretariat: **Elvio Bonisoli**

The Journal is addressed to scientists and engineers who work in the fields of mechanics (mechanics, machines, systems, control, structures). It is edited in Turin (Northern Italy) by Levrotto&Bella Co., with an international board of editors. It will have not advertising.
Turin has a great and long tradition in mechanics and automation of mechanical systems. The journal would will to satisfy the needs of young research workers of having their work published on a qualified paper in a short time, and of the public need to read the results of researches as fast as possible.
Interested parties will be University Departments, Private or Public Research Centres, Innovative Industries.

Aims and scope

The *International Journal of Mechanics and Control* publishes as rapidly as possible manuscripts of high standards. It aims at providing a fast means of exchange of ideas among workers in Mechanics, at offering an effective method of bringing new results quickly to the public and at establishing an informal vehicle for the discussion of ideas that may still in the formative stages.

Language: English

International Journal of Mechanics and Control will publish both scientific and applied contributions. The scope of the journal includes theoretical and computational methods, their applications and experimental procedures used to validate the theoretical foundations. The research reported in the journal will address the issues of new formulations, solution, algorithms, computational efficiency, analytical and computational kinematics synthesis, system dynamics, structures, flexibility effects, control, optimisation, real-time simulation, reliability and durability. Fields such as vehicle dynamics, aerospace technology, robotics and mechatronics, machine dynamics, crashworthiness, biomechanics, computer graphics, or system identification are also covered by the journal.

Please address contributions to

Prof. Guido Belforte
Prof. Andrea Manuello Bertetto
PhD Eng. Elvio Bonisoli

Dept. of Mechanics
Technical University - Politecnico di Torino
C.so Duca degli Abruzzi, 24.
10129 - Torino - Italy - E.C.

www.jomac.it
e_mail: jomac@polito.it

Subscription information

Subscription order must be sent to
the publisher:

Libreria Editrice Universitaria
Levrotto&Bella
2/E via Pigafetta – 10129 Torino – Italy

www.levrotto-bella.net
e_mail: info@levrotto-bella.net
tel. +39.011.5097367
+39.011.5083690
fax +39.011.504025

ISSN 1590-8844
International Journal of Mechanics and Control, Vol. 10, No. 01, 2009

A THREE-STEP PROCEDURE FOR THE MODELLING OF HUMAN DIARTHRODIAL JOINTS

Riccardo Franci* Vincenzo Parenti-Castelli* Nicola Sancisi*

* Department of Mechanical Engineering, University of Bologna, Italy

ABSTRACT

The basic role played by models of the diarthrodial joints in surgery, in pre-surgical planning and in prosthesis design has been widely stressed in the literature. Different approaches have been proposed to highlight the role of the main anatomical structures of the joint. Most models are based on in vivo measurements which, however, are difficult to perform. This paper presents a sequential procedure based on three steps for the modelling of a joint. At each step a more and more complicated model of the joint is provided. Starting with a limited number of the passive anatomical structures of the joint (ligaments, for instance), all the structures, both passive and active (muscles), are incorporated in the final model step by step. This procedure makes it possible to progressively gain a deeper understanding of each structure of the joint. Examples of application to the knee and ankle joints are finally reported.

Keywords: diarthrodial joints, knee, ankle, models, sequential approach

1 INTRODUCTION

The study of human diarthrodial joints has involved efforts of an impressive number of researchers. Basic studies focussed on experimental measurements of the relative motion of the main bones of the joint under investigation. The measurements performed in vitro (cadaver specimens) or in vivo (patients and volunteers) have the following various purposes:

- to test and validate measurement techniques [1, 3] as well as define standardization of diagnosis and rehabilitation procedures;
- to obtain a deeper knowledge on the behaviour of these joints which exhibit a quite complicated anatomical structure [12, 13];
- to validate and improve mathematical models of the articulations [14, 22].

Mathematical models are among the most powerful tools for the functional analysis of such a complicated biological structures and represent helpful tools for the solution of important issues such as, for instance:

- definition of surgical and diagnostic procedures for joint disorders caused by injuries or diseases;
- designing prosthesis devices [4, 9];
- assessment of the role of the joint biological structures in the joint characteristics in normal and pathological conditions [3];

Planar and spatial mathematical models of joints have been presented in the literature [11, 14, 22]. Planar models proved to be of great usefulness. However, for many joints they cannot take into account some complicated and subtle phenomena involved in the joint motion since most of them intrinsically have a three-dimensional motion.

The models presented in the literature are based on two different approaches. The first one models the biological structures of the joint connections such as ligaments, muscles, and articular surfaces by means of linear and non-linear elastic and dumping elements, lumped or distributed parameters, and finds the relative motion of the main bones by solving the equations of motion of the resulting model [1, 17, 21, 23]. The main bones are allowed to have up to six degrees of freedom (DOF) in their relative motion which finally depends on the external forces applied to the joint and on the elastic and dumping characteristics of the joint connecting structures. These models are computationally demanding but are also suitable to simulate the dynamic behaviour of the joint in addition to its kinematic and static behaviour.

Contact author: Vincenzo Parenti-Castelli

Viale Risorgimento 2, 40136, Bologna, Italy.
E-mail: vincenzo.parenti@unibo.it
URL: http://www.diem.ing.unibo.it/grab/

The second approach, instead, models the joint as a linkage or an equivalent mechanism [14, 15, 22] whose geometry is based, as much as possible, on the joint's anatomical structures. The motion of the mechanism predicts the relative motion of the joint's main anatomical structures. These mechanisms are suitable to analyze the passive motion of the joint, that is, the motion of the joint under virtually unloaded conditions (no external loads), which is believed to have a great relevance for a deeper understanding of the joint kinematics [9]. Indeed, with regard to the knee joint "the actual motion patterns of the human knee joint depend on a combination of its passive motion characteristics and the external loads" [3].
Examples of equivalent mechanisms with one or more DOFs have been proposed in the literature to account for the joint passive motion. Most of them are planar mechanisms and only a few are spatial. For example, one of the first spatial equivalent mechanism (with one DOF) for the study of the knee passive motion was presented in [22]. This model combined a relative simplicity with the ability to take the tibia-femur spatial motion into good account.
The authors of this paper started working on this field by basing their research on the O'Connor approach [22]. Much work was done mainly on the modelling of passive motion of the human knee and the ankle joints. Remarkable results were obtained and presented in [7, 8, 18].
Passive motion involves only some anatomical structures, i.e. the main passive structures of the joint. Instead, the modelling of kinetostatic and dynamic behaviour of the joints involves all the anatomical structures, that comprise both passive (ligaments, tendons, and bones) and active (muscles) structures. In this case, ligament elasticity is necessarily involved, thus making the models mathematically more complicated since model elements would have a subtle relation with the anatomical structures. This would make the outcomes of the models difficult to interpret and the model itself less useful to surgeons and to prosthesis designers.
In this context a new approach has been devised and presented here in a structured form for the kinematic, kinetostatic and dynamic modelling of diarthrodial joints. The approach makes it possible to consider all the anatomical structures of a joint, both the passive and the active ones, making their role in the kinematic and kinetostatic-dynamic behaviour of the joint itself evident. The approach relies upon some basic hypotheses and is based on three main steps from which, in order, three joint models of increasing complexity can be obtained. More precisely, the first step models the joint passive motion, the second step takes into account the kinetostatic behaviour of the joint under external loads, and the third step considers the (dynamic) influence of the active elements such as the muscles.
The following sections are organized as follows: the general presentation of the proposed approach is presented in section 2. Section 3 exhibits some application of the proposed approach to some joints, and the corresponding results of the simulation and measurements. Finally, some conclusions are reported.

2 NEW SEQUENTIAL APPROACH

The new sequential approach proposed relies upon experimental measurements and mechanical models of the articulations. Three different steps are involved in the whole process. Each step refers to a model: each model is an evolution of the model obtained at the previous step. A process of optimization makes it possible to define the main geometric and structural parameters of the model at each step. The three steps therefore provide three different models, which for convenience are called M1, M2 and M3 respectively.
All models rely upon two basic rules:

- once a parameter has been identified at a particular step, it is left unmodified at the next steps;
- parameters identified at each step must be chosen in a way that they do not alter the results obtained at the previous steps.

These two rules guarantee that the results obtained at each step do not worsen those already obtained at previous steps and, most importantly, they make it possible to choose new parameters without violating possible anatomical constraints satisfied at previous steps.
In this sense, the proposed sequential approach is substantially an inductive procedure that starts from the definition of a simple model that can replicate the behaviour of the articulation under very strict conditions (with only some basic anatomical structures considered). This preliminary model is then enriched, at each step, by adding further anatomical structures which make the model progressively more complex, i.e. more sophisticated, in order to obtain a more generalized model which can replicate the behaviour of the joint under less restrictive conditions.
The three models identified at each step are the following:

- **STEP 1** (M1 model). This is the model of the passive motion of the articulation. It refers to the joint's main anatomical structures which are involved during the motion of the joint under virtually unloaded conditions. In practice they are the passive structures that guide the motion of the joint: in most cases they are represented by bones which are in mutual contact during the motion and ligaments that interconnect the bones. Since no external force and moment are considered, the passive structures involved do not normally provide forces. This allows the assumption that all structures behave as rigid bodies. Thus, the M1 model can be represented by an equivalent planar or spatial mechanism having rigid bodies. The geometric parameters of the models are identified by an optimization process based on in vivo measurements of the joint passive motion.
- **STEP 2** (M2 model). The M2 model comprises the M1 model with the addition of the remaining passive structures, the ones that are not considered in the previous step. External forces and moments are

considered and all the passive structures involved (both those of the M1 model and those added at this step) are now considered as elastic or viscoelastic structures. The physical model no longer has the feature of a rigid body equivalent mechanism, but it incorporates elastic/viscoelastic elements. Once again, the model's geometric and structural parameters are identified by mean of an optimization procedure based on experimental data collected by in vivo experiments. The identification procedure is performed by satisfying the rules of the sequential approach.

- **STEP 3** (M3 model). The M3 model comprises the M2 model with the addition of all the active joint structures, i.e. mainly all muscles involved in the motion of the joint. The physical model has similar rigid-elastic/viscoelastic features to the M2 model but incorporates dynamic loads (inertia). Once again, an optimization procedure makes it possible to identify the remaining geometrical and structural parameters of the model.

At each step it is therefore possible to identify the role of the added structures.

In conclusion, the M1 model allows the study of the joint passive motion which mainly comprises kinematic concepts; in fact, no forces are involved. The role of the main passive structures, such as ligaments and bones, which guide the motion of the joint under no external load is highlighted.

The M2 model studies the motion and the stiffness of the joint under external loads. It allows considerations on the joint stability, to understand the role that both the main and the secondary passive structures play on it. The model, in practice, is represented by a mechanical system with both rigid and elastic/viscoelastic links which allow kinematic, static and kinetostatic analyses to be performed.

The M3 model is the most complete and complex model: it incorporates all the structures of the joint and allows kinematic, static and dynamic analyses to be performed. The role of the active structures such as the muscles is highlighted by this model.

Each model has its own advantages and disadvantages: M1 is simple and computationally not too much expensive but provides a limited amount of information, whilst M3 is computationally demanding but provides all the information related to the behaviour of the joint.

3 APPLICATIONS

As an application of the proposed procedure, the M1 model is reported for two important human joints, namely the knee and the ankle; a few details are given regarding the extension of these models to M2 and M3 models.

3.1 THE M1 MODEL OF THE HUMAN KNEE JOINT

The knee is a joint which allows the relative motion between three bones of the legs, i.e. the femur, tibia and patella (Figure 1). Two sub-joints can be recognized according to the bones that enter into contact with each other during knee flexion: the tibio-femoral joint (TF) allows the relative motion between the femur and tibia and the patello-femoral joint (PF) allows the relative motion between the patella and femur. These motions are guided in general by articular surfaces (the femur and tibia condyles, the trochlea and the back surface of the patella), by passive structures (such as the ligaments) and by active structures (such as the muscles).

The passive motion of the knee is thus the relative motion of the tibia, femur and patella when no loads are applied to the articulation. Several studies [9, 22] prove that the movement of the TF during passive flexion is a one DOF motion: once the flexion angle is imposed on the articulation, the corresponding pose (position and orientation) of the tibia with respect to the femur is defined, both univocally and experimentally replicable. The same result holds also for the relative movement of the patella and femur [2]: although the PF is slightly more slack during passive flexion if compared to the TF, experimental results prove that for a given flexion angle of the knee the relative pose of the patella with respect to the femur is replicable. As a consequence, the patella also has a one DOF of unresisted motion with respect to the femur.

Among the equivalent spatial parallel mechanisms proposed to simulate the passive motion of the knee, one DOF mechanisms have been presented which can accurately replicate the passive motion of the TF [16, 18, 22] and PF [19]. The first equivalent mechanism for the modelling of the whole knee has been presented in [19]. The philosophy of equivalent mechanisms fits well with the rules of the new approach proposed in this study: these models can indeed replicate the knee passive motion by modelling only those structures that actually influence this particular motion. On the contrary, the other structures are excluded from the passive motion model: they will be modelled in step 2 or step 3 of the procedure.

The passive motion model of the knee required by the first step can be devised by referring to the above-cited studies. In this paper, in particular, TF motion is modelled by means of a 5-5 fully parallel mechanism (defined in the following) as in [16], while PF motion is modelled by means of a revolute joint, suitably connected to the femur and tibia, as presented in [19]. The complete knee model is represented in Figure 2 and its key aspects are reported below.

In order to define a model which can replicate the passive motion of the knee, it is fundamental to identify the relative poses of the tibia, femur and patella and to understand how articular surfaces, and passive and active structures influence both TF and PF motion. The bones' relative poses can be identified in space by three anatomical frames, respectively attached to the tibia (S_t), femur (S_f) and patella (S_p), as in Figure 2; more detailed information on the coordinate reference systems are reported in [19]. As regards articular surfaces, the femur and tibia condyles can be fitted by spheres centred on points $\mathbf{A}_1$ and $\mathbf{A}_2$ on the tibia and on points $\mathbf{B}_1$ and $\mathbf{B}_2$ on the femur (Figure 2). These

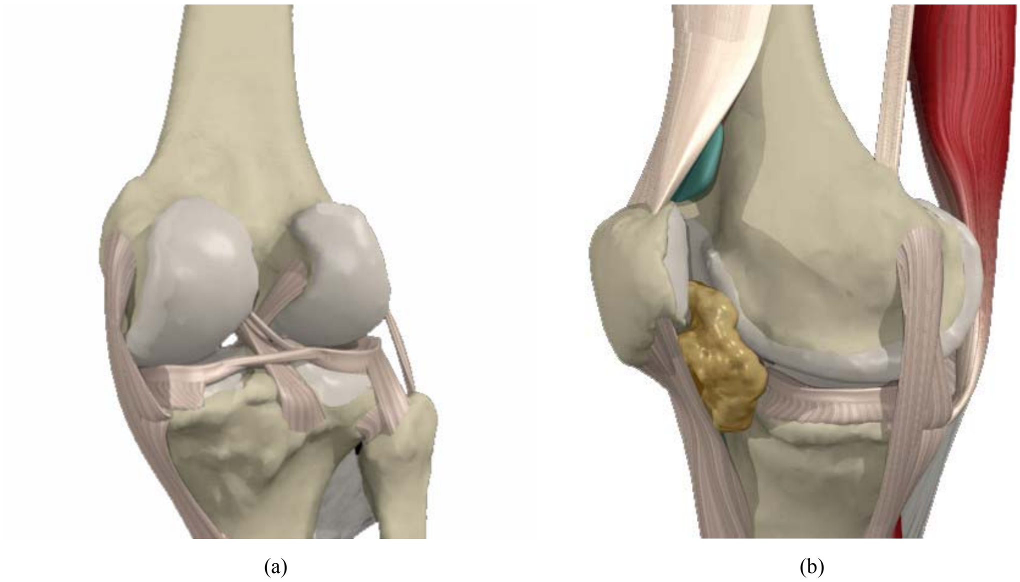

Figure 1 The knee joint: (a) posterior view and (b) medial view.

spheres have to remain in contact two by two during passive flexion and could thus be replaced by two kinematically equivalent rigid binary links (not shown in Figure 2) connected at the femur and tibia through spherical pairs centred at points $\mathbf{A}_i$ and $\mathbf{B}_i$, i = 1, 2. Furthermore, the trochlea and the portions of femoral condyles which are involved in PF contact can be approximated by a cylinder. Thus, the relative motion of the patella and femur occurs about an axis, i.e. the axis of the approximating cylinder, while axial translation can be ignored. As a consequence, the contact between the patella and femur can be modelled by a revolute joint which mutually connects the two bones. This joint can be identified on the femur by the unit vector $\mathbf{n}_1$ (parallel to the joint axis) and the point $\mathbf{Q}_1$ (arbitrarily chosen on the joint axis); the joint can be identified on the patella accordingly, by means of the unit vector $\mathbf{n}_2$ and the point $\mathbf{Q}_2$. The axis on the femur and the one on the patella are constrained to be coincident during passive motion, while the distance λ between $\mathbf{Q}_1$ and $\mathbf{Q}_2$ has to remain constant. All these surface parameters are shown in Figure 2; in particular it is worth noting that in the figure both unit vectors $\mathbf{n}_1$ and $\mathbf{n}_2$ define the same axis, on account of the said geometrical constraints, that is also the axis where points $\mathbf{Q}_1$ and $\mathbf{Q}_2$ lie.

Moreover, since no forces are exerted on the knee, no forces can be exerted by the passive structures to satisfy the equilibrium of the system composed of the tibia, femur and patella. The internal forces due to the passive structures could be internally autobalanced, thus invalidating the concept of unloaded condition, but these circumstances would be extremely complex to achieve on the full flexion-extension movement, also considering friction between articular components. As a consequence, the ligaments cannot be tight during passive flexion: they can at the most reach the limit between laxity and tension. These

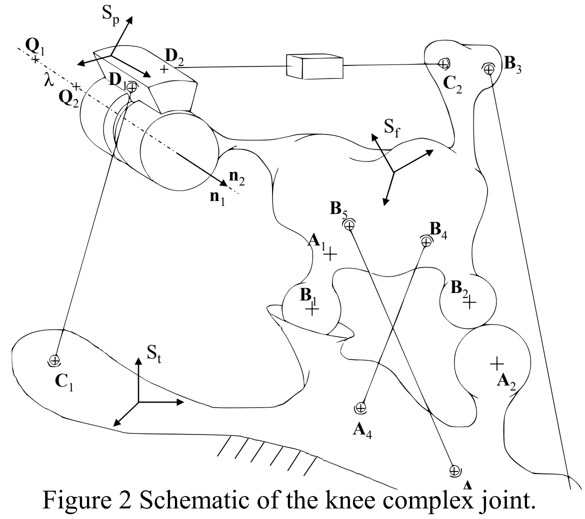

Figure 2 Schematic of the knee complex joint.

considerations are supported by experimental observations which show that some fibres of the anterior cruciate (ACL), posterior cruciate (PCL), medial collateral (MCL) and patellar (PL) ligaments remain almost isometric in passive flexion, while other structures are slack. Because of this property, these fibres can be seen as four rigid binary links: the first three links are connected at the femur and tibia through spherical pairs centred respectively at the points $\mathbf{A}_i$ and $\mathbf{B}_i$, i = 3, 4, 5; the last one is connected at the points $\mathbf{C}_1$ on the tibia and $\mathbf{D}_1$ on the patella through spherical pairs (Figure 2).

As regards active structures, they can intrinsically exert forces but, in general, they practically do not oppose external forces when inactive. Since no loads are applied to the joint during passive motion, active structures remain inactive: they cannot guide the passive motion of the knee. As a consequence, the muscles are not considered in the

M1 model, in general; only the quadriceps is represented for completeness. It is modelled by means of two rigid links joined together by a prismatic pair; this two-link complex is then connected at the point $\mathbf{C}_2$ on the femur and $\mathbf{D}_2$ on the patella through spherical pairs (Figure 2). It can be easily proved that the addition of the two-link complex to the model does not modify PF and TF motion.

The equivalent mechanism represented in Figure 2 is the passive motion model of the whole knee. It can be proved that this mechanism has one DOF, if idle inessential DOFs are ignored. In particular, the TF sub-chain (i.e. the mechanism composed by the femur and tibia and by the links connected at the points $\mathbf{A}_i$ and $\mathbf{B}_i$, $i = 1, 2,..., 5$) is a 5-5 fully parallel mechanism.

The relative motion between the tibia, femur and patella can be found by solving the closure equations of the equivalent mechanism. In particular, the solution of these equations provides the relative poses of the three anatomical frames S_t, S_f and S_p, once the flexion angle is imposed on the joint. A relative pose of the femur with respect to the tibia can be expressed by means of the 3x3 rotation matrix R_{tf} for the transformation of vector components from S_f to S_t, and the position $\mathbf{P}_{tf}$ of the origin of S_f in S_t. Matrix R_{tf} can be expressed as a function of three rotation parameters α_{tf}, β_{tf} and γ_{tf}, which represent the flexion, ab/adduction and intra/extra rotation angles of the femur relatively to the tibia, according to a convention deduced by [10]. Likewise, the matrix R_{fp} (function of the angles α_{fp}, β_{fp} and γ_{fp}) and the vector $\mathbf{P}_{fp}$ express a relative pose of the patella with respect to the tibia. Even though the convention in [10] was originally defined for the TF, its application on other joints (the PF included) is becoming routine practice in the scientific literature.

The closure equations of the complete mechanism are:

$$
\begin{aligned}
&\left\| \mathbf{A}_i - R_{tf} \cdot \mathbf{B}_i - \mathbf{P}_{tf} \right\| = L_i \quad (i = 1, 2, \ldots, 5) \\
&R_{fp} \cdot \mathbf{n} \quad = \mathbf{n} \\
&R_{fp} \cdot \mathbf{Q} \quad + \mathbf{P}_{fp} = \lambda \mathbf{n} \quad + \mathbf{Q} \\
&\left\| R_{tf} \cdot \left(R_{fp} \cdot \mathbf{D} \quad + \mathbf{P}_{fp} \right) + \mathbf{P}_{tf} - \mathbf{C} \quad \right\| = L
\end{aligned}
\tag{1}
$$

where the points $\mathbf{A}_i$ and $\mathbf{C}_1$ are measured in S_t, the points $\mathbf{B}_i$, $\mathbf{C}_2$, $\mathbf{Q}_1$ and the vector $\mathbf{n}_1$ are measured in S_f, the points $\mathbf{Q}_2$, $\mathbf{D}_1$, $\mathbf{D}_2$ and the vector $\mathbf{n}_2$ are measured in S_p; L_i are the lengths of the rigid links connected at the points $\mathbf{A}_i$ and $\mathbf{B}_i$; L is the length of the link connected at the points $\mathbf{C}_1$ and $\mathbf{D}_1$; the symbol $\|\cdot\|$ is the L^2-norm of the vector. The first 5 scalar equations and the last one constrain the points $\mathbf{A}_i$, $\mathbf{B}_i$ and $\mathbf{C}_1$, $\mathbf{D}_1$ to keep a constant distance; the second and the third vectorial equations force the axis identified by $\mathbf{n}_1$ and $\mathbf{Q}_1$ to be coincident with that identified by $\mathbf{n}_2$ and $\mathbf{Q}_2$; moreover, the third vectorial equation constrains $\mathbf{Q}_1$ and $\mathbf{Q}_2$ to keep a constant distance.

In the second vectorial expression of (1) only two out of three equations are independent, since $\mathbf{n}_1$ and $\mathbf{n}_2$ both have unitary norms. Thus, if the flexion angle α_{tf} is assigned, (1) is a system of 11 equations in the 11 unknowns β_{tf}, γ_{tf}, α_{fp}, β_{fp}, γ_{fp} and $\mathbf{P}_{tf}$, $\mathbf{P}_{fp}$ components. These parameters define the relative pose of the tibia, femur and patella at each imposed flexion angle. System (1) is a nonlinear system which can be solved, for instance, by a quasi-Newton numerical procedure.

As a result of step 1 of the proposed procedure, the model parameters which define the structures which guide the passive motion of the knee are determined. These parameters are the components of the insertion points $\mathbf{A}_i$, $\mathbf{B}_i$, $\mathbf{C}_1$, $\mathbf{D}_1$, those of the points $\mathbf{Q}_1$, $\mathbf{Q}_2$ (only four out of six components are independent, because of the arbitrariness of the points), the components of the vectors $\mathbf{n}_1$ and $\mathbf{n}_2$ (only four out of six components are independent, since these vectors have unitary norm), the link lengths L_i, L and the distance λ between $\mathbf{Q}_1$ and $\mathbf{Q}_2$. These parameters constitute a set of 51 geometrical parameters which define the M1 model of the knee and which have to be identified based on experimental data. This set will remain unchanged during steps 2 and 3 of the procedure, in order to observe the first rule of the sequential approach.

The experimental data provide both the geometric dimensions of the main anatomical structures, which are used as a first tentative geometry of the mechanism, and the relative pose of the tibia, femur and patella at a number n of selected values of the flexion angle within a complete excursion.

The identification procedure used to synthesize the optimum geometry of the mechanism is based on optimization. At each step of the optimization iterative process, the closure equations (1) are solved for each measured flexion angle; then the relative poses of the tibia, femur and patella are iteratively compared with the poses obtained by measurement data by means of an error function f (objective function). The function is the sum of the squared and weighted errors of the experimental values of the variables with respect to the calculated ones, for all the n values of the flexion angle (α_{tf}). The function f is defined as follows:

$$
f = \sum_{j=1}^{11} \sum_{i=1}^{n} \frac{(x_{ji} - x_{ji}^{*})^2}{(x_{j_{\max}} - x_{j_{\min}})^2} \tag{2}
$$

where, x_{ji} is the actual value of the j-th dependent variable, $j = 1, 2, \ldots, 11$, at the i-th pose, $i = 1, 2, \ldots, n$; x_{ji}^{*} is the corresponding experimental value of the variable x_{ji}; $x_{j\max}$ and $x_{j\min}$ are the maximum and minimum values of each of the dependent variables obtained during the experimental session.

If equation system (1) does not provide a real solution then an arbitrarily high value is given to the objective function f. If the objective function reaches a minimum the process stops, otherwise a new geometry of the mechanism is defined and the Eq. (2) is evaluated once again.

This particular objective function is proposed since it proved to be effective [7, 18]. Since the function f is highly nonlinear and has discontinuities, the optimization procedure is initially solved by means of a genetic algorithm or, alternatively, by means of a direct search method. The obtained solution is then refined by means of a

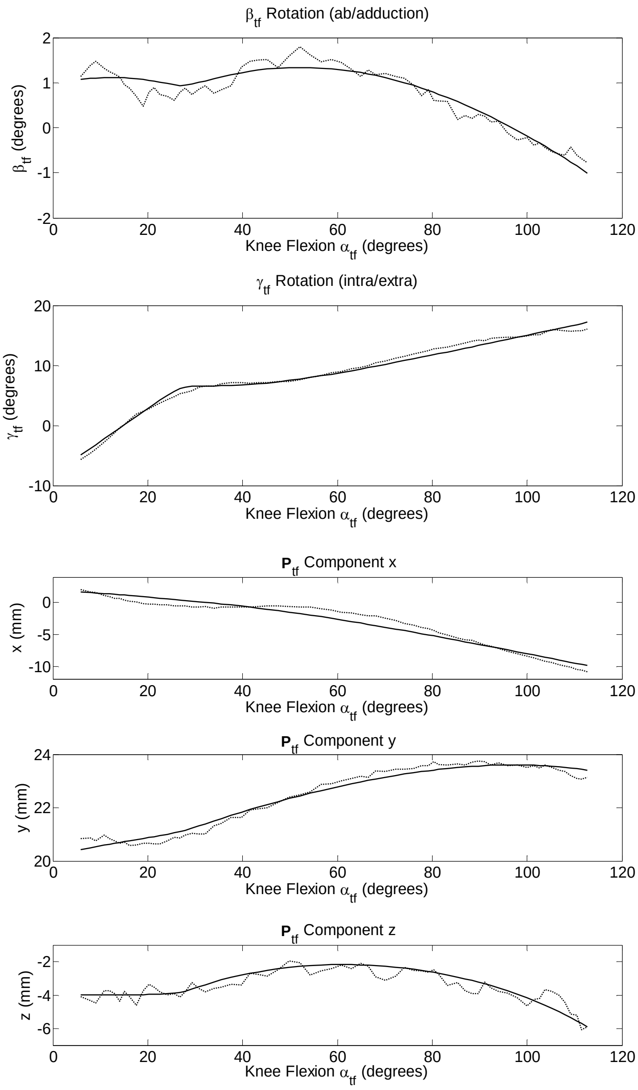

Figure 3 Passive motion simulation: angles β_{tf}, γ_{tf} and $\mathbf{P}_{tf}$ components versus knee flexion angle.

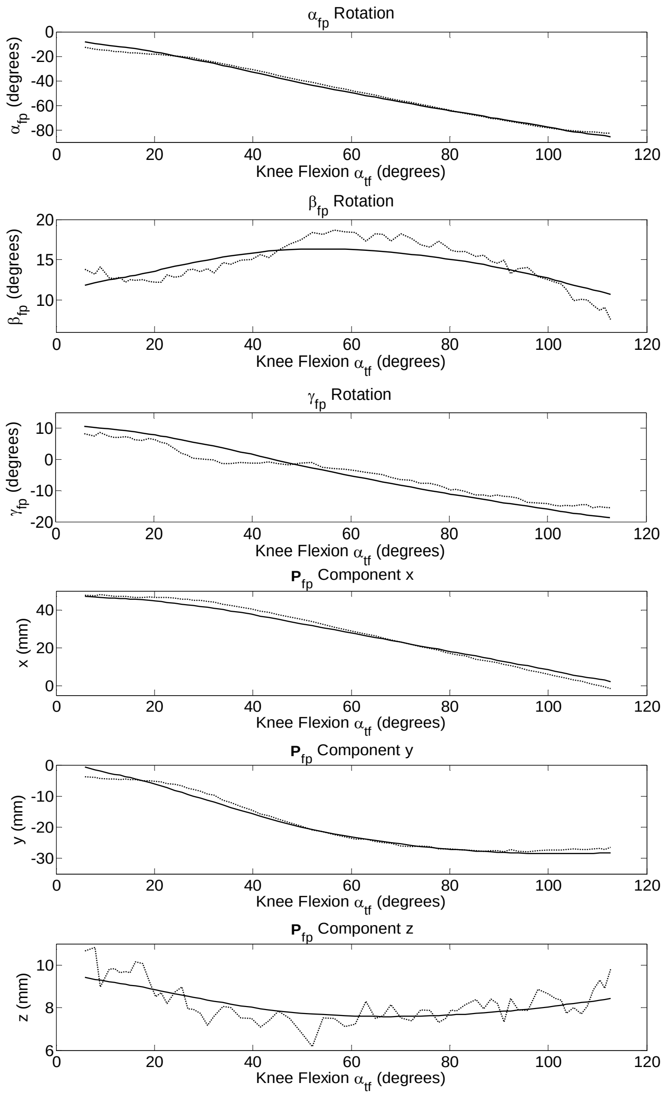

Figure 4 Passive motion simulation: angles α_{fp}, β_{fp}, γ_{fp} and $\mathbf{P}_{fp}$ components versus knee flexion angle.

quasi-Newton algorithm. It is worth noting that the introduction of lower and upper bounds to the values of the 51 parameters that define the geometry of the equivalent mechanism provides a final geometry of the optimized equivalent mechanism which retains the anatomical feature of the knee joint.

Figures 3-4 report both experimental (dotted lines) and simulation (solid lines) data of a specimen. In particular, the angles β_{tf}, γ_{tf}, and the $\mathbf{P}_{tf}$ components are reported in Figure 3, as a function of the knee flexion angle; the angles α_{fp}, β_{fp}, γ_{fp} and the $\mathbf{P}_{fp}$ components are reported accordingly in Figure 4.

These results show that the proposed kinematic model of the knee joint can accurately reproduce the relative motion of the patella, femur and tibia in passive flexion.

3.2 THE M1 MODEL OF THE HUMAN ANKLE JOINT

The human ankle joint features three main bones: the tibia which forms the inside, or medial, portion of the ankle; the fibula which forms the lateral, or outside portion of the ankle; and the talus underneath (Figure 5). A fourth bone, the calcaneus, is considered as rigidly joined with the talus. Clinical evidence and experimental results show that the passive relative motion of the tibia and talus, which are the main bones of the ankle joint, is a complex spatial motion that can be replicated very well by one DOF spatial equivalent mechanisms [6, 7, 14]. Like the knee joint, these mechanisms are based on the geometry of the main anatomical structures of the ankle joint, namely on the shape of the talus and tibio/fibula bones at their interface and on two main ligaments. Moreover, these mechanisms rely upon the experimental observations that some fibres of the calcaneofibular ligament (CaFiL) and the tibiocalcaneal ligament (TiCaL) are nearly isometric during ankle passive motion. The location of this ligaments is shown in Figure 5. In particular, in [7] the relative motion of the talus/calcaneus, considered as a single bone, with respect to

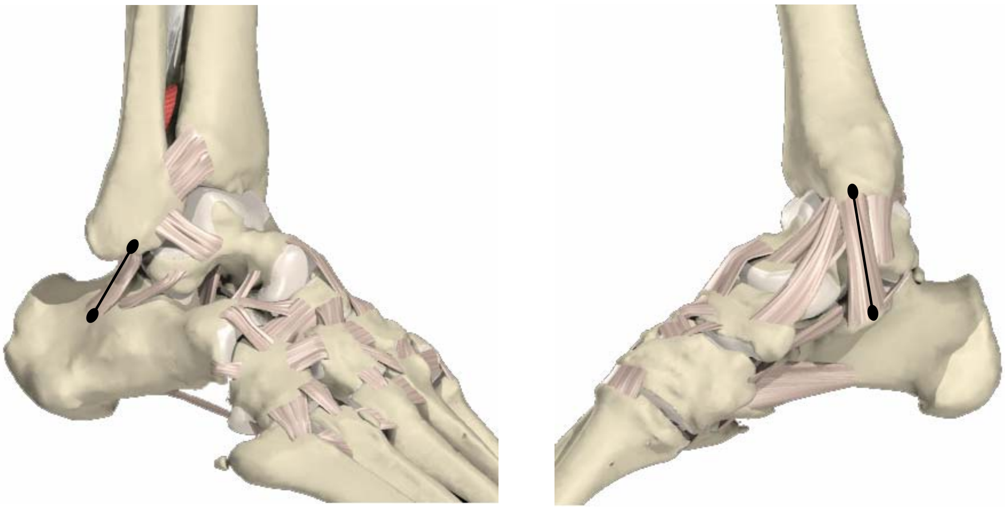

(a) (b)

Figure 5 The ligaments of a right human ankle joint: (a) calcaneofibular (CaFiL) and (b) tibiocalcaneal (TiCaL).

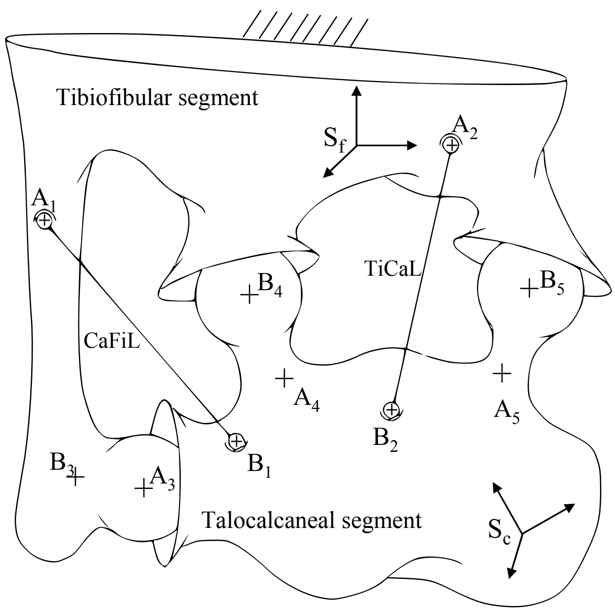

Figure 6 Schematic of the ankle complex joint.

the tibia/fibula, also considered as a single bone, was modelled by means of three sphere-to-sphere contact points at the tibiotalar interface and by the isometric fibres of the CaFiL and TiCaL ligaments.

The three contact points were identified at the lateral malleolus (a pyramidal process on the lateral surface of the lower extremity of fibula), at the internal region of the inferior surface of the distal tibia articulated with the talus surface, and at the medial malleolus (a pyramidal process on the medial surface of the lower extremity of tibia).

Based on these observations and assumptions a schematic of the M1 model of the ankle joint is shown in Figure 6. Here the two talocalcaneal and tibiofibular segments feature three sphere-to-sphere contact points where points $\mathbf{A}_i$ and $\mathbf{B}_i$, i = 3, 4, 5, represent the centres of the mating spherical surfaces fixed to the tibia/fibula and talus/calcaneus respectively, while points $\mathbf{A}_i$, and $\mathbf{B}_i$, i = 1, 2, represent the insertion points on the two segments of two isometric fibres of the two ligaments CaFiL and TiCaL respectively.

During the relative motion of the two ankle segments, each pair of mating spherical surfaces maintains the contact; therefore the distance L_i=A_iB_i , i = 3, 4, 5, is constant. Moreover the distance L_i=A_iB_i, i = 1, 2 is also constant during the passive motion since it represents the length of the ligament isometric fibre.

According to these assumptions, the equivalent mechanism is defined by two rigid bodies, i.e. the tibiofibular and talocalcaneal segments, interconnected by five rigid binary links $\mathbf{A}_i$ and $\mathbf{B}_i$, i = 1, 2, …, 5, where $\mathbf{A}_i$ and $\mathbf{B}_i$, i = 1, 2 replace the isometric fibres while $\mathbf{A}_i$ and $\mathbf{B}_i$, i = 3, 4, 5, represent the centres of the talus/calcaneus and tibia/fibula spherical surfaces respectively. This equivalent mechanism can be more synthetically represented by a spatial fully-parallel mechanism (FPM) of type 5-5 which provides the movable platform with one DOF with respect to the fixed base (rotation of links about the axes through their ending points $\mathbf{A}_i$ and $\mathbf{B}_i$, is irrelevant to the relative mobility of the two main segments).

The closure equations of the 5-5 FPM can be found based on the consideration that each pair of points ($\mathbf{A}_i$, $\mathbf{B}_i$), i = 1, 2, ... , 5, is constrained to maintain a constant mutual distance L_i, during motion. With these considerations, the closure equations of the M1 model of the ankle joint with one DOF can be expressed by:

$$\left\| \mathbf{A}_i - R \cdot \mathbf{B}_i - \mathbf{P} \right\| = L_i \quad (i = 1, 2, \ldots, 5) \tag{3}$$

where the points $\mathbf{A}_i$ and $\mathbf{B}_i$ are measured in the Cartesian reference systems S_f and S_c respectively, which are embedded in the tibiofibular segment and the talocalcaneal segment respectively. More detailed information on the coordinate reference systems is reported in [7]. The symbol $\|\cdot\|$ is the L^2-norm of the vector, and $\mathbf{P}$ the position of the origin O_c of S_c in the reference system S_f. The rotation matrix R, that transforms the components of a vector from system S_c to system S_f , can be expressed as a function of three parameters α, β and γ (intra/extra rotation, pronation/supination and dorsi/plantar flexion of the foot with respect to the tibia) that represent the rotation angles of the human ankle, as deduced by the Grood and Suntay convention [8, 10].

For a given geometry of the 5-5 FPM, the system (3) can be regarded as a system of five nonlinear equations in six variables, i.e. the three components of vector $\mathbf{P}$ and the three orientation parameters which define the rotation matrix R. If, for instance, the angle γ (the ankle flexion) is given, the remaining five variables can be found by solving system (3).

Like the knee joint, the non-linear system (3) is solved by means of a quasi-Newton numerical procedure. Moreover, the geometrical parameters of the ankle model are identified based on experimental data by means of an identification procedure similar to the one presented in the previous paragraph. In this case the parameter j, which appears in Eq. (2), is j = 1, 2, …, 5 instead of j = 1, 2, …, 11.

Like the knee, the optimization problem is solved by means of a genetic algorithm followed by a quasi-Newton algorithm. It is worth noting that the introduction of lower and upper bounds to the values of the 35 parameters (points $\mathbf{A}_i$ and $\mathbf{B}_i$, i = 1, 2, …, 5 and lengths L_i, i = 1, 2, …, 5), that define the geometry of the equivalent mechanism, provides a final geometry of the optimized equivalent mechanism which retains the anatomical feature of the ankle joint.

For different legs, the poses of the talus with respect to the tibia obtained by means of the experimental sessions were compared with those obtained by means of the 5-5 equivalent FPM.

Figure 7 reports both experimental and simulation data of a specimen. In particular, the angles α, β and the positions x, y, and z of the origin of the reference system S_c with respect to S_f are reported in Figure 7 respectively, as functions of the ankle flexion angle.

The experimental results are identified by the symbol “Δ” and interpolated by a dash-dot line. The interpolation makes it possible to use a higher number of experimental data, which may be useful for the optimal synthesis of the geometry of the model M1.

Inspection of the figures reveals that the new equivalent spatial mechanism replicate the passive motion of the human ankle very well.

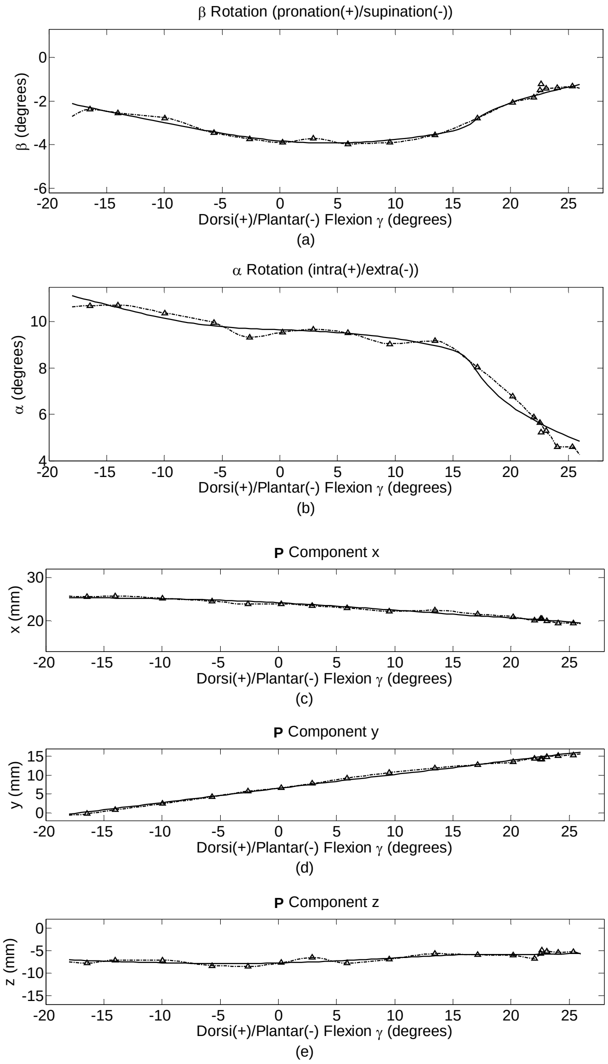

Figure 7 Passive motion simulation: angles β, α and $\mathbf{P}$ components versus ankle flexion angle γ.

3.3 THE M2 AND M3 MODELS

The M1 models of the knee and the ankle joints described in previous paragraphs can be generalized by means of the proposed sequential approach, in order to obtain the M2 and M3 models, as described in section 2.

Details regarding the model M2 for the knee are reported in [20] while the M2 model for the ankle was partially developed in [5], when this new procedure was still not completely devised. Just a few key points are given here on the M2 model. As outlined in section 2, the M2 models of the knee and the ankle make it possible to replicate the motion of the joints when external forces and moments are applied to the bones; in particular, if static forces are considered, the elastic properties of the joint passive structures can be identified. The previously excluded passive structures are added to the optimized M1 models, which remain unchanged and embedded in the new models to satisfy the first rule of the sequential approach. As the only difference, the links of the two equivalent mechanisms of the knee and ankle joint in the M2 models are not considered rigid, but they can be deformed by loads. The structures added in the M2 models must not interfere with passive motion, to satisfy the second rule of the sequential approach: for instance, the lengths of the popliteus tendon, the lateral collateral, the arcuate and the oblique popliteus ligaments (i.e. the passive structures added in the M2 model of the knee) are chosen in a way that these structures are never tight during passive motion. The new geometric and structural parameters are identified by an optimization procedure, similar to that presented in this study.

At the moment, the M3 models for the knee and ankle joints are under developments. Active structures are added to the previously optimized M2 models; the new geometrical and structural parameters are then identified by means of an optimization procedure similar to the previous ones. The final result is a model which would simulate the behaviour of the joint even under dynamic loads applied by muscles.

4 CONCLUSIONS

This paper presents a sequential procedure for the modelling of diarthrodial joints.

The procedure relies upon some basic assumptions (rules) and provides, in three sequential steps, three different joint models (M1, M2 and M3 respectively) with increasing complexity that incorporate both more and more complex anatomical structures and different joint loading conditions.

In particular, the M1 model provides a model of the passive motion of the joint and incorporates only some basic anatomical structures of the joint. The M2 model comprises the M1 model with the addition of further passive structures and external forces. Elastic behaviour of the passive structures is taken into account in the model. The M3 model comprises the M2 model and the active anatomical structures such as the muscles. The M3 model is the most complete model and can provide kinematic, static and dynamic information on joint behaviour.

However, all the models have an important role: step by step they make it possible to highlight the role that each individual joint structure plays in the joint.

Finally, the results of the M1 model for both the knee and the ankle are reported, showing the efficiency of the proposed procedure.

ACKNOWLEDGMENTS

The authors would like to thank Dr Leardini of Istituti Ortopedici Rizzoli for the efficient collaboration in providing the measurement data of in the vivo experiments.

REFERENCES

[1] Andriacchi T.P., Mikosz R.P., Hampton S.J. and Galante J.O., Model studies of the stiffness characteristics of the human knee joint. *Journal of Biomechanics*, Vol. 16, No. 1, pp. 23-29, 1983.

[2] Belvedere C., Catani F., Ensini A., Moctezuma de la Barrera J.L. and Leardini A., Patellar tracking during total knee arthroplasty: an in vitro feasibility study. *Knee Surgery, Sports Traumatology, Arthroscopy*, Vol. 15, pp. 985-993, 2007.

[3] Blankevoort L., Huiskes R. and De Lange A., Envelope of passive knee joint motion. *Journal of Biomechanics*, Vol. 21, No. 9, pp. 705-720, 1988.

[4] Essinger J.R., Leyvraz P.F., Heegard J.H. and Robertson D.D., A mathematical model for the evaluation of the behaviour during flexion of condilar-type knee prosthesis. *Journal of Biomechanics*, Vol. 22, No. 11, pp. 1229-1241, 1989.

[5] Corazza F., O'Connor J.J., Leardini A. and Parenti-Castelli V., Ligament fibre recruitment and forces for the anterior drawer test at the human ankle joint. *Journal of Biomechanics*, Vol. 36, pp. 363-372, 2003.

[6] Di Gregorio R., Parenti-Castelli V., O'Connor J.J. and Leardini A., Mathematical models of passive motion at the human ankle joint by equivalent spatial parallel mechanisms. *Medical & Biology Engineering & Computing*, Vol. 45, No. 3, pp. 305-313, 2007.

[7] Franci R. and Parenti-Castelli V., A 5-5 one degree of freedom fully-parallel mechanism for the modelling of passive motion at the human ankle joint. *Proc. of ASME-IDETC/CIE 2007*, Las Vegas (USA), pp. 1-8, 2007.

[8] Franci R. and Parenti-Castelli V., A one-degree-of-freedom spherical wrist for the modelling of passive motion of the human ankle joint. *Proc. of IAK 2008*, Lima (Peru), pp.1-13, 2008.

[9] Goodfellow J.W. and O'Connor J.J., The mechanics of the knee and prosthesis design. *Journal of Bone Joint Surgery [Br]*, Vol. 60-B, pp. 358-369, 1978.

[10] Grood E.S. and Suntay W.J., A joint coordinate system for the clinical description of three-dimensional motions: application to the knee. *Journal of Biomechanical Engineering*, Vol. 105, No. 2, pp. 136-144, 1983.

[11] Hefzy M.S. and Cooke T.D.V., Review of knee models: 1996 update. *Applied Mechanics Review*, Vol. 49, No. 10, part 2, pp. 187-193, 1996.

[12] La Fortune M.A., Cavanagh P.R., Sommer III H.J. and Kalenak A., Three-dimensional kinematics of the human knee during walking. *Journal of Biomechanics*, Vol. 25, No. 4, pp. 347-357, 1992.

[13] Leardini A., O'Connor J.J., Catani F. and Giannini S., Kinematics of the human ankle complex in passive flexion: a single degree of freedom system. *Journal of Biomechanics*, Vol. 32, No. 2, pp. 111-118, 1999.

[14] Leardini A., O'Connor J.J., Catani F. and Giannini S., A geometric model of the human ankle joint. *Journal of Biomechanics*, Vol. 32, No. 6, pp. 585-591, 1999.

[15] O'Connor J.J., Shercliff T.L., Biden E. and Goodfellow J.W., The geometry of the knee in the sagittal plane. *Journal of Engineering in Medicine*, Vol. 203, pp. 223-233, 1989.

[16] Parenti-Castelli V., Leardini A., Di Gregorio R. and O'Connor J.J., On the modeling of passive motion of the human knee joint by means of equivalent planar and spatial parallel mechanisms. *Autonomous Robots*, Vol. 125, No. 2, pp. 219-232, 2003.

[17] Rahman E.A. and Hefzy M.S., A two-dimensional dynamic anatomical model of the human knee joint. *Journal of Biomechanical Engineering*, Vol. 115, pp. 357-365, 1993.

[18] Sancisi N. and Parenti-Castelli V., A 1-dof parallel spherical wrist for the modelling of the knee passive motion. *Proc. of the 12th IFToMM World Congress*, Besançon (France), pp. 1-6, 2007.

[19] Sancisi N. and Parenti-Castelli V., A new 3d kinematic model of the patellofemoral joint during knee passive motion. *Proc. of AIMeTA 2007*, Brescia (Italy), pp. 1-12, 2007.

[20] Sancisi N. and Parenti-Castelli V., A Sequential Approach for Modelling the Knee Joint Stiffness. *Proc. of Romansy 2008*, Tokyo (Japan), pp.1-9, 2008.

[21] Tumer T.S. and Engin A.E., Three-body segment dynamic model of the human knee. *Journal of Biomechanical Engineering*, Vol. 115, pp. 350-356, 1993.

[22] Wilson D. and O'Connor J.J., A three-dimensional geometric model of the knee for the study of joint forces in gait. *Gait and Posture*, Vol. 5, pp. 108–115, 1997.

[23] Wismans J., Velpaus F., Janssen J., Huson A. and Struben P., A three-dimensional mathematical model of the knee-joint. *Journal of Biomechanics*, Vol. 13, pp. 677-685, 1980.

ISSN 1590-8844
International Journal of Mechanics and Control, Vol. 10, No. 01, 2009

WORKSPACE ENLARGEMENT MERGING ASSEMBLY MODES. APPLICATION TO THE 3-$\underline{R}$RR PLANAR PLATFORM

Erik Macho Oscar Altuzarra Victor Petuya Alfonso Hernandez

Department of Mechanical Engineering, Faculty of Engineering in Bilbao, Spain

ABSTRACT

The direct kinematic problem in parallel manipulators has multiple solutions that are traditionally called assembly modes. Non-singular transitions between some of these solutions have been detected and shown in the past. Cusp points have been defined as special points on the projection of the singularity curves onto the joint space that have the property of allowing such non-singular transitions when encircling them. In this paper the authors will show that the condition for such a transition is more general. Authors also argue about the need for a differentiation between the concepts of assembly mode and solution of the direct kinematic problem. This paper also provides an example where modifying some dimensions, several assembly modes merge achieving a larger practical workspace.

Keywords: Planar parallel robot, Singularities, Assembly modes, Configuration space, Cusp points

1 INTRODUCTION

Parallel manipulators often present limited and complex workspaces with internal singularities. Thus, the workspace size and shape, and the singularity loci are considered the main design criteria of these robots. In general they have multiple solutions of the direct kinematic problem (DKP), traditionally called assembly modes, and the inverse kinematic problem (IKP), also called working modes. Singularities are obtained by the analysis of the conditions that make the Jacobian matrices singular.

IKP singularities, where the determinant $|J_{IKP}|=0$, are the workspace boundaries. At these postures, a dependence among the output velocities of the platform is verified, so they may be considered inappropriate at an operational level due to manipulability restrictions. However, they do not imply a loss of control of the robot. On the contrary DKP singularities arise when $|J_{DKP}|=0$. In such configurations, a dependence among the input velocities of the manipulator appears. This means that the robot becomes uncontrollable, so these postures must be avoided.

Contact author: A. Hernandez

Alameda de Urquijo s/n, 48013, Bilbao, Spain.

Due to the typical architecture of parallel manipulators, if each kinematic chain connecting the moving platform to the fixed frame contains a single actuator (one input variable), the IKP Jacobian matrix is diagonal. Each term of such diagonal is associated to one kinematic chain and the determinant vanishes if any term does. This means that each kinematic chain is able to produce IKP singularities independently. IKP singularities are reached whenever a chain changes its IKP configuration. Therefore an IKP singularity is achieved when two IKP solutions coalesce at the same posture. Different working modes are separated by IKP singularities.

Each working mode has its own DKP singularity loci, which divides the workspace into a set of singularity-free regions associated with positions with different sign of $|J_{DKP}|=0$. A common practice in the use of these manipulators is to keep them at all times in the same singularity-free region, so the practical workspace remains limited. However, [6] explained how several singularity-free regions associated to different working modes can be joined to achieve a larger practical workspace. IKP singularities are considered as gates which allow the transition among singularity-free regions associated to different working modes without risk of uncontrollability.

Some applications are trying to show the practicability of changing between different DKP solutions, whereby the workspaces associated with each solution are joined, to form a larger practical workspace. Nevertheless, in this kind of approaches DKP singularities are crossed making use of additional strategies, such as the use of redundant

actuators in passive joints, which are specifically controlled at the singularity, or making use of physical effects like gravity [4], which may imply a certain risk of uncontrollability.
Initially, [2] proposed the hypothesis that different DKP solutions are always separated by DKP singularities. Therefore, any path joining two DKP solutions should cross one of these singular postures where the robot becomes uncontrollable. However, [3] showed that this assumption is not always verified. They found an example of manipulator, a 3-RPR planar platform, which was able to perform a non-singular transition between two DKP solutions. It was tested numerically that any point of a path joining both solutions had $|J_{DKP}| \neq 0$.
Later works have gone deeper into this topic. [8] showed how when a DKP singularity is reached several DKP solutions coalesce at the same posture. This means that at a singular configuration the solution has a multiplicity equal to two or higher. The most common are the solutions with multiplicity two which were called ordinary singularities. However, it was proved that there are some special singularities where three DKP solutions coalesce simultaneously. Their existence makes possible non-singular transitions among some DKP solutions. In the joint space (input variables domain) those special positions appear as cusp points in the singularity loci. It was explained why a non-singular DKP solution changing path in the joint space always encircles one of these cusp points. Due to this phenomenon, manipulators presenting this ability have been called cuspidal robots. There are other authors that have also analyzed this phenomenon [10] [5].
The configuration space is a concept used by several researchers [8] [11]. It allows the direct visualizing and analysis of all assembly modes and working modes simultaneously. Making use of this entity this paper presents a procedure to get the total number of assembly modes of a mechanism. Likewise, it will be shown the possibility of merging several assembly modes in one in order to obtain a larger practical workspace, namely a larger region of the workspace free of internal DKP singularities. Taking into account some of the contents presented here the authors propose the convenience of a differentiation between the concept of DKP solution and assembly mode, which traditionally have been considered the same thing.
Although the discussion presented here could be considered of general application, a typical example of parallel manipulator will be used to illustrate concepts. The 3-RRR planar platform has been chosen because it is a well known mechanism whose kinematic characteristics have been studied in many works [9] [1]. For this example it will be shown how encircling a cusp point is not the only way of making a non-singular transition between DKP solutions. Another example of non-singular, non-cuspidal transition was developed in [7].

2 THE 3-RRR PLANAR PARALLEL MANIPULATOR

The 3-RRR planar platform is a three degrees of freedom mechanism, shown in Fig. 1. Actuators are located in the fixed revolute joints A_i, so the input variables are angles θ_i. The output variables are those defining the position of the moving platform $C_1C_2C_3$, namely the coordinates x and y of C_1 and the angle φ. Revolute joints B_i and C_i are passive kinematic joints. The example proposed has the three actuated joints coincident in the same point because this particularization gives to the manipulator some special characteristics that will be explained in the next section.

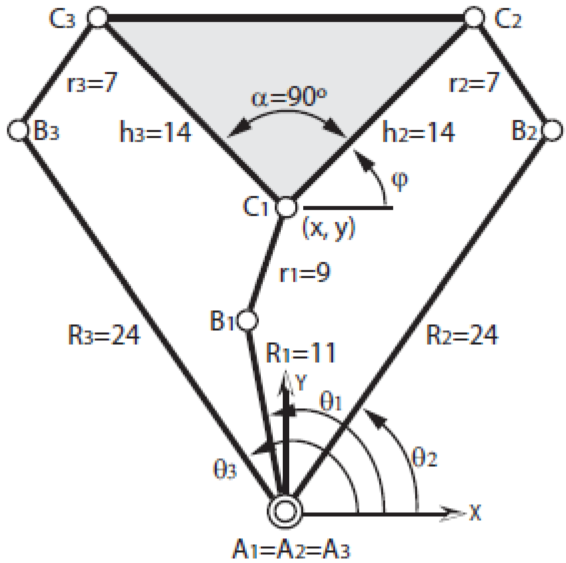

Figure 1 3-RRR manipulator with coincident fixed revolute joints.

The constraint equations for this example are:

$$(x - R_1\cos(\theta_1))^2 + (y - R_1\sin(\theta_1))^2 = r_1^2 \quad (1)$$

$$(x + h_2\cos(\varphi) - R_2\cos(\theta_2))^2 + \\ + (y + h_2\sin(\varphi) - R_2\sin(\theta_2))^2 = r_2^2 \quad (2)$$

$$(x + h_3\cos(\varphi+\alpha) - R_3\cos(\theta_3))^2 + \\ + (y + h_3\sin(\varphi+\alpha) - R_3\sin(\theta_3))^2 = r_3^2 \quad (3)$$

Making an algebraic manipulation of Eq. (1), (2) and (3), the following expressions can be achieved:

$$x = \lambda(\theta_1, \theta_2, \theta_3, \varphi) \quad (4)$$

$$y = \mu(\theta_1, \theta_2, \theta_3, \varphi) \quad (5)$$

And finally, introducing Eq.(4) and (5) into Eq.(1) an equation like the following is obtained:

$$\zeta(\theta_1, \theta_2, \theta_3, \varphi) = 0 \quad (6)$$

Once the geometric parameters are defined, Eq.(6) can be used to solve the DKP (with Eq.(4) and (5)), which is known to have multiple solutions. Given the values of the input variables θ_i it is possible to find several ways of assembling the mechanism, defined by different values of the output variables x, y and φ. This kind of manipulator can have a maximum of six different DKP solutions.

3 CONFIGURATION SPACE

The configuration space of a mechanism is the loci of postures in a mixed domain which includes input and output variables simultaneously. Its projections onto the input and output variables spaces are the joint space and the workspace respectively. For a three degrees of freedom non redundant manipulator, like the example proposed, this is a six dimensional mathematical entity, which cannot be graphically represented in general. However, due to the special geometric characteristics of this example, an entity similar to the general configuration space, but reduced to just three variables can be obtained. Therefore, this reduced configuration space could be displayed in a three dimensional space.

Taking constant one input variable in Eq.(6) it is achieved an equation that relates one output variable with the remaining two input variables. The graphical representation of this equation is a 3D surface. This reduced configuration space will be different according to the constant value assigned to the input variable. However, in the proposed example, as the three fixed revolute joints are coincident at the same point, the shape of the surface will be the same for any constant value assigned to the input variable. such parameter. Different values of the input variable taken constant result in a translation of the surface, but it always keeps the same shape. In this case, the whole configuration space and the reduced one provide the complete information.

By taking a constant value of the input variable θ1 in Eq.(6), the configuration space equation is obtained. This equation relates the output variable φ with input variables θ2 and θ3, namely:

$$\zeta(\varphi, \theta_2, \theta_3) = 0 \tag{7}$$

Configuration space for the manipulator in Fig.1 is shown in Fig.2. In this case it is composed of two closed disjoint surfaces.

This entity and its projections onto the joint space and workspace can be used to plot the IKP and DKP singularity loci and locate the multiple DKP solutions. Multiple solutions of the DKP are the intersections of this surface with a vertical line, defined by a given value of input variables θ2 and θ3. Any motion of the robot can be plotted as a path over the configuration surface. DKP singular configurations correspond to those points in the surface with horizontal normal (or vertical tangent plane). At these postures several DKP solutions (intersections) coalesce to one solution with multiplicity two (normally) or higher. Therefore, DKP singularity locus is defined by curves given by:

$$\zeta(\varphi, \theta_2, \theta_3) = 0 \tag{8}$$

$$\frac{\partial \zeta}{\partial \varphi} = \xi(\varphi, \theta_2, \theta_3) = 0 \tag{9}$$

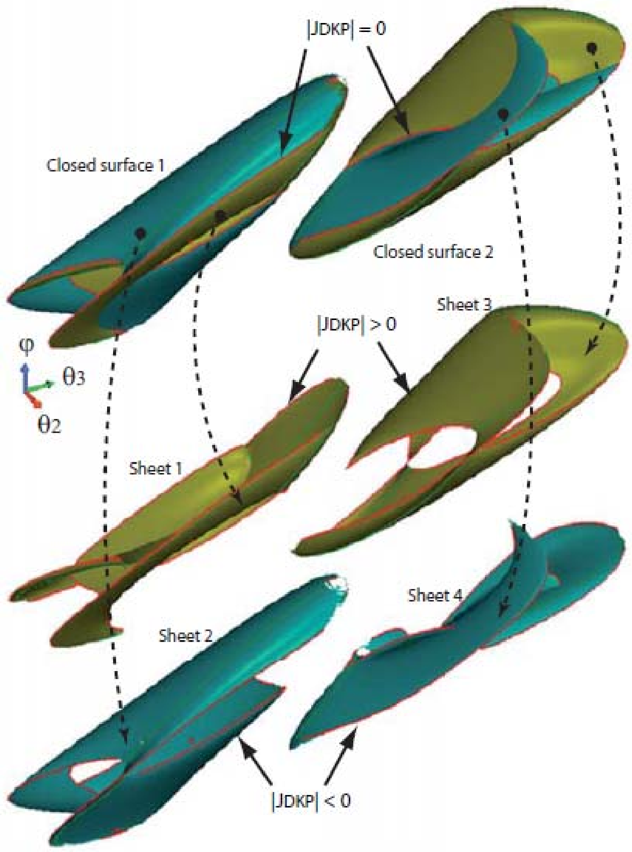

Figure 2 3-<u>R</u>RR manipulator configuration space.

DKP singularity curves are associated with postures where |JDKP| vanish and divide the configuration surface into parts with different sign of |JDKP|. Therefore those parts, called sheets of the configuration space, depicted in Fig.2, remain free of internal DKP singularities. The robot can move inside each of these sheets without losing control. Configuration space sheets are crossed by IKP singularity curves. Crossing one of these curves imply reaching a workspace boundary to make a transition from one working mode (IKP solution) to another. Such a position has manipulability restrictions but it does not imply a loss of control.

4 A NEW CONCEPT OF ASSEMBLY MODE

Three types of transitions between two different DKP solutions can be found. Transition type depends on the relative placement of these solutions on the configuration surface sheets. If both solutions are located at disjoint surfaces of the configuration space (Fig.3), the mechanism needs to be disassembled to change between them.

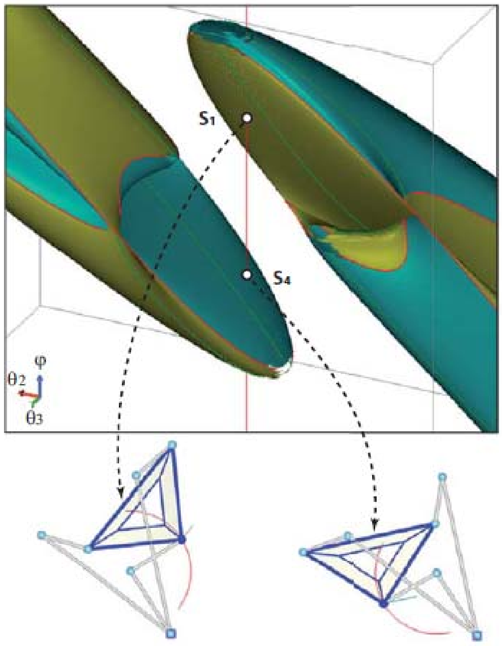

Figure 3 Transition between solutions on disjoint surfaces.

If they are on the same surface but on adjacent DKP-singularity-free sheets, namely two sheets separated by a DKP singularity curve (Fig.4), both solutions can be joined without disassembling the mechanism. However, the transition path will reach a DKP singularity where the robot losses its stiffness, because three bars B_iC_i intersect simultaneously at the same point [1]. Therefore, both of these types of transitions cannot be performed while the manipulator is normally working.

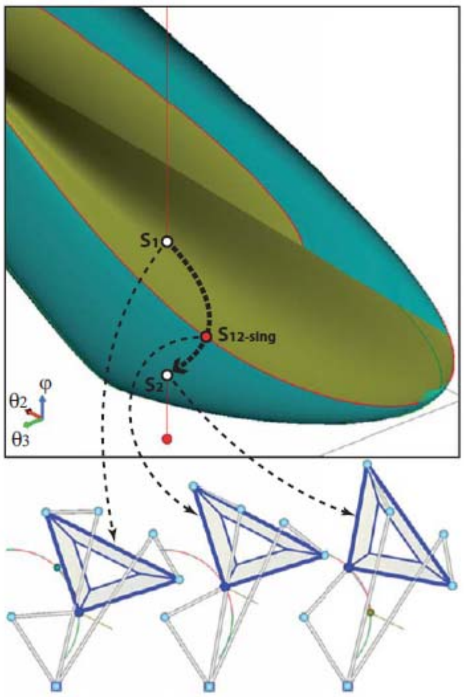

Figure 4 Transition between solutions on adjacent sheets.

The initial hypothesis established that to make an assembly mode changing it is needed either disassembling the manipulator or crossing a DKP singularity [2]. This is the case of the first two types of transitions between DKP solutions explained in this section. However, later works [3] [8], proved that this assumption is not always verified. There were found examples of manipulators with the ability of making non-singular transitions between some DKP solutions. This is the third type of transition proposed here.
This type of transition takes place when both solutions are in the same DKP-singularity-free region, i.e. in the same configuration space sheet (Fig.5). In this case solutions can be joined by a path completely included in such sheet, so a DKP singularity is never reached. This phenomenon is known as non-singular assembly mode changing, because DKP solutions are traditionally called assembly modes.

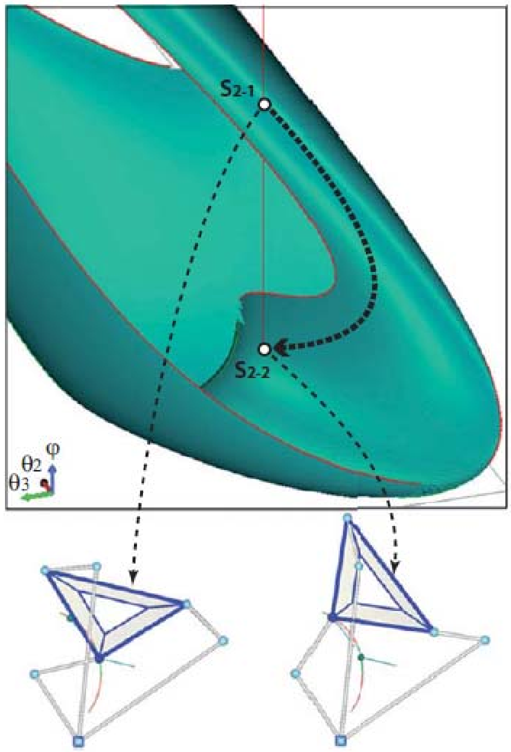

Figure 5 Transition between solutions on the same sheet.

This circumstance introduces the need for a differentiation between the concept of assembly mode and DKP solution. Two DKP solutions in the first and second type of transitions are clearly distinguishable. This differentiation agrees with the classical concept of assembly mode, namely those DKP solutions the manipulator cannot join itself. However, in the third type of transition, joined DKP solutions cannot be distinguished in practice. The transition is completely continuous and smooth so there is no way to distinguish when exactly the formerly known as assembly mode is changed. Therefore, in this third case both DKP solutions could be considered as belonging to the same assembly mode.

Consequently, DKP solutions are simply the different mathematical solutions of the constraint equations system and the number of assembly modes is the number of sheets into which the configuration space is divided by DKP singularity loci. Therefore, an assembly mode can be composed of more than one DKP solution, e.g. those which can be joined without losing control.

5 A LARGER WORKSPACE MERGING ASSEMBLY MODES

For the manipulator proposed in Fig.1 the configuration space is plotted in Fig.2. For the given values of geometric parameters, the configuration surface is divided in two closed and disjoint surfaces. Each closed surface is divided in two sheets by DKP singularity curves. According to the definition given in the previous section there are four assembly modes (four sheets). The fact that the configuration surface is divided in two disjoint surfaces implies that the manipulator needs to be physically disassembled to change among some of its assembly modes.

The configuration space equation, or the configuration surface shape, changes with the values of geometric parameters, i.e. dimensions of the manipulator. Making an adequate modification of the manipulator geometry a workspace enlargement can be achieved by means of assembly modes merging. This strategy aims to join in one those assembly modes which require the mechanism disassembling to be reached. Modifying the values of some geometric parameters, the two disjoint closed surfaces of the configuration space merge in a single closed surface. For example, in the manipulator considered in Fig.1, if the value of R_1 is modified from 11 to 9, the configuration space evolves to a single closed surface, shown in Fig.6.

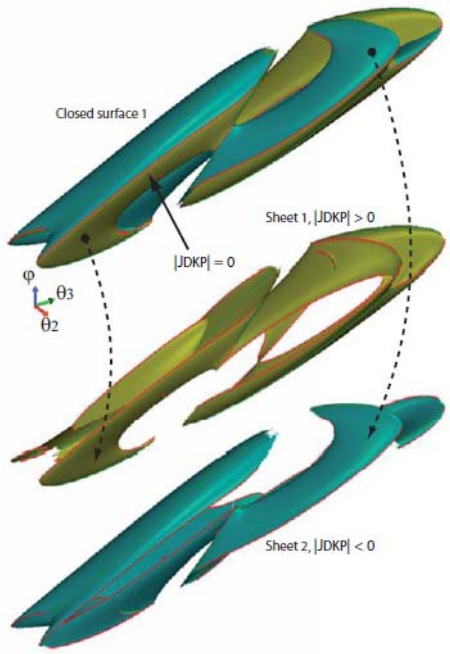

Figure 6 Enlarged workspace.

DKP solutions are always equally divided into sheets associated to $|J_{DKP}|$ positive and negative. This fact implies that assembly modes are always even numbers. This procedure consists in merging all sheets associated to the same $|J_{DKP}|$ sign in a single sheet. The final result is a mechanism with just two assembly modes. Both assembly modes are separated only by DKP singularity curves. In this case, each assembly mode can contain from one to three DKP solutions.

6 DKP-SINGULARITY-FREE TRANSITIONS BETWEEN DKP SOLUTIONS

As it has been shown, the configuration space representation is the best approach to understand the controllable transitions among DKP solutions. In order to find the mathematical conditions which enable transitions without crossing a DKP singular posture, the representation of the DKP singularity loci in the joint space will be also used. The configuration space and the joint space can be simultaneously displayed since the joint space is the projection of the configuration space onto the input variables domain, i.e. $\theta_2\theta_3$ plane.

When a sheet of the configuration space contains more than one DKP solution is because that sheet is folded in such a way that a vertical line is able to intersect with it in more than one point. Those intersections are the DKP solutions which can be joined without losing control. The boundary of a configuration space sheet is always a DKP singularity curve, which corresponds with those points on the surface whose normal vector is horizontal.

Two examples of foldings on the surface verifying these conditions will be shown next, the traditional cuspidal folding and the new helicoidal folding.

When the constraint equations (1), (2) and (3) have a root with multiplicity three, the configuration surface folds as shown in Fig.7. In such a fold the surface goes from having three intersections with a vertical line to just one. At that point, where three solutions coalesce to the same one, the solution has multiplicity three. Due to the shape of the folding, it is possible to figure out paths over the sheet where two of the intersections are located, which join them avoiding the DKP singularity curve. Obviously those paths must encircle the triple coalescence point C of the surface as shown in Fig.7 and Fig.8.

Such points are located on the singularity curve. Considering the projection of the singularity curves onto the joint space (Fig.7 and Fig.9), the solution with multiplicity three appears as a cusp point C. This is the reason why the non-singular transition between DKP solutions described is a path encircling a cusp point in the joint space.

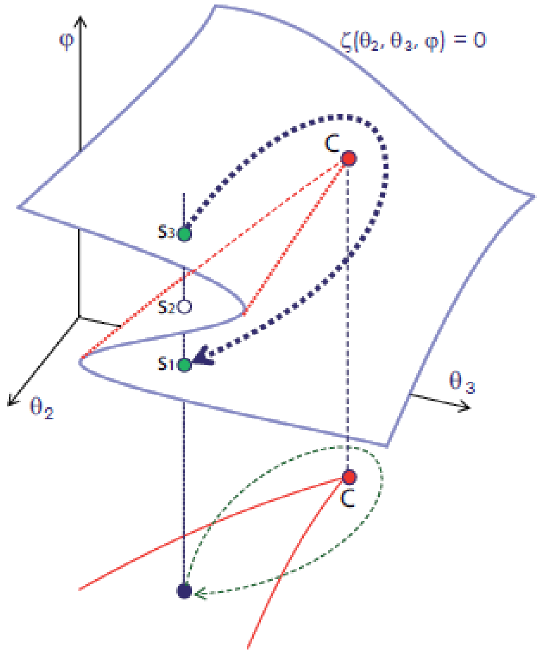

Figure 7 Schematic cuspidal folding.

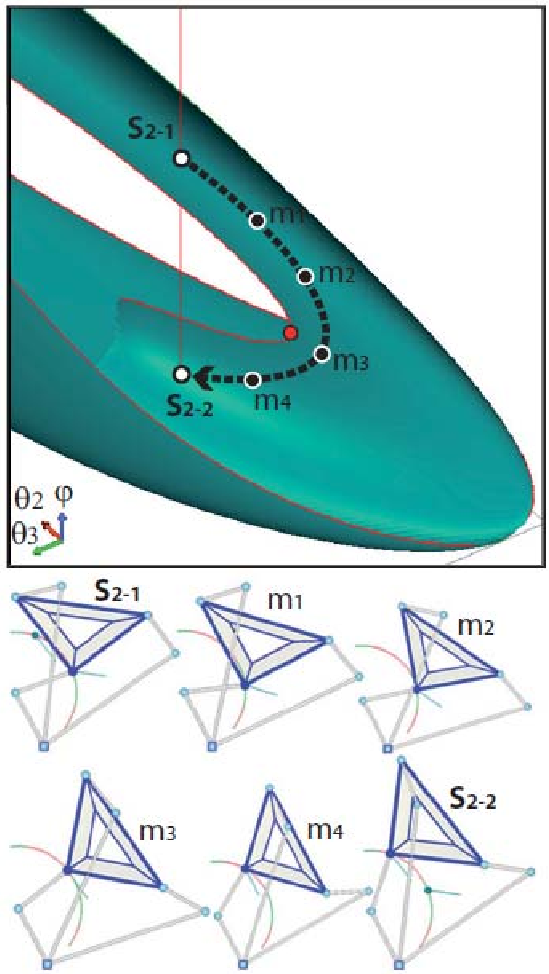

Figure 8 Non-singular transition on a cuspidal folding.

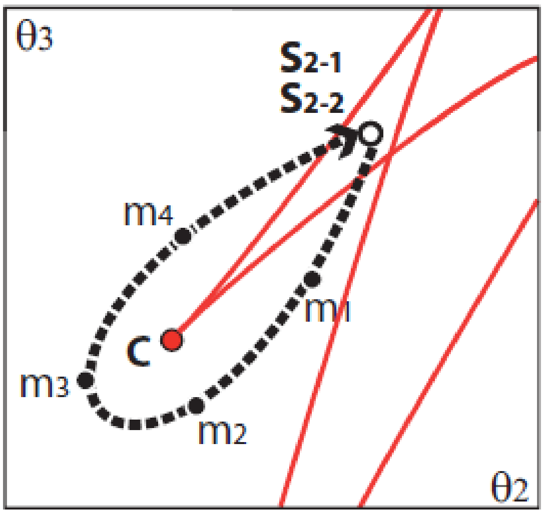

Figure 9 Encircling a cusp point in the joint space.

Taking into account these concepts, the typically referenced way to make DKP-singularity-free transitions is encircling a cusp point. Nevertheless, the computation and representation of the configuration space, as well as the visualization of non-singular transitions over this surface allow the extension of this idea. It is possible to figure out, at least theoretically, other types of folding the configuration surface in such a way that several DKP solutions are found in the same DKP-singularity-free sheet and the transition among them does not imply any threefold point. This would be the case of a helicoidal folding shown schematically in Fig.10, [7]. The configuration surface obtained in Fig.6 presents this characteristic, as detailed in Fig.11.

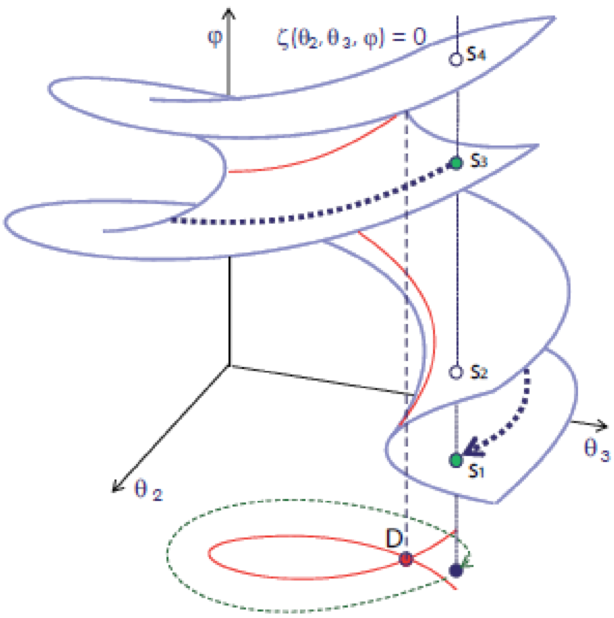

Figure 10 Schematic helicoidal folding.

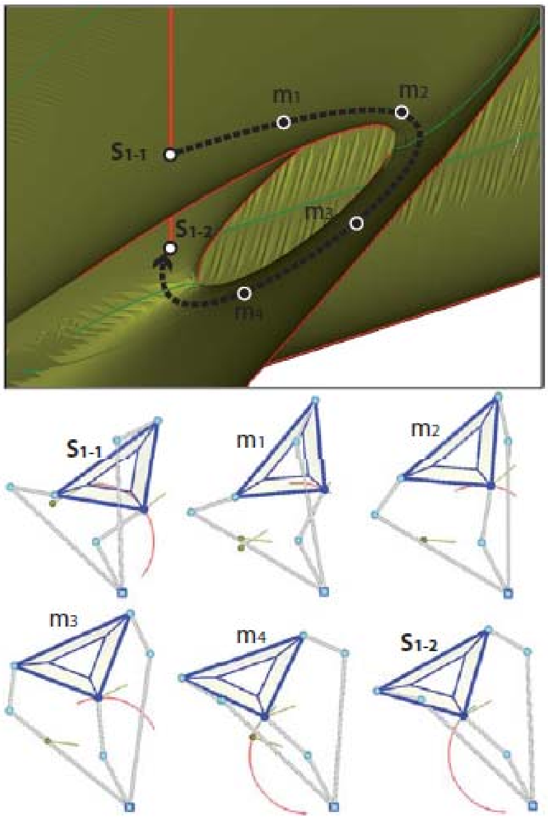

Figure 11 DKP -singularity-free transition on a helicoidal folding.

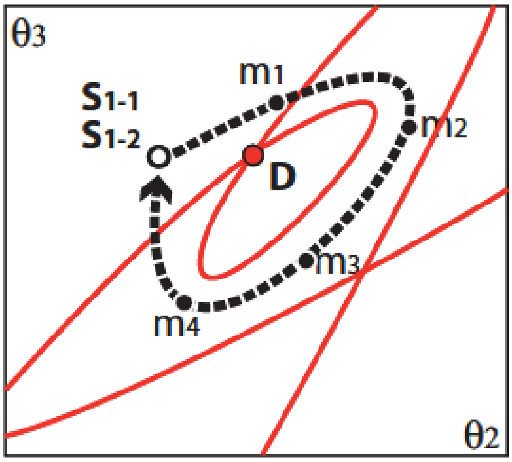

Figure 12 Encircling a loop defined by a double point in the joint space.

In the case of a manipulator presenting multiple IKP solutions like this one, each sheet is composed by several adjacent regions associated with the different working modes of the manipulator. These regions are separated by the IKP singularity curves. When postures with $|J_{IKP}|=0$ are reached, a dependence among the output velocities is achieved, so there are manipulability restrictions, but this does not imply a risk of uncontrollability as in a DKP singularity. Moreover, these postures allow the transition between regions associated with the eight different working modes of this manipulator, enlarging the practical workspace. The path shown in Fig.11 crosses IKP singularity curves, so it may not be theoretically considered a non singular transition between two DKP solutions, but since it is completely contained in a DKP-singularity-free sheet, the control of the robot is never lost.

When the configuration surface has a helicoidal folding, in both sheets, which share the singularity curve that defines the folding, it is possible to find two pairs of DKP solutions which can be joined by DKP-singularity-free paths, as shown in Fig.10 (s_3 and s_1, or s_4 and s_2). In the projection onto the joint space these paths must encircle a loop in the singularity curve. Such a loop is defined by the existence of a double point, D, in such planar curve shown in Fig.12.

The projection of the singularity curves on the $\theta_2\theta_3$ plane can be obtained as an equation which comes from the elimination of the output variable φ from the system of equations (9):

$$\psi(\theta_2,\theta_3)=0 \qquad (10)$$

In this curve there are some points associated to special singular configurations. Cusp points are defined by solutions with multiplicity three. A double point in the curve can be also considered as a special singular configuration. In such a point constraint equations have a couple of double solutions, namely two different solutions with multiplicity two.

Mathematical conditions verified in a double point are:

$$\frac{\partial\psi}{\partial\theta_2}=\frac{\partial\psi}{\partial\theta_3}=0 \text{ or } \infty \qquad (11)$$

A cusp point verifies the same conditions. In fact, the proposed approach states that the existence of these loops and their associated double points are actually a more general mathematical condition than the existence of cusp points, since the latter are a degeneracy of the former.

7 CONCLUSIONS

The concepts presented in this paper allow a better understanding of how different solutions of the DKP, traditionally called assembly modes, can be joined via DKP-singularity-free paths, and hence without disassemble the mechanism. It has been presented a practical tool which allows knowing in an easy and quickly way if a mechanism has the ability of doing this. It has been proved that encircling a cusp point is not the only way of making a non-singular assembly mode change. A more general way to do this is encircling a loop in the singularity curves plotted in the joint space. This loop is defined by the existence of a double point. A cusp point is a degeneracy of such loop.

It would be interesting to find a way of posing the mathematical conditions in a symbolical form and then obtain the relations among the different geometric parameters of the manipulator which ensure the capability of passing among certain DKP solutions. This information would be very important in the design phase of the manipulator. Moreover, it has been introduced the reason why the concept of assembly mode should be redefined. The representation of the configuration space also gives information about the possibility of merging several assembly modes in order to obtain a larger practical workspace.

REFERENCES

[1] Chablat D. and Wenger P., The kinematic analysis of a symmetrical three-degree-of-freedom planar parallel manipulator. *Proc. of ROMANSY 2004*, Montreal (Canada), 2004.

[2] Hunt K. and Primrose E., Assembly configurations of some in-parallel-actuated manipulators. *Mechanism and Machine Theory*, Vol. 28 (1), pp.31-42, 1993.

[3] Innocenti C. and Parenti-Castelli V., Singularity-free evolution from one configuration to another in serial and fully-parallel manipulators. *Journal of Mechanical Design*, Vol. 120, 1998.

[4] Maass J., Kolbus M., Budde C., Hesselbach J. and Schumacher W., Control strategies for enlarging a spatial parallel robot's workspace by change of configuration. *Proc. of the 5th Chemnitz Parallel Kinematics Seminar*, April 25-26, pp.515-530, 2006.

[5] Macho E., Altuzarra O., Pinto C. and Hernandez A., Singularity free change of assembly mode in parallel manipulators. Application to the 3-RPR planar platform. *Proc. of 12th World Congress in Mechanism and Machine science*, Besançon (France), 2007.

[6] Macho E., Altuzarra O., Pinto C. and Hernandez A., Workspaces associated to assembly modes of the 5r planar parallel manipulator. *Robotica*, Vol. 26(3), pp.395-403, 2008.

[7] Macho E., Altuzarra O., Pinto C. and Hernandez A., Transitions between solutions of the direct kinematic problem. *Advances in Robot Kinematics*, June 22-26, Batz-sur-Mer (France), 2008.

[8] McAree P. and Daniel R., An explanation of never-special assembly changing motions for 3-3 parallel manipulators. *The International Journal of Robotics Research*, Vol. 18(6), pp.556-574, 1999.

[9] Mohammadi Daniali H.R., Zsombor-Murray P.J., and Angeles J., Singularity analysis of planar parallel manipulators. *Mechanism and Machine Theory*, Vol 30(5), pp.665-687, 1995.

[10] Zein M., Wenger P. and Chablat D., Singular curves and cusp points in the joint space of 3-RPR parallel manipulators. *Proc. of the 2006 IEEE International Conference on Robotics and Automation*, Orlando, 2006.

[11] Zein M., Wenger P. and Chablat D., Non-singular assembly mode changing motions for 3-RPR parallel manipulators. *Mechanism and Machine Theory*, Vol. 43(4), pp.480-490, 2007.

ACKNOWLEDGMENTS

This research work was supported in part by the Spanish Ministerio de Ciencia y Tecnologia (Project DPI2008-00159), the FEDER funds of the European Union, the University of the Basque Country (Project GIU07/78) and the Grant (BFI104.148.R2) from the Basque Government.

ISSN 1590-8844
International Journal of Mechanics and Control, Vol. 10, No. 01, 2009

LOT SIZE ONE IN THE MASS PRODUCTION AND PRECISION ASSEMBLY OF CYLINDER LOCKS

Wolfgang Mann, Georg Peschl, Arne Sieber and Christian Wögerer*

* Profactor Research and Solutions GmbH – Seibersdorf, Austria

ABSTRACT

This paper describes the research and development of a precision assembly process for cylinder locks that can be used from mass production down to lot size one. Each lock is a very tight tolerated assembly group and has its own unique combination files. That fact results in a high effort in designing the mechanical parts and the data management in the background. The highly complex cylinder locks consist of very small parts whose tricky detection requires analysis based on six-sigma approaches. Profactor Research and Solutions GmbH has developed a Europe wide unique automated plant that is offering maximized flexibility in the assembly of cylinder locks and for the process required accuracy and precision to handle in total 60 different parts including tumblers and miniature springs. A cycle time of 75s for a cylinder lock assembly was achieved. Requiring an area of just 2x2m the main process of that plant is a very good example for a desktop factory.

Keywords: Lot size one, precision assembly, Six Sigma, total flexible automation, process capability, desktop factory, cylinder locks

1 INTRODUCTION

The main aim of the present work was to develop a plant for automated assembly of cylinder locks of an Austrian lock manufacturer with worldwide markets. Next to being able to handle all kinds of different locking systems of the customer, the machine must additionally be ready for new generations of locking systems with geometrical modifications, thus requiring maximum flexibility in the assembly process.

Next to the fully automation also an integration into the Computer Integrated Manufacturing (short CIM) - System of the customer was required. The CIM supplies the information of the combinations for each cylinder lock. Moreover the current production state is reported continuously to the CIM during the whole assembly process.

The main challenges of the project are the high-precision assembly process of a variety of micro-parts that differ in diameter and length and the complex data processing between SoftSPS and robots and between SPS and the customer's host computer.

Contact author: Georg Peschl

E-mail: georg.peschl@profactor.at

Profactor Research and Solutions GmbH meets these challenges of precision assembly processes and developed a plant, which is in Europe the first plant providing this flexibility. To maximize the plants throughput, two assembly robots and two additional robots for a separate supply of parts were integrated in the setup.

2 BASICS ABOUT CYLINDER LOCKS

The main task was to develop a high speed precision assembly process for a large variety of parts. This process has to be able to able to handle 60 parts like pins and tumblers that differ in length and diameter (figure 1). Next to that, also a complex miniature spring has to be processed, for which first of all a process capability had to be verified.

Figure 1 Pins, tumblers and spring.

The components have to be inserted into holes, which are situated multidimensional over the lock insert surface. An insert is made of three main components – stator, hull and rotor (figure 2, top row, from left to the right).

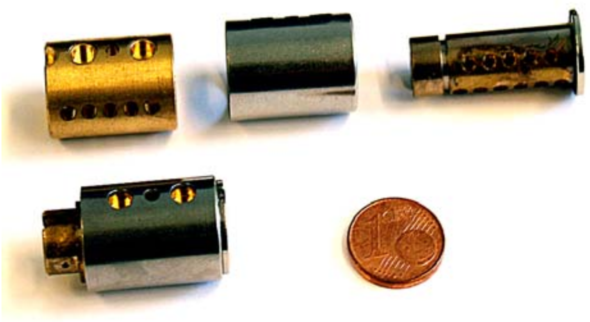

Figure 1 Parts of an Insert

Every alignment on the insert consists of n dill-rows with b drills. In total six different product groups with different drill alignments have to be processed.

A very interesting and important aspect of that plant is the possibility of mass production down to lot size one. Lot size one in this context means that every cylinder lock has its own unique combination of separate parts with different spreading on the rotor.

The first development step was dedicated to the implementation of a prototype to perform functional tests. In those the interaction of components e.g. grippers and insert-manipulation units, on the one hand, and the process stability at cycle times of max 75 sec per assembly, on the other hand, had to be verified.

After successful prototype tests this construction was duplicated and assembled twice in the final plant combined with some new elements. Two supply-robots, one portal-system for handling the inserts and four buffer magazines for a fast supply of the required pins, tumblers and springs have been added.

The assembly information about the lock combinations are provided by the customers CIM-System.

3 PROCESS DESCRIPTION

The assembly process starts with placing the inserts in a work piece holder (figure 3). Then the holder is placed on a conveyor belt and transported to a scanner which reads the work piece holder number and transmits it to the CIM. From there, the assembly information is transferred to the plant which is detailed in chapter 0. After finishing the transfer, the work piece holder is transported into the machine on a conveyor belt. To save part changing time, two belts are used in parallel. During normal operation at least one work piece holder is in the machine.

Figure 2. Work piece holder and part of the handling system

After the work piece holder has reached the processing position, the portal handling system places an insert in the manipulation unit. Due to the layout and the large amount of different parts a direct assembly of the parts is not possible. Thus supply of the pins and tumblers is performed via buffer magazines. These buffer magazines are filled fully automatically via two supply robots. A pipeline concept, where two magazines are filled while the parts of the two other ones are assembled, assures highest capacity utilization of the supply robots which in the end saves cycle time.

After the buffer magazines are filled, they are driven to the assembly robots where the actual assembly process starts. Springs are supplied via an extra magazine, which carries enough springs for one shift (figure 4).

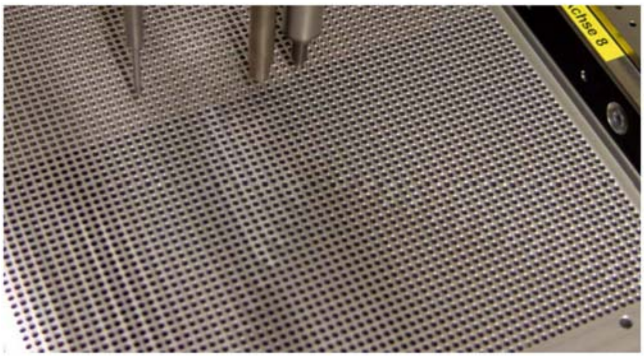

Figure 3 Spring-magazine

3.1 ASSEMBLY ROBOT

The actual assembly robot unit is the result of an updated prototypical experimental setup construction. One unit consists of a twin arm SCARA-Robot, [RP-5AH, Mitsubishi] a linear and a rotary axis. Each drill position of an insert can be reached with this combination. The two additional axes are connected and controlled by the robot controller.

After placing an insert in the manipulation unit (figure 5) the linear axis pulls the insert into the assembly position and the hull of the insert is synchronously peeled off. During the linear movement, the lock assembly is turned around its longitudinal axis and positioned at the first drill.

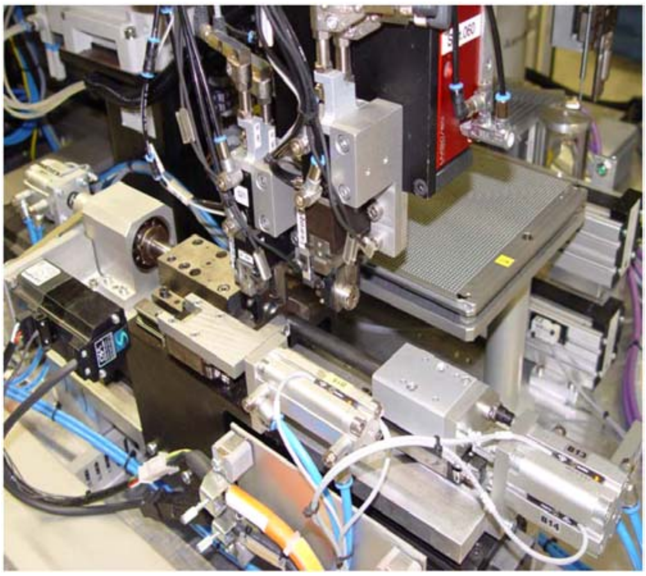

Figure 4. Insert change at manipulation unit

When a buffer magazine arrives at the assembly robot station, the process starts with the tumbler- and spring gripper picking a spring from the spring magazine. In the next step a tumbler and a pin are collected from the buffer magazine. The presence of all parts during and a correct picking is verified with a high sensitive pressure sensor during the whole process.
Prior to the filling of a new row, a centering pin, fixed on the robot arm, aligns the drills in rotor and stator concentrically. After the centering step the pin is placed into the drill, followed by the tumbler together with the spring. A special designed gripper avoids damage to the springs during the repositioning to the next drill.
After finishing a cylinder lock assembly, the buffer magazines change the position (full magazine to the assembly robot, empty magazine to the supply robot). In parallel to that the cylinder lock assembly is turned back to its initial position and pushed out of the manipulation unit into the hull. The portal system returns the assembled inlet to the work piece holder and picks up a new one. If all inlets are assembled, the actual work piece holder is replaced with a new one.
Figure 5 shows an assembly robot taking parts from the buffer-magazine, in the bottom right corner is the manipulation unit apparent.
To maximize the final plants throughput, two assembly robots are processing in parallel two work piece holders.

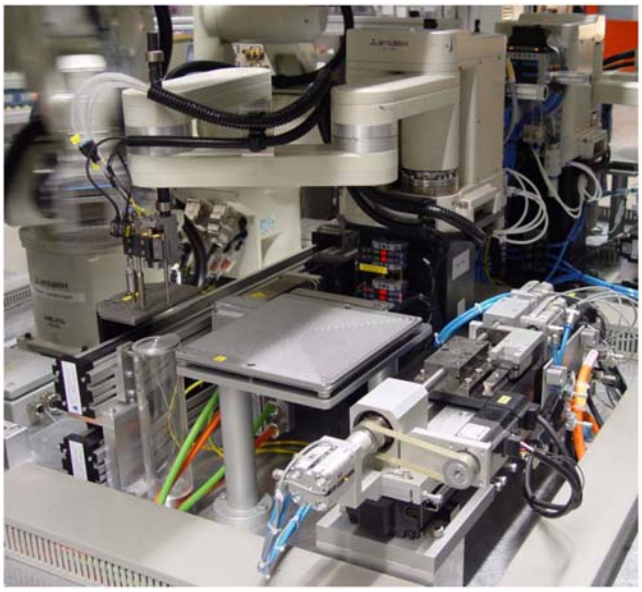

Figure 5. Assembly robot, manipulation unit and buffer-magazine

3.2 SUPPLY ROBOT

Two articulated robots [Mitsubishi RV-6S] manage the collecting of the pins and tumblers which are required for the assembly process. The parts are collected from spiral stacks arranged in an “arena-like” layout around them figure 7).
One robot is dedicated to the pins and the other to the tumblers. Each robot is filling one half of a buffer magazine. After finishing that job, the magazines are exchanged so that the other robot can complete the buffer. The breakup into tumbler robot and pin robot facilitates taking care of the attributes of the different part-types.

Figure 6. Supply robot in the arena

ISSN 1590-8844
International Journal of Mechanics and Control, Vol. 10, No. 01, 2009

After finishing the filling process the two magazines are kept in a waiting position until two empty ones return from the assembly robots.

4 TOLERANCE DESIGN

Prior to the mechanical designs a tolerance analysis was performed for the most important mechanical interfaces. Based on this the components were selected and then designed and/or purchased.
The centering pin is a good example to show the advantages and the function of the tolerance analysis. A centering pin is required as the rotor and the stator may be slightly missing aligned. Additional to this fact, not all drills are concentric to the drill of the manipulation unit. The inserts are pre-aligned but through the different steps in the handling a 100% correct pre-alignment is impossible. The information from the tolerance analyses helps to design the centering pin in order to adjust all tolerances.
Tab 1 show how important a centering step can be and how the different clearances look like. Minimum and maximum clearance represents the concentricity of the drills in rotor and stator. A negative value means that the drills are misaligned.

Tab. 1. Tolerance analysis

	Maximum clearance	**Minimum clearance**
Without centering	-0,119mm	-0,142mm
With centering	0,057mm	0,016mm

5 REQUIREMENTS TO THE ROBOTICS

Small tolerances of the inserts require high precision assembly processes. In addition to that, tolerances of the manipulations units and other parts have to be considered: Robots with a high basic precision are required.
A very good example is the assembly robot: the sensible assembly process requires high accurate positioning on the one hand and fastest processing times on the other. To meet these requirements, a twin arm SCARA [Mitsubishi RP-5AH] was chosen as already mentioned before. This kind of robot is able to reach the desired positions very fast and accurately. High precision is important to eliminate the possibility of assembly errors as a result of robot inaccuracy.
As supply robots, two articulated robots were chosen [Mitsubishi RV-6S]. They have a large workspace, but their end position is at high speeds not as accurate as that from the SCARAs. Thus final positioning takes place at a reduced speed. As described above, buffer magazines are filled in parallel to the assembly process – in total four magazines are used – which helps to increase the overall assembly speed.

6 PROTOTYPE

Figure 8 details the prototype consisting of all main assembly process essential components except the supply robots and the portal handling system.

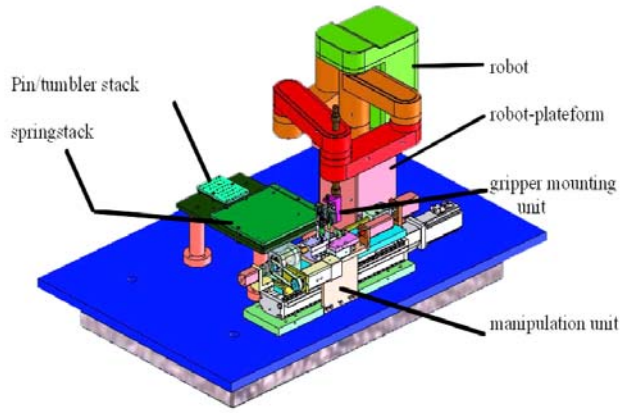

Figure 7. Scheme of the prototype

The background of the prototype was to show that the process is stable enough for continuous production and signal possible problems and conflicts at an early stage.
Next to first assembly trials, tests on the interaction between the mechanical components and the sensors were included. There the main challenge turned out to be the reliable detection and verification of a correct gripping of the miniature spring.

6.1 SENSORS

As explained before, pins, tumblers and springs are picked with a suction gripper. For the detection of a picked object, a pressure sensor is incorporated- Detection of a pin or a tumbler is quite easy in comparison to the detection of a spring. A special sensor had to be chosen [Keyence AP-44] for this application which is able to detect the small pressure drops.
This precise sensor in combination with a precision pressure regulator - to ensure a stable supply pressure for the vacuum generator - makes it possible to detect the springs.
The thresholds for the spring detection algorithm were found with the help of a six-sigma-approach. Several tests were performed to find a representative value for the pressure limits. A correct initial pressure is the only precondition for detecting most of the springs.

6.2 GRIPPER UNIT

The core components of the gripper unit (figure 9) of the assembly robot are two single-grippes, one for the pins (figure 11) and the other one for the springs and the tumblers (figure 10). A third element is the centering pin.

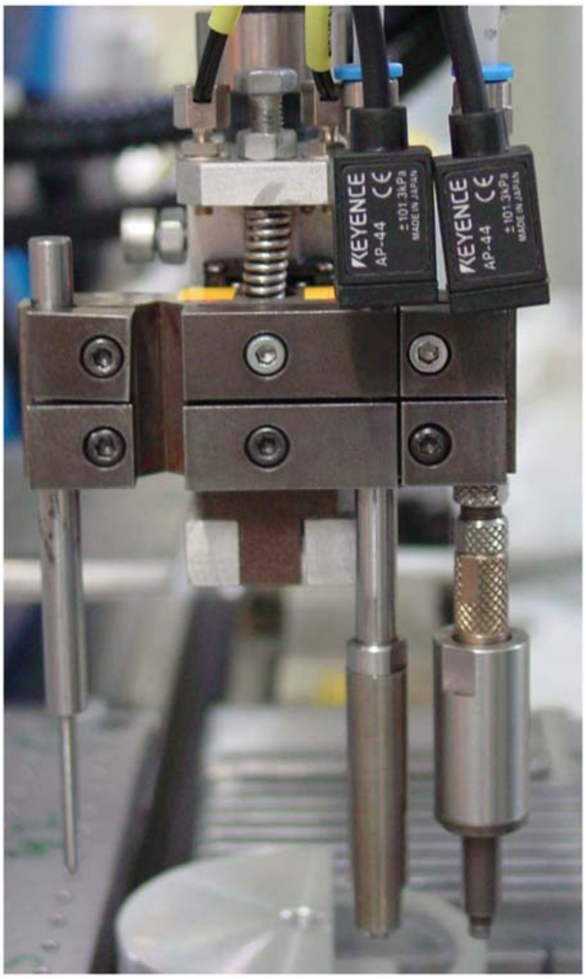

Figure 8 Centering pin, pin gripper, tumbler and spring gripper

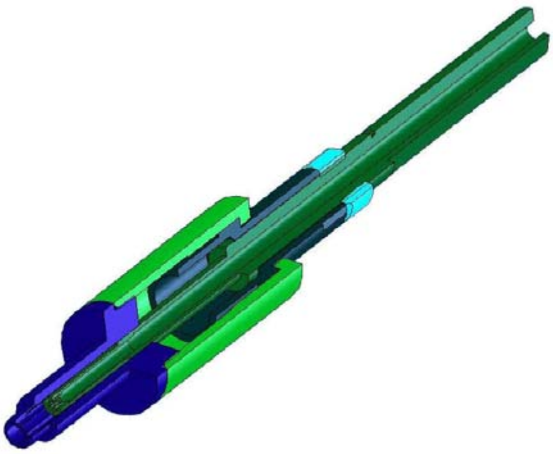

Figure 9. Spring- and tumbler Gripper

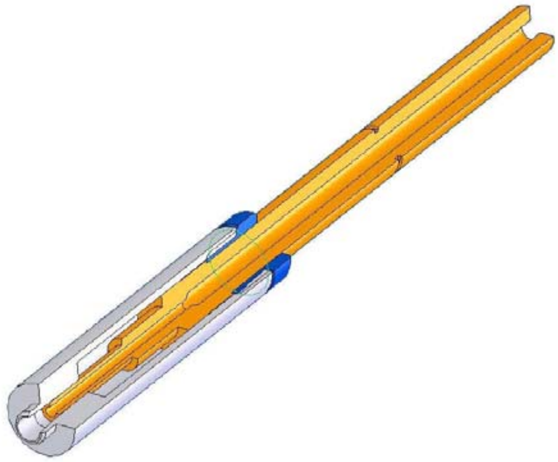

Figure 10. Pin gripper

These 3 mechanical elements are held by a spring mounted chassis. Additionally to the mechanical elements different sensors are integrated in the gripper unit. They allow measuring the pressure in the grippers and the z-offset between the grippers and the robot arm with an accuracy of 0,1mm. This is necessary to avoid collisions in z-direction and to check if a part is placed in the right order. This z-offset is possible as the unit allows a relative movement between two components.
This gripper unit turned out to be mechanically reliable and precise, thus the design was also used for the gripper development of the articulated supply. The major difference to the assembly robot gripper unit is that to maximize performance 6 gripper pairs are mounted in parallel (Figure 12). Figure 13 shows the side view of the gripper with the 6 pressure sensors.

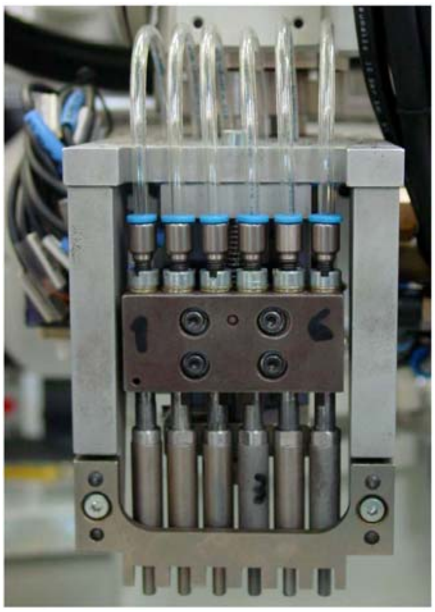

Figure 11 Gripper of the supply robot (front view)

ISSN 1590-8844
International Journal of Mechanics and Control, Vol. 10, No. 01, 2009

Figure 12 Gripper of the supply robot (side view)

7 CONTROL TECHNIQUE

The handling of the large amount of product variations and the high complexity of the locks requires a sophisticated data-management in the background. Fig 14 shows details the information flow between the different components

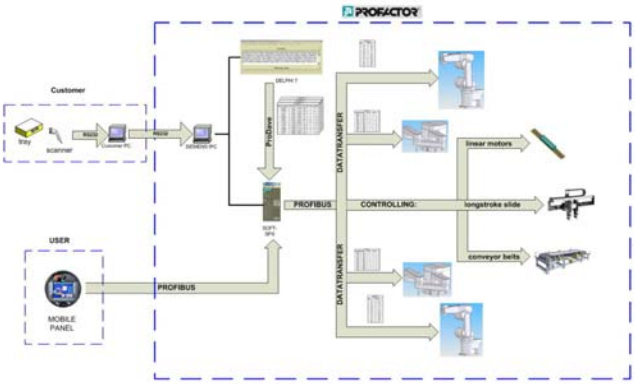

Figure 13. Dataflow

7.1 DATAFLOW OF THE ASSEMBLY INFORMATION

The assembly information is centrally administrated by the customer and provided to the plant via a serial connection. After identifying a work piece holder by reading it's code, the assembly information is downloaded from the server. At the same time, the customer's CIM-system calculates the part consumption and books it on the server.
After the serial data transfer to the plant-side Industrial PC is finished, this information has to be processed. Therefore a special application was developed under Delphi [Borland]. Figure 15 shows the graphical user interface. This application receives the data from the serial connection, splits the string into part and geometry information and performs a CRC check. Then the assembly information is sent to the SoftSPS (WinAC-RTX , figure 16).
The second task of this application is giving continuously feedback about the production state to the customers' CIM.

Figure 14. Delphi program

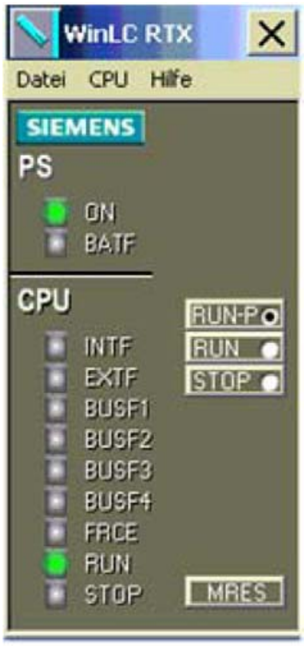

Figure 15. SoftSPS running on IPC

The SPS receives the information and writes it into a temporary buffer. From there the information is moved into one of two arrays ready to be distributed to one of the two assembly plants. Work piece holder and assembly information are always connected to each other by software. As soon as one workpiece holder is finished, the assembly information from the previous job is cleared and updated then with the new data from the temporary buffer. Then a conveyor belt is chosen to drive a new work piece holder to the assembly robot.
After the data processing by the SPS, all following transfers to the robots will be performed via Profibus.

7.2 ADDITIONAL TRAFFIC ON THE PROFIBUS

The plant is controlled by SoftSPS. Thus a bus system is the best basis for interfacing additional periphery like the six linear axes, IO-elements, pneumatics, the mobile operator panel and, of course, the four robots. Besides the standard bus-traffic, the assembly information and the robot messages about their spring stock and operating status are also transferred via Profibus. All this data transfer lead to a very high utilization of the bus nearly on its limits.

7.3 DATA MANAGEMENT

With the present plant it is possible to administrate three work piece holders at the same time. While two of them are already processed in the plant, one is at the scanner position in a waiting position.

Each of the three work piece holders carries 60 inserts. For 60 inlets 350000 assembly information are needed and stored in the buffers. Each insert on the work piece holder is clearly identified through a number. With that number all information in the array, all buffer magazines and all following processing steps are connected together.

It is a challenge for a SPS-application to manage all that data and provide information for all units in the right time window

7.4 OPTIONAL OPERATIONS MODES

Parallel to the standard operation with both assembly robots the customer can choose alternative operation modes where only one assembly robot is used. That is the case during maintenance of a robot, as in such a way the production does not need to be stopped completely. In that operation mode all inserts in the work piece holder are processed by only one assembly robot.

8 RESULTS AND CONCLUSION

Profactor Research and Solution GmbH succeeded in developing a plant (figure 17) which meets all the customers' requirements and is able to assemble all currently available parts without problems.

Typical cycle time for one lock assembly is 75 sec, The actual unit is operating 24h/day. It has been in operation since December 2007. In these last 10 months more than 250000 cylinder locks were already successfully assembled.

The assembly process is highly flexible as it is based on the one piece flow concept for lot size one. Due to this outstanding flexibility, also lock design changes can be handled easily.

Figure 16. Plant in operation

9 OUTLOOK

The knowledge and experience gained during the development of the plant will be used in future projects to follow the trend towards a desktop factory. These concepts allow a highly flexible production process and need only a minimum area – even an area of a desktop may be sufficient.

ACKNOWLEDGMENT

The scientific work was supported by the Company KABA Lower Austria, the government of Lower Austria and the EU FP 6 Project CA IPMMAN NMP2-CT2006-033205

REFERENCES

[1] Ch. Wögerer, A. Dedinak, W. Mann. 2007. Equipment based control system structures for complex and integrated systems intention and industrial application example, Universitad de Alicante, 23-25 May, Alicante (Spain).

[2] Dedinak, G. Kronreif, Ch Wögerer, "Vertical Integration of Production Systems" IEEE international Conference on "Industrial Technology ICIT'03", Maribor, Dezember 2003.

[3] Dedinak, Ch. Wögerer., H. Haslinger, P. Hadinger, "Vertical Integration of Mechatronic Systems demonstrated on Industrial Examples - Theory and Implementation Examples", BASYS'04, Proceedings of the 6th IFIP International Conference on Information Technology for balanced automation systems in Manufacturing and Services, Vienna, Austria, 27-29 September 2004.

[4] Dedinak, W. Studecker, A. Witt., "Fully automated testplant for calibration of flow-/heat-meters", International Federation of Automatic Control (IFAC), 16th World Congress, Juli 2005, Prag, Tschechische Republik.

[5] G. Strohrmann, "Automatisierungstechnik 1", Oldenburg, 1998.

[6] K.-H. John, M. Tiegelkamp, "SPS Programmierung mit IEC 61131-3", Springer, Berlin 2000.

[7] Ch. Wögerer, W. Mann, Georg Peschl, Development of flexible gripper for prescision assembly of cylinder locks, 2007 IEEE International Symposium on Assembly and Manufacturing (ISAM 2007), July 22-25, 2007, Ann Arbor, Michigan, USA.

[8] www.ipmman.eu – Homepage of the EU project IPMMAN.

ISSN 1590-8844
International Journal of Mechanics and Control, Vol. 10, No. 01, 2009

CALIBRATION AND TESTING ISSUES OF THE VISION, INERTIAL MEASUREMENT AND CONTROL SYSTEM OF AN AUTONOMOUS INDOOR QUADROTOR HELICOPTER

Laszlo Kis* Zoltan Prohaszka* Gergely Regula*

**Department of Control Engineering and Information Technology,*
Budapest University of Technology and Economics (BUTE) - Budapest, Hungary

ABSTRACT.

This article focuses on the practical problems emerged during the development of an indoor helicopter model, and both practical or theoretical solutions found to these. We present the details of development and implementation in the following areas: embedded software development in MATLAB/Simulink environment, marker based vision system for absolute positioning, inertial sensors for relative positioning, position and orientation estimation based on extended Kalman filters. Beside tests in real environment, we performed hardware-in-the-loop tests as well. The control system implementation and system tests are close to finish, all electronic components were realised and tested, but mainly on development-boards.

Keywords: indoor autonomous helicopter, quad-rotor, control system, implementation, vision

1. INTRODUCTION

1.1. THE PROJECT

Our project initiated in the spring of 2006 as a cooperation between Budapest University of Technology and Economics (BUTE) and MTA SZTAKI research institute. In the current phase, the primary goal of this research is to build an autonomous indoor quadrotor helicopter, which will serve later as a research testbed for advanced algorithms in the areas of control, path planning, manoeuvering in formation, position estimation, sensor fusion, embedded real-time (RT) vision system, spatial map building, robust and efficient mechanical and aerodynamical construction.

The development started in five areas: control system algorithms, system architecture, electronic components, mechanical and aerodynamical design and vision system.

In the end of 2007 we successfully performed hardware-in-the-loop tests, which verified that the onboard MPC555 CPU can be programmed via Simulink to perform the back-stepping control and extended Kalman filter algorithms together with CAN bus I/O in RT.

Contact author: Laszlo Kis, Zoltan Prohaszka, Gergely Regula
H-1117 Budapest, Magyar tudósok körútja 2
E-mail: { lkis, prohaszka, regula}@iit.bme.hu.

We successfully tested all system components, which were built on development boards. The first version of the helicopter body is under construction.

This article focuses mainly on implementation results, problems and solution related to the author's contribution to the project.

1.2. RELATED RESEARCH

Both ground and arial autonomous vehicles are intensively investigated nowadays. Currently, Unmanned Aerial Vehicle (UAV) technology is near to enter civilian applications, for example, there is an effort in the United Kingdom to tailor aviation regulations to suit for limited application of UAVs. There are lots of successful quadrotor UAV research projects in the world which demonstrated that current technology is capable of solving unmanned control of these vehicles.

A very brief list of such research would be: the STARMAC platform is a robust helicopter built in Stanford University, which serves as a testbed for multi agent control [6]. The X4-flyer was developed at the Australian National University, a pilot augmentation control is proposed in [9]. A miniature, partially autonomous quadrotor flyer was built at the Pennsylvania State University [2].

1.3. SYSTEM OVERVIEW

The control loop of the helicopter requires accurate position and orientation information. The primary sensor for this is an inertial measurement unit (IMU), which provides acceleration and angular velocity measurements. The raw

sensor output is loaded with noise and offset errors, which can build up increasing orientation and position error during integration. Since the measured acceleration vector has to be integrated according to the approximated orientation, the position contains third order integral of the angular velocity. Thus, for 6 degrees of freedom (DoF) mobile robots, one needs absolute measurements performed frequently. Our recent measurements are in correlation with our preliminary expectations, that there is a few second window, while integral error build up is small enough to work with (0.1m in 5 seconds). Based on these, one needs absolute position and orientation measurements roughly in every second or faster. For outdoor autonomous vehicles, GPS or differential GPS is usually used. For indoor vehicles, vision based measurements are widely used to compensate integration errors.
The overview of our system architecture is as follows. The helicopter will have an onboard CPU. The IMU and motor controllers are connected to the CPU via CAN bus. Also, a spread spectrum code division multiplexing (CDM) radio link is connected to the CPU, providing bidirectional communication between the rover and the ground station. The ground station sends commands and reference path to the CPU, together with the absolute position measurements. The helicopter sends status information to the ground. The ground station is connected to the computer performing vision algorithms via ethernet cable. We use commercial, high resolution web cameras for imaging.
The onboard computer is a phyCORE-MPC555, since it is lightweight, equipped with a floating point unit and can be programmed in MATLAB/Simulink. There is an alternative goal of the project is to compare high level model based programming of embedded systems with traditional methods.

2. CALIBRATION METHODS

During a general development process there are only a few points when calibrations can be done. Before final assembly we are able to do lots of measures for calibration. During this period we have a lot of time for measurements, so time-efficiency is not so important, but we need to perform these methods only once during the whole lifetime of the product. We are able to do additional calibrations during normal operation, but the number of measurements and processing time are limited.
These possibilities suit to the types of errors, if one can classify error sources as constant and varying errors. During the pre-build phase we are able to measure constant errors exactly and during normal operation we can estimate varying errors.
During the IMU and vision system calibration we used both calibration methods.

3. CALIBRATION OF THE IMU

We use a Crossbow μNAV100CA unit as an IMU. Unfortunately Crossbow decided to discontinue the production of this device. Because of indoor situation we utilise accelerometers and angular velocity sensors only.

3.1. TYPES OF ERRORS

Based on the sensor's datasheet we can classify the types of error sources. In connection with the accelerometers constant errors come from the fact that axes of sensors are not perpendicular and there is a gain error as well. There is also a bias error which depends on the supply voltage and the temperature. Therefore bias error can change considerably from take off to take off, but according to our measurements, it can be assumed constant during one flight.
Acceleration can cause different errors in different orientation in the angular velocity sensors. This phenomenon is due to the construction of the microelectromechanical system (MEMS) sensors. This error is permanent, but to reduce it we need exact information about the direction and magnitude of acceleration. Angular velocity sensors have also gain, non-perpendicularity and bias errors, classified similarly as in the case of accelerometers.
Our calibration method has two main parts. The first one is called offline calibration, it is used to decrease constant errors, the second one is the online calibration, used to remove variant errors.

3.2. OFFLINE CALIBRATION

This part of the calibration method is used to reduce permanent errors. Offline calibration estimates non-permanent errors as well, but online calibration will overwrite them. First part of the calibration is connecting to acceleration, because in the second part we will need calibrated acceleration for the calibration of angular velocity sensors.

3.2.1. ACCELERATION CALIBRATION.

The theory of the calibration is as follows. If there is no error in the measurements and gravity vectors measured in different orientation in stationary positions, vectors define a sphere in the origin with a radius of 1. Because of the errors this sphere is transformed to an ellipsoid with random centre and orientation. We should calculate the inverse transformation.
Let the ellipsoid be in the quadratic form of:

$$a_i Q_h a_i^T = 0 \tag{1}$$

Where Q_h is a 4×4 symmetric matrix with 10 free parameters and a_i is one of the measured gravity vectors in homogenous form. Transform the equation to the form of:

$$p^T a_{p_i} = 0 \tag{2}$$

Where p is a parameter vector with the 10 free parameters of Q_h and a_{p_i} is a vector with 10 elements, calculated from a measured gravity vector. An ellipsoid has 9 free parameters so we used the $p^T p = 1$ constraint. Let F be a matrix where the columns are the calculated a_{p_i} vectors from different measurements. At least 10 columns are needed. Divide F with the singular value decomposition (SVD) algorithm to the form of $F = UDV$, where D is a diagonal matrix. Find the column in U, which is connecting to the least element of D. This column will be the best p parameter vector.

Let Q_h be in the following form:

$$Q_h = \begin{bmatrix} M & v \\ v^T & c \end{bmatrix} \tag{3}$$

Where M is a 3×3 symmetric matrix, v is a 3×1 vector and c is a constant. Let the centre of the ellipsoid be s. Then

$$s = -M^{-1}v \tag{4}$$

Let N matrix be the transformation which transforms the ellipsoid in the origin to a sphere. N can be calculated by the $M = N^T N$ decomposition of M. We can do this decomposition by the calculation of the eigenvalues and eigenvectors of M in the form of $M = UDU^T$ ($U^T = U^{-1}$), where D is a diagonal matrix and the eigenvalues are in the diagonal of D and U has the eigenvectors in its columns. Let be D_1 is a diagonal matrix where the elements are the square roots of the elements of D. Then $N = D_1 U^T$.

The whole inverse transformation will be in the form of:

$$T = \begin{bmatrix} N & -Ns \\ 0^T & 1 \end{bmatrix} \tag{5}$$

T transforms the ellipsoid to a sphere in the origin with a radius of 1 and with random orientation. To define the orientation we measured two gravity vectors, the first defines the negative Z axis and the X axis is calculated from the second vector. These measurements give a rotation transformation called E.

The calibrated a_{cal} vectors can be determined from the measured ones in the form of:

$$a_{cal} = ETa_{measured} \tag{6}$$

3.2.2. ANGULAR VELOCITY CALIBRATION.

In stationary position the expected angular velocity is $0/s$. This results that all measured values are errors, therefore we cannot estimate the gain error from stationary measurements. We used the following error model:

$$\omega_{measured} = \omega_{real} + \omega_{bias} + (a_{cal}{}^T K)^T \tag{7}$$

Where ω_{bias} is the 3×1 bias error vector of the sensors, a is a 3×1 vector of the acceleration, measured together with angular velocity and K is a 3×3 matrix, which defines the coupling effect of the acceleration vector. Let the error be in the form as follows:

$$\omega_{bias} + (a_{cal}{}^T K)^T = (a_{cal\,h}{}^T R)^T = \left(\begin{bmatrix} a_{cal}{}^T & 1 \end{bmatrix} \begin{bmatrix} k_x & k_y & k_z \\ b_x & b_y & b_z \end{bmatrix} \right) \tag{8}$$

The columns of R can be calculated with the least square (LS) error method, based on the elements of ω. But it can be unified to the following form:

$$R = \left(A^T A\right)^{-1} A^T \Omega \tag{9}$$

Where Ω has at least 4 different angular velocity vectors in its rows and A has the acceleration vectors in its rows measured together with the corresponding angular velocities in the same time instants.

The calibrated ω_{cal} vectors can be determined from the measured ones in the form of:

$$\omega_{cal} = \omega_{measured} - \left(a_{cal}{}^T 1 R\right)^T \tag{10}$$

3.3. CALIBRATION BEFORE START-UP

Online calibration is a method to estimate bias error of the sensors. This algorithm should be fast and should be based only on one measurement. Therefore a constraint is introduced, that the helicopter should start from a horizontal orientation.

During the first second after the start we capture measurements from the sensors, than we calculate an average to reduce the effect of noise. Then the acceleration value is transformed with ET_1 matrix, where T_1 is the T transformation matrix with zeros at the place of translation. The bias error is the calculated acceleration vector subtracted from the $(0,0,-g)^T$ vector (where $g = 9.81 m/s^2$).

The average angular velocity is transformed with the K matrix and the calibrated acceleration vector. The remaining angular velocity will be the bias error.

During normal operation the acceleration and angular velocity is calculated as follows:

$$a_{cal} = ET_1 a_{measured} - a_{bias} \tag{11}$$

$$\omega_{cal} = \omega_{measured} - \omega_{bias} - a_{cal}^T K \tag{12}$$

3.4 RESULTS OF THE CALIBRATION

The effectiveness of calibration can be examined with the average values of acceleration and angular velocity in different orientations.

Before calibration the magnitude of the gravity were measured between 0.87g and 1.12g. The error of angular velocity were $\pm 1.5/s$.

We used 18 measurements for calibration, distributed equally in all directions. After the full calibration method the magnitude of the measured gravity were between 0.98g and 1.01g and the error of the angular velocity decreased $0.1/s$.

4. 3D VISION SYSTEM

4.1. REAL TIME OPERATION OF THE VISION SYSTEM

For the initial phase of the project we chose that the image processing algorithms would be evaluated on the ground, on one or more computers. This yields that the results of the image processing algorithms has to be sent to the onboard controller via radio link. A small bandwidth radio link is also required for control purposes, so the system design already had such a component.

We have chosen that we will use some marker based pre-processing solution. The question was whether the camera should be onboard and markers in the environment (ceiling) or in opposite setup. To avoid the need of transmitting images via radio, and due to requirements against markers, we use stationary cameras and helicopter mounted markers. In the preliminary phase, when the control algorithms will demonstrate capabilities of levitation and motion primitives, we will only use a single camera. The chosen image processing algorithm can be extended to multiple cameras and multiple processing stations to enhance features of the localisation. 7 to 11 markers will be mounted on the vehicle. These markers will be coloured to distinguish them or groups of them.

4.2. CALIBRATION, TRIFOCAL OPERATION

In our vision system we currently use a single camera and motion stereo technique to calculate relative motion of our camera to the helicopter body, which carries optical markers. However, our camera is stationary, but the markers are moving with rover. With elementary matrix operations we can calculate the movement of the markers, and thus the movement of the frame attached to the vehicle.

However, motion stereo technique and epipolar geometry involves the scaling ambiguity problem, which means that one can reconstruct the arrangement of cameras and objects only up to a scaling factor. If we inflate a model suitable to our measurements by any factor, we get a model which suits our measurements the same.

Once we got a suitable guess for the position of the markers and cameras from two images, we have to compare the size of the helicopter body to a previously known size to scale our model to be metric. Once we have done so, we can combine transformations to get the movement of the vehicle if we assume that the two images were shot from the same position.

Prior to take off, one needs two photographs (image #1 and #2) (It is advantageous to rotate the helicopter body by roughly 90 degrees around an arbitrary chosen axis) of the markers to calculate spatial arrangement of the markers, centroid of them and the 2^{nd} moment of their positions. (This would tell us the axis of symmetry). We can also measure the maximum distance of markers on the real vehicle. This maximum distance is fed into this calibration algorithm in metres, so we can inflate our model to be metric.

On the fly, the camera takes photograph of the markers (image #N). This image is fed into the 7 point motion stereo algorithm together with calibration image #1. A spatial arrangement of the markers and focal points is determined, but it is ambiguous up to a scale. We seek for the inflating factor f, which would result the same coordinates of markers in the frame of the camera of image #1, as the coordinates coming from calibration computation of image #1 and #2. Minimising spatial difference yields to a scalar LS problem for *f*.

Problems arise if image #N is taken from the same or similar position according to the helicopter frame as image #1. This means that the helicopter is in similar location as when image #1 was recorded, according to the frame of the single camera or world frame. In this case either the essential matrix can not be computed, or the markers reconstructed position will have large error in the direction of photographing rays. Even the resulting arrangement of markers may not be similar to the arrangement obtained during calibration at all.

To solve this problem, an other model is built based on image #2 and #N. This model is also inflated optimally. The resulting 3D error is compared to the error of the previous calculation. The smaller error selects, which calculation will be accepted.

Thus, in practice, we use 'trifocal' reconstruction with one, single camera.

4.3. DECOMPOSITION OF THE ESSENTIAL MATRIX

The 7 point algorithm returns 3 possible solutions of the fundamental matrix. Since we previously normalised the 2D measurements according to the camera's calibrated intrinsic parameters, the fundamental matrix is the same as the essential matrix. The essential matrix (E) contains information regarding relative camera motion only. In the following indices A and B represent relation to image #A and #B respectively.

$$E_{BA} = R_{BA}\left[t_A \times\right] \tag{13}$$

$$p_B^T E_{BA} p_A = 0 \tag{14}$$

$$E_{BA}^T = E_{AB} = R_{AB}[t_B \times]. \tag{15}$$

One can choose between these 3 solutions based on 2D or 3D reprojection error only, which means we have to build models of camera arrangement for each solution and verify how the measurements fit to these models. [3] and [4] recommend to calculate R (t can be obtained unambiguously as the null-space of E) by the following formulae:

$$UDV^T = E_{BA} \tag{16}$$

$$R = U\begin{bmatrix} 0 & \pm 1 & 0 \\ \mp 1 & 0 & 0 \\ 0 & 0 & 1 \end{bmatrix} V^T \tag{17}$$

$$t_A = \pm V[0,0,1]^T, t_B = \pm U[0,0,1]^T \tag{18}$$

if diag(D) is ascending.

These formulae lead to four solutions of R and t. For singular matrices SVD algorithm does not guarantee that the determinant of U and V will be positive, nor that they will be equal. The determinant of all resulting R will be $det(U \cdot V)$. The algorithm has to test the determinants and in the case of -1, it should correct it, for example by negating R. Each of the four solutions has to be investigated whether all points are in front of the camera.

The formulae above run precisely for synthetic (error-less) input, but on noisy input, the resultant R matrix is far from optimal. It is proved in [3], that it is optimal in the means of Frobenius norm. This means that using Frobenius norm is not optimal in practice. According to the terminology of [4], minimising Frobenius norm means minimising a chosen algebraic error function, which is not so good choice as using geometric error. Geometric error is well circumferenced, since it comes from the geometric arrangement rather than being chosen from many possible error representations. To achieve precise results on noisy output, we worked out an other algorithm to find better solutions of R.

We run the algorithm above on 9 markers with not very accurate blob centre detection. We got skew lines for rays reprojected from camera A and B, but it could clearly be seen, that these rays would be much closer if we had rotated one camera around t, the vector of translation. This gave the idea of our solution. After implementing it, the observed error disappeared.

4.3.1. FORMULATION OF OUR SOLUTION:

For errorless measurements, one of the three resulting essential matrices (all of them has a rank of 2) can be expressed as Eq. (13).

For real situations, E will be somewhat different. If we investigate epipolar geometry or the above equations, we see that t_A and t_B will be the right and left null vector of E_{BA}. The most robust way to find both of these vectors is a single SVD call on the essential matrix.

Now t_A is a vector in frame A which is parallel to the epipolar line which is the vector of translation of the focal point. Similarly, t_B is this spatial direction vector expressed in Frame B. We have not known yet, how frame B is located relative to frame A, but we know, that t_A and t_B is parallel to the same spatial line, to the epipolar line. We can rotate these frames to ensure

$$t_A = \pm R_{AB_1} t_B . \tag{19}$$

This could be done by calculating the axis of rotation by $t_R = t_A \times t_B$ and to calculate cosine and sine of the rotation angle we need $t_Q = t_A \times t_R$. We should use the Rodriguez formula to obtain R_{AB_1}. The resulting formulae would not be very different from the factorisation mentioned in [3] and [4]. Since we have already run SVD, and the factorisation solves this problem precisely, we should accept the resulting R as a transformation between frames A and B, which rotates t_A and t_B together perfectly, but we should treat the rotation around the epipolar axis as a good initial guess. We have to calculate how much rotation around the epipolar axis would rotate the corresponding epipolar planes together with minimal error. Since the axis of rotation is fixed, we have to determine the angle of rotation. Two possibilities arise.

The first assumes that two corresponding epipolar planes must coincide and must have the observed rays lie on the same side of the epipolar line (which is contained by any epipolar plane).

We implemented the second method, which assumes that only small correction has to be made to correct R_{AB_1}, and approximates as follows: $S_\alpha = \sin(\alpha) \approx \alpha$, $C_\alpha = \cos(\alpha) \approx 1$. The correct rotation can be calculated by the Rodriguez formula:

$$R_{AB_2} = Rot(t_A, C_\alpha, S_\alpha) R_{AB_1} = (I + 0 \cdot t_A t_A^T + \alpha [t_A \times]) R_{AB_1} \tag{20}$$

$$R_{BA_2} = R_{AB_2}^T \tag{21}$$

The rotation error can be calculated by the following form:

$$e_{total}^2 = \sum_i \left(P_{B_i}^T \left(R_{BA_2} [t_A \times] \right) P_{A_i} \right) \tag{22}$$

which is the quadratic form of α.

$$e_{total}^2 = A\alpha^2 + 2b\alpha + c \tag{23}$$

where the optimal α is:

$$\alpha_{opt} = -A^{-1} b \tag{24}$$

If we correct R_{AB_1} with the determined rotation about the epipolar axis, the resulting 3 dimensional reprojection error will be much less than it was previously.

We have to highlight, that our algoritm relies on the calculated essential matrix and measured point correspondences, while the standard method in [3] and [4] is based only on the essential matrix. This can be thought as a reason, why the new algorithm can perform better on noisy measurements.

4.4. DELAY

In RT vision systems it is important to tell the exact time the pictures were taken synchronised to the clock of other system components.

Most hardware is unable to tell the exact time of the start and end of the exposition, neither for each separate pixel (or line), nor for an average, but precise time for the whole picture. The whole image is not recorded in the same time instance by usual video input devices.

While the image arrives to the processing process's address space (by a callback function) it has gone through a lot of buffers and delays, so time stamping images based on time of arrival is not an accurate choice. The results of the vision system can suffer additional delay while arriving to the control system (in our set-up: via radio link), which increases the problem if the vision system does not have a

clock synchronised to the control system's clock.
We expect this delay to be somewhere between 1.5 … 3 frames, which means around 60 to 120ms. Since we found a satisfying solution to get around this problem, we did not simulate this effect in our hardware-in-the-loop setup, so we are unable to tell how the magnitude of the delay affects closed loop behaviour.
To solve this problem, we modulate our marker's intensity with a periodic signal. The period is chosen to be twice as much as previously measured or approximated delay time. The vision system calculates average light intensity, and sends these data to the control system (rover) which is responsible for the modulation, so knows the exact timing of it. Removing low-frequency components from this signal, we can calculate exact delay time by observing phase shift.

5. REAL TIME OPERATION OF THE SYSTEM

5.1 HELICOPTER DYNAMIC MODEL AND CONTROL ALGORITHM

Multicomponent dynamic systems can be described using frames. Let us assume that the vision system's frame and the helicopter's frame K_H at the start position are identical to the world base frame (K_B). The position and orientation of the helicopter can be described by a homogeneous transformation, whose orientation and position parts are $A(\eta)$ and ξ, respectively. The vector η denotes the Euler angles (Roll-Pitch-Yaw angles), i.e. $\eta = (\Phi, \Theta, \Psi)^T$, while $\xi = (x, y, z)^T$.
The angular velocity (ω) takes the form $\omega = \Gamma \dot{\eta}$ and its derivative $\dot{\omega} = \Gamma \ddot{\eta} + \dot{\Gamma} \dot{\eta}$ where

$$\Gamma = \begin{bmatrix} 1 & 0 & -S_\Theta \\ 0 & C_\Phi & S_\Phi C_\Theta \\ 0 & -S_\Phi & C_\Phi C_\Theta \end{bmatrix} \tag{25}$$

The helicopter has four actuators, four brushless DC (BLDC) motors which exert a lift force dependent on the angular velocities ($f_i = b\Omega_i^2$). The BLDC motors' reference signals can be programmed in Ω_i [8]. The resulting torque and lift force are

$$\tau = \begin{pmatrix} lb(\Omega_4^2 - \Omega_2^2) \\ lb(\Omega_3^2 - \Omega_1^2) \\ d(\Omega_2^2 + \Omega_4^2 - \Omega_1^2 - \Omega_3^2) \end{pmatrix} \tag{26}$$

$$u = f_1 + f_2 + f_3 + f_4 = b\sum_{i=1}^{4}\Omega_i^2 \tag{27}$$

where l, b, d are helicopter and rotor constants. The gyroscopic effect can be modelled as

$$\tau_G = -I_r(\omega \times k)(\Omega_2 + \Omega_4 - \Omega_1 - \Omega_3) = -I_r(\omega \times k)\Omega \tag{28}$$

where I_r is the rotor inertia and k is the third unit vector. The equations of motion of the helicopter are

$$m\ddot{\xi} = A(\eta)F_{ext} + F_g \tag{29}$$

$$\tau_{ext} = I\dot{\omega} + \omega \times (I\omega) \tag{30}$$

where I is the inertia matrix of the helicopter, τ_{ext} and F_{ext} are the external torque and force in K_H and F_g is the gravity vector in K_W. We assumed that I is diagonal, because of the symmetry of the helicopter. $\Gamma \approx I_3$ (where I_3 is the unit matrix), because during flight Φ, Θ are around 0. The equations of motion can be rewritten in a simplified form:

$$\ddot{x} = (C_\Phi S_\Theta C_\Psi + S_\Phi S_\Psi)\frac{u}{m} \tag{31}$$

$$\ddot{y} = (C_\Phi S_\Theta S_\Psi - S_\Phi C_\Psi)\frac{u}{m} \tag{32}$$

$$\ddot{z} = -g + C_\Phi C_\Theta \frac{u}{m} \tag{33}$$

$$\ddot{\Phi} = \frac{I_y - I_z}{I_x}\dot{\Theta}\dot{\Psi} - \frac{I_r}{I_x}\dot{\Theta}\Omega + \frac{1}{I_x}\tau_x \tag{34}$$

$$\ddot{\Theta} = \frac{I_z - I_x}{I_y}\dot{\Phi}\dot{\Psi} + \frac{I_r}{I_y}\dot{\Phi}\Omega + \frac{1}{I_y}\tau_y \tag{35}$$

$$\ddot{\Psi} = \frac{I_x - I_y}{I_z}\dot{\Phi}\dot{\Theta} + \frac{1}{I_z}\tau_z \tag{36}$$

The state equations can easily be obtained by choosing $(x, y, z, \dot{x}, \dot{y}, \dot{z}, \Phi, \Theta, \Psi, \dot{\Phi}, \dot{\Theta}, \dot{\Psi})^T$ as state variables.
In order to perform simulations in the early stages of the project, the mechanical parameters of the helicopter was needed. Based on the planned dimensions of the vehicle, the masses of purchased elements and an other quadrotor construction [7], we estimated a set of the required parameters. These parameters are summarised in Table I.

Table I: The parameters of the helicopter used prior to construction

Parameter	*Value*
l	0.16
b	8.44310-6
d	8.44310-8
I_x, I_y	3.91710-3
I_z	6.89710-3
I_r	1.66710-5
m	0.89

The control law is based on the backstepping algorithm described in detail in [1]. Since the vision system's operating frequency is not high enough and the control

ISSN 1590-8844
International Journal of Mechanics and Control, Vol. 10, No. 01, 2009

algorithm requires signals that are not measured by the IMU, nor by the vision system, a state estimator has been included in the control. The state estimator consists of two extended Kalman filters (EKFs), one estimates the orientation and the angular velocity, the other the position and the velocity of the helicopter.
Let us collect the angular velocity components measured by the IMU in the vector $\rho_S \in K_S$ (which also contains the unknown bias and a Gaussian noise beside the correct value $\rho_{S,0}$) and transform them into the helicopter frame K_H:

$$\rho_S = \rho_{S,0} + \rho_{S,b} + \rho_{S,n} \tag{37}$$

$$A_s\rho_S = A_S\rho_{S,0} + A_S\rho_{S,b} + A_S\rho_{S,n} \tag{38}$$

$$\rho = A_S\rho_{S,0} = A_S\rho_S - A_S\rho_{S,b} + A_S\rho_{S,n} \tag{39}$$

The derivative of the Euler angles can be determined from $\rho = (P,Q,R)^T$ by using

$$\Gamma^{-1} = \begin{bmatrix} 1 & T_\Theta S_\Phi & T_\Theta C_\Phi \\ 0 & C_\Phi & -S_\Phi \\ 0 & S_\Phi/C_\Theta & C_\Phi/C_\Theta \end{bmatrix} \tag{40}$$

$$\begin{pmatrix} \dot{\Phi} \\ \dot{\Theta} \\ \dot{\Psi} \end{pmatrix} = \Gamma^{-1}\rho \tag{41}$$

$$\dot{\rho}_{s,b} = \rho_{s,b,n} \tag{42}$$

$$\begin{pmatrix} \Phi \\ \Theta \\ \Psi \end{pmatrix}_m = \begin{pmatrix} \Phi \\ \Theta \\ \Psi \end{pmatrix} + \begin{pmatrix} \Phi \\ \Theta \\ \Psi \end{pmatrix}_n \tag{43}$$

The continuous time model above can be discretised by the Euler approximation if T denotes the sample time:

$$x_1 = (\Phi,\Theta,\Psi)^T \;\; x_2 = \rho_{S,b} \;\; x = \left(x_1^T, x_2^T\right)^T \tag{44}$$

$$w_1 = \rho_{S,n} \;\; w_2 = \rho_{S,b,n} \;\; w = \left(w_1^T, w_2^T\right)^T \tag{45}$$

$$u = \rho_S \tag{46}$$

$$x_{1,k+1} = x_{1,k} - T\Gamma_k^{-1}A_S x_{2,k} + T\Gamma_k^{-1}A_S u_k + T\Gamma_k^{-1}A_S w_{1,k} \tag{47}$$

$$x_{2,k+1} = x_{2,k} + Tw_{2,k} \tag{48}$$

$$y_k = x_{1,k} + z_k \tag{49}$$

The EKF algorithm can be performed then, assuming w and z are not correlated and introducing the following notations:

$$R_{w,k} = E[w_k w_k^T] \tag{50}$$

$$R_{z,k} = E[z_k z_k^T] \tag{51}$$

$$A_k = \frac{\partial f(\hat{x}_k, u_k, 0)}{\partial x} \tag{52}$$

$$B_{w,k} = \frac{\partial f(\hat{x}_k, u_k, 0)}{\partial w} \tag{53}$$

$$C_k = \frac{\partial g(\hat{x}_k, 0)}{\partial x} \tag{54}$$

$$C_{z,k} = \frac{\partial g(\hat{x}_k, 0)}{\partial z} \tag{55}$$

Prediction:

$$\bar{x}_k = f(\hat{x}_{k-1}, u_{k-1}, 0) \tag{56}$$

$$M_k = A_{k-1}\Sigma_{k-1}A_{k-1}^T + B_{v,k-1}R_{v,k-1}B_{v,k-1}^T \tag{57}$$

Time update:

$$S_k = C_k M_k C_k^T + C_{z,k}R_{z,k}C_{z,k}^T \tag{58}$$

$$G_k = M_k C_k^T S_k^{-1} \tag{59}$$

$$\hat{x}_k = \bar{x}_k + G_k(y_k - g(\bar{x}_k, 0)) \tag{60}$$

$$\Sigma_k = M_k - G_k S_k G_k^T \tag{61}$$

The estimation of the position and the velocity of the helicopter is performed similarly.
To extend the controller's capabilities, a path tracking algorithm is also included. Thus, the helicopter is capable of following a path defined by its waypoints' spatial coordinates and yaw angles. The helicopter may advance towards the next navigation point if it reaches the actual one within a predefined distance.

5.2. HARDWARE AND SOFTWARE ENVIRONMENT

The full system is shown in Figure 1.

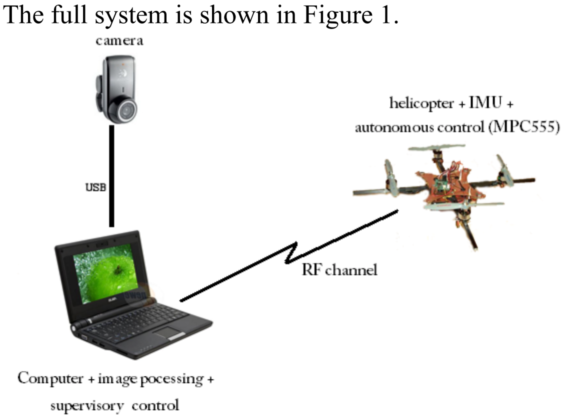

a,

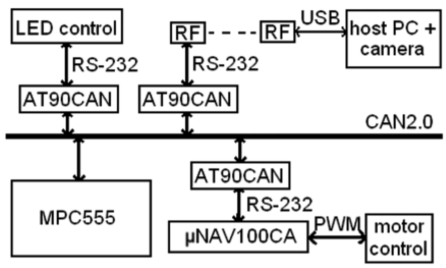

b,

Figure 1 The full system (a: physical layout b: hardware schematic)

The four BLDC motors are controlled by pulse width modulation (PWM) motor controllers. PWM signals are generated by the Crossbow μNAV100CA unit. This is used as IMU as well. Main communication runs over CAN bus. To connect units which do not have CAN interface, AT90CAN128 microcontrollers are used to transmit data to CAN bus. These controllers are programmed in C, with AVR Studio and WinAVR.

The video processing algorithm runs on a host PC and programmed in MATLAB/Simulink environment with Image Acquisition Toolbox and Image Processing Toolbox. An other program, written in C, runs parallel and communicate with the video processing algorithm. This program provides a user interface and handles the serial interface of the PC. Data are sent to the helicopter via radio channel.

A LED control unit is also part of the helicopter to find the proper colors of markers for video processing. The central unit is a Freescale MPC555 microcontroller programmed in MATLAB/Simulink environment with Real-Time Workshop, Real-Time Workshop Embedded Coder and Embedded Target For Motorola MPC555. Programs are compiled with MetroWerks CodeWarrior cross-development tool.

5.3. EMERGING PROBLEMS DURING DEVELOPMENT

5.3.1. Communication

MATLAB's Target Language Compiler supports the majority of Simulink's blocks, while the Embedded Target for Motorola MPC555 includes blocks that can be used for communication via serial and CAN interface. However experiments show, that serial communication causes a significant delay (20ms-30ms) in the signal propagation. Since CAN communication did not cause such delays, the issue was tackled by adding an extra component to the system which was responsible for converting the data received from the serial interface into CAN packets.

It is also crucial to maintain data integrity during the hardware-in-the-loop test, since starting the calculation of the control inputs before receiving all measurement data may make the control loop unstable. Therefore, all data sent by the emulated helicopter model are timestamped. The MPC555 contains 16 buffers that can be used for transmitting or receiving CAN packets, while the number of data to be transmitted in each cycle may exceed the buffers' number. Since the packet size is limited to 8 bytes, groups of the measurement data need to be transmitted in each packet. Data acquisition (collecting data from the buffers) on the target processor is performed at a higher frequency compared to that of the control algorithm, to ensure that the delay between receiving the measurement and starting the calculation of the new control inputs is minimal.

5.3.2. The sample time of the control algorithm

Preliminary calculations showed that theoretically the MPC555 is capable of performing the computation of the control inputs every 0.01s. However, Execution Profiling shows that calculating the control inputs using double precision floating point numbers takes slightly more than 20ms. Using single precision numbers does not cause significant deterioration in the calculations, however, it saves 5ms.

5.3.3. Software issues

The compilation procedure requires special attention from the developer. If the Simulink model to be run on the dSPACE DS1103 board contains several S-functions written in C that contain global variables inside, then these variables should have different names in order to avoid unexpected behaviour during execution.

Sampling times are also of high importance, especially when there are blocks in the same model whose sampling times are different from each other. It is not a good practise to set the sampling time property “inherited” of any Simulink block. For the same reason the usage of blocks that do not have sampling time property (like discrete derivative blocks) is not recommended.

5.4. REAL-TIME TESTS

Real-time tests were performed using the hardware-in-the-loop method. The tests were aided by a dSPACE DS1103 board. First the model of the helicopter, the sensory and the vision systems' measurements were emulated on the board, while further experiments included the real IMU and vision system. The basic scheme of the tests can be seen in Figure 2.

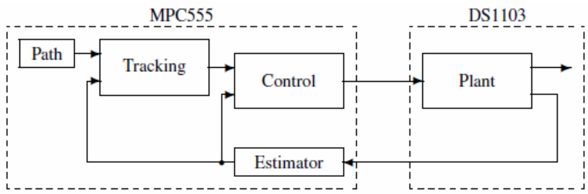

Figure 2 The scheme of the distributed control

As an illustration of the control algorithm's capabilities, two complex manoeuvres are presented. One is of a spatial spiral and the other is of an equilateral pentagon shape. In the diagrams of Figure 3. crosses show the navigation points, while lines show the helicopter's actual movement.

5.5. STATE ESTIMATION WITH REAL-TIME IMU AND VISION

After the hardware-in-the-loop test we changed the sources of information from simulated ones to real ones. In the first step the IMU unit was connected and the estimated position and orientation were feedbacked as the information from vision system. This test simulated the situation when the vision system cannot produce data (e.g. because of coverage).

The result of the test is shown in Figure 4. The error reaches 10cm after 6 seconds. This means that the helicopter cannot fly more than 5 or 6 seconds without information from the vision system.

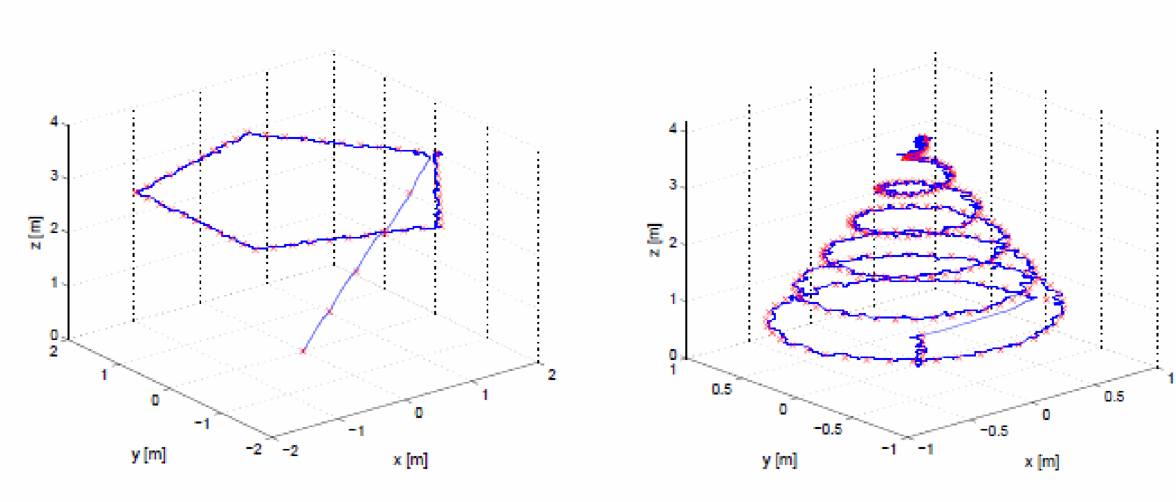

Figure 3 Complex predefined trajectories

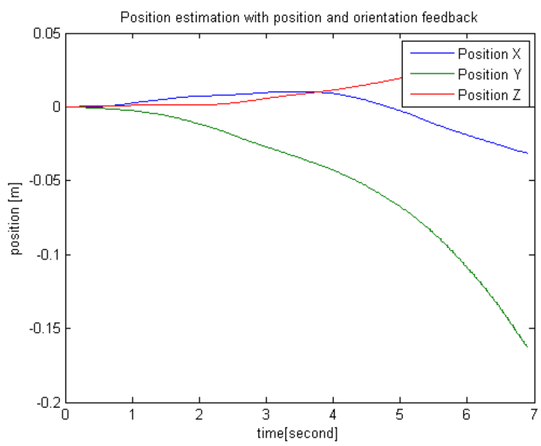

Figure 4 Estimated position with feedback

The next step was that we connected the vision system to the state estimation. The orientation estimation around the Z axis is shown in Figure 5. The estimation error except fast transitions was between ± 1.5.
The position estimation is shown in Figure 6. The error of position estimation was between ± 6 cm, except fast transitions.
The results of the tests show that the estimation is precise enough to expect that the control algorithm will be able to drive the helicopter accurately.

6. CONCLUSION

In this paper we presented the implementation results of the development of a quadrotor indoor helicopter. We focused on accurate position and orientation sensing, as this is the key for precise manoeuvering. Details of the calibration of the Inertial Measurement Unit was shown. We presented the operation of our marker based vision system which serves absolute position sensing. Solution to an previously undescribed problem regarding the decomposition of the essential matrix was formulated. The fusion of absolute and relative position sensing was shown by the operation of extended Kalman filters. The system's architecture was described both for the hardware-in-the-loop tests and for normal operation.

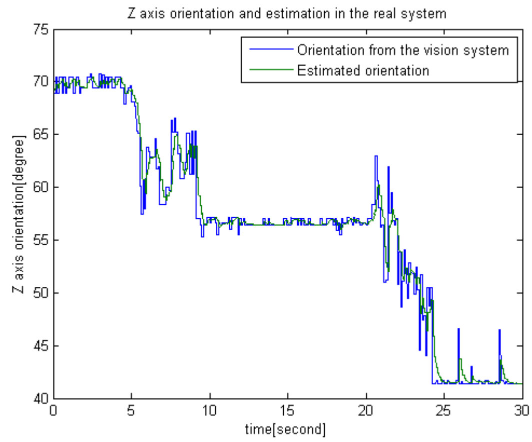

Figure 5 Estimated orientation around Z axis

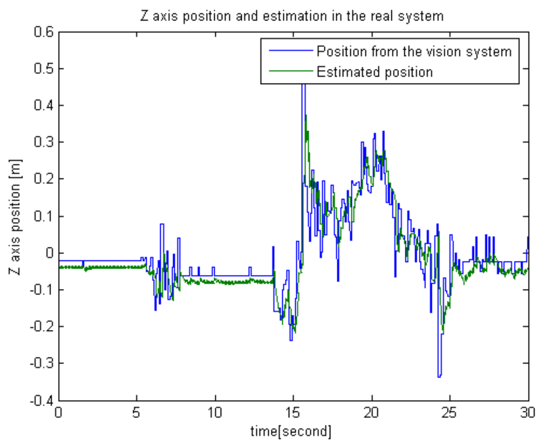

Figure 6 Estimated position on Z axis

6.1 FUTURE WORK

For the first liftoff, when the controller board remains on the ground, the vehicle carries only motor drives and IMU and they are connected to the ground components via the guiding cable, we need the following steps:

First we should finish mechanical work, then a safety cable should be attached to the helicopter, which will hang from the ceiling during the first flights. Elongate cables should connect the IMU, motor drivers and the CPU. Finally we should determine the position of the centroid, rotor axes, IMU and optical markers in the vehicle coordinate frame.

For the first true flight, we need the following: after successfully performing the previous steps, we should prevent mechanical noise coming from the motors reaching the IMU by applying mechanical filters with precisely tailored frequency response tuned by the parameters of elastic springs and damper elements. Finally we should design, build, test and correct the onboard printed circuit board, which packs together the CPU and other microcontrollers to achieve a small, light and compact unit.

ACKNOWLEDGEMENT

This research was supported by the Hungarian National Research Program under grant No. OTKA K 71762.

REFERENCES

[1] Bouabdallah S., Siegwart R., Backstepping and Sliding-mode Techniques Applied to an Indoor Micro Quadrotor *IEEE International Conference on Robotics and Automation, Barcelona, Spain,* 2005.

[2] Hanford S. D., Long L. N., Horn J. F., A Small Semi-Autonomous Rotary-Wing Unmanned Air Vehicle (UAV) *American Institute of Aeronautics and Astronautics, Infotech@Aerospace Conference, Paper No. 2005-7077,* 2005

[3] Hartley R. I., An Investigation of the Essential Matrix, *GE CRD, Schenectady, NY 12301, USA, Tech. Rep.,* 1993.

[4] Hartley R. I., Zissermann A., Multiple View Geometry in Computer Vision, *Cambridge University Press 2003, pp. 25-127. ISBN 0521 54051 8*

[5] Hartley R. I., Kahl F., Global Optimization through Searching Rotation Space and Optimal Estimation of the Essential Matrix *International Conference on Computer Vision, Rio de Janeiro,* 2007.

[6] Hoffmann G. , Rajnarayan D. G., Waslander S. L., Dostal D., Jang J. S., Tomlin C. J., The Stanford Testbed of Autonomous Rotorcraft for Multi Agent Control (Starmac) *Digital Avionics Systems Conference* 2004.

[7] Kendoul F., Lara D., Fantoni I., Lozano R., Nonlinear Contor for systems with bounded inputs: Real-time embedded control applied to UAVs *45th IEEE Conference on Decision and Contro,* 2006.

[8] Molnar Cs., Sensorless steering and revolution control of BLDC motor driving a quadrotor helicopter *BUTE master thesis* 2007.

[9] Pounds P., Mahony R., Hynes P., Roberts J., Design of a Four-Rotor Aerial Robot *Australasian Conference on Robotics and Automation* 2002.

ISSN 1590-8844
International Journal of Mechanics and Control, Vol. 10, No. 01, 2009

FRACTIONAL-ORDER DERIVATIVES AND THEIR APPLICATION TO THE POSITION CONTROL OF ROBOTS

Luca Bruzzone Giorgio Bozzini

Dipartimento di Meccanica e Costruzione delle Macchine, Università degli Studi di Genova

ABSTRACT

The paper discusses the application of fractional calculus to robotics; in particular, the $PDD^{1/2}$ position control scheme is proposed. This control scheme is an evolution of the PD control, characterized by a third gain which multiplies the half-derivative of the error. The introduction of this gain allows to lower considerably the settling time of a second-order linear system in comparison with a traditional PD control, under the same limitations of maximum control output and overshoot. The behaviour of a 2R robot with a $PDD^{1/2}$ position control has been simulated, and the results show that this scheme is a simple but interesting option for position control of robots and mechatronic devices.

Keywords: fractional calculus, tracking control, $PDD^{1/2}$ control

1 INTRODUCTION

Fractional calculus deals with the derivatives and integrals to an arbitrary order, which is not necessarily integer, but can be rational, irrational or even complex [1-3]. Therefore, fractional calculus (*FC*) can be considered a possible extension of classical mathematics.

Mathematicians such as Euler and Liouville investigated this theoretical problem since the birth of the differential and integral calculus, but the application of fractional derivatives and integrals (*FDIs*) to practical problems is relatively recent.

The theory of FDIs is a useful tool in many scientific areas such as physics [4], biology [5], electronics [6], signal processing [7].

The application of the FDIs theory to control system design is studied in [8-10]. In particular, a $PI^{\lambda}D^{\mu}$ controller with fractional order derivatives and integrals is discussed in [11].

Within the field of robotics, in [12] a fractional order algorithm is applied to the position/force control of a 2R robot; in [13] a fractional order PD^{α} control is applied to the locomotion of a multi-legged robot.

Contact author: Luca Bruzzone[1], Giorgio Bozzini[1]

[1]Dipartimento di Meccanica e Costruzione delle Macchine, Università degli Studi di Genova, Via Opera Pia 15A, 16145 Genova, Italy, {bruzzone, bozzini}@dimec.unige.it

In the proposed work, the application of the fractional calculus to robot control system design is faced with a different approach, not substituting a differential-order derivative term for the first-order derivative term, but using them in combination. In particular, the half-derivative term is added to the PD scheme, giving rise to the $PDD^{1/2}$ scheme.

The justification of this approach is due to the belief that the robot manufacturers are unlikely to abandon completely the well-known and reliable PID scheme, but maybe they will accept to add the half-derivative term if significant advantages are demonstrated.

In the following of the paper the integral term, which reduces the steady-state error, is not considered and the attention is focussed on the comparison between the PD scheme and the $PDD^{1/2}$ scheme; obviously, the results can be easily extended to the $PIDD^{1/2}$ scheme.

2 THEORETICAL DEFINITION OF THE FRACTIONAL DERIVATIVE

Since the foundation of fractional calculus, different approaches for the generalization of derivatives and integrals to a non-integer order α have been followed, and this leads to different theoretical definitions of FDIs.

In [14] these definitions are compared with special reference to the application to control algorithms, and the Letnikov definition of fractional order derivative has some computational advantages in the discrete-time implementation.

The Letnikov definition for the derivative of fractional order α of a signal $x(t)$ is the following:

$$D^{\alpha}x(t)=\lim_{h\to 0}\left[\frac{1}{h^{\alpha}}\sum_{k=0}^{\infty}(-1)^{k}\frac{\Gamma(\alpha+1)}{\Gamma(k+1)\Gamma(\alpha-k+1)}x(t-kh)\right] \tag{1}$$

where Γ is the gamma function and h is the time increment. This formulation leads to a discrete-time approximation which can be expressed in the z-domain by the following equation [14]:

$$D^{\alpha}\left(z^{-1}\right)=\frac{1}{T^{\alpha}}\sum_{k=0}^{\infty}(-1)^{k}\frac{\Gamma(\alpha+1)}{k!\Gamma(\alpha-k+1)}z^{-k} \tag{2}$$

where T is the sampling period.

This approximation requires an infinite number of terms; a real discrete-time implementation can be obtained using a finite number of terms; the accuracy of the sixth-order truncation can be considered acceptable, as pointed out in [14].

The derivative of fractional order α = ½ is called *half-derivative*; its sixth-order approximation is expressed in the z-domain by the following transfer function:

$$D^{1/2}\left(z^{-1}\right)=\sqrt{\frac{1}{T}}\left(1-\frac{1}{2}z^{-1}-\frac{1}{8}z^{-2}-\frac{1}{16}z^{-3}-\frac{5}{128}z^{-4}+\right.$$
$$\left.-\frac{7}{256}z^{-5}-\frac{21}{1024}z^{-6}\right) \tag{3}$$

3. THE PDD$^{1/2}$ DISCRETE-TIME CONTROL SCHEME

The scheme of the PDD$^{1/2}$ discrete-time control system can be easily obtained starting from the previously defined z-transform of the half-derivative.

Figure 1 shows the PDD$^{1/2}$ control loop applied to a purely inertial second-order system, which is represented in continuous time by the following Laplace transfer function:

$$\frac{\theta(s)}{\tau(s)}=\frac{1}{Js^{2}} \tag{4}$$

where θ is the angular position, τ is the torque and J is the mass moment of inertia.

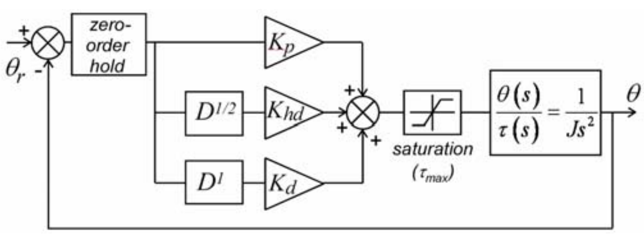

Figure 1 PDD$^{1/2}$ control applied to a purely inertial system.

The digital control is in discrete time, so the error $e = \theta_r - \theta$ is processed by a zero-order hold with sampling time T; then the discrete-time error is multiplied by the proportional gain K_p; the derivative of the error is obtained from the discrete-time error by the following z-transfer function:

$$D^{1}\left(z^{-1}\right)=\frac{1-z^{-1}}{T} \tag{5}$$

and then multiplied by K_d; the half-derivative is obtained by the z-transfer function (3) and then multiplied by K_{hd}; the proportional, derivative and half-derivative terms are added up; the maximum absolute value of control output is limited by a saturation function.

The PD control (K_{hd} = 0) has been compared to different PDD$^{1/2}$ controls under the following assumptions:

- the proportional gain K_p of both the PD and the PDD$^{1/2}$ controls is defined as function of the desired natural angular frequency ω_n:

$$K_p = J\omega_n^2 \tag{6}$$

- the output saturation value (τ_{max}) of both the PD and PDD$^{1/2}$ controls is defined by the maximum angular acceleration α_{max}:

$$\tau_{\max} = J\alpha_{\max} \tag{7}$$

- once selected the value of K_{hd} (null for the PD control) the derivative gain K_d is determined choosing its minimum value that provides a stabilization without overshoot in presence of a step of θ_r from zero to θ_{max}

For the comparison between the PD and PDD$^{1/2}$ control systems, the following parameters are used:

- ω_n = 5 rad/s
- J = 7.575 kgm^2
- α_{max} = 2π rad/s^2
- T = 0.01 s
- θ_{max} = 1 rad

Five different values for the K_{hd} gain are compared: 0 (PD), 20, 50, 100, 200 Nms$^{1/2}$/rad. As already said, the corresponding values of derivative gain K_d are the minimum values that provide stabilization without overshoot. The resulting five gain sets are shown in Table I.

Table I shows two nondimensional coefficients (ξ and γ) related to the gains K_d and K_{hd}. The damping ratio ξ represents the magnitude of the derivative gain, considering the proportional effect as a spring and the derivative effect as a damper:

$$\xi=\frac{K_d}{2\sqrt{JK_p}} \tag{8}$$

The second nondimensional coefficient represents the magnitude of the half-derivative gain:

$$\gamma=\frac{K_{hd}}{K_p^{3/4}J^{1/4}} \tag{9}$$

Table I - The gain sets used for the comparison between the PD and the PDD$^{1/2}$ controls

Gain Set	K_p (Nm/rad)	K_{hd} (Nms$^{1/2}$/rad)	K_d (Nms/rad)	ξ	γ
a (PD)	189.38	0.00	72.34	0.96	0
b (PDD$^{1/2}$)	189.38	20.00	77.26	1.02	0.24
c (PDD$^{1/2}$)	189.38	50.00	83.33	1.10	0.59
d (PDD$^{1/2}$)	189.38	100.00	90.90	1.20	1.18
e (PDD$^{1/2}$)	189.38	200.00	113.25	1.49	2.36

Figures 2 and 3 show the time histories of θ and τ in the five cases; it is possible to note that the settling time decreases by increasing half-derivative gain; this is due to the fact that with high half-derivative gains the control output τ tends to be similar to the one of a bang-bang control (maximum positive torque for the acceleration and maximum negative torque for the deceleration), and the bang-bang control is the one that minimizes the settling time of a second-order linear system for a given maximum control output.

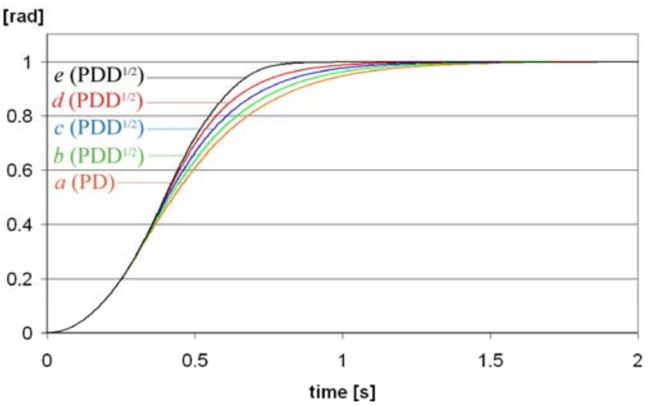

Figure 2 PD-PDD$^{1/2}$ comparison: time histories of θ.

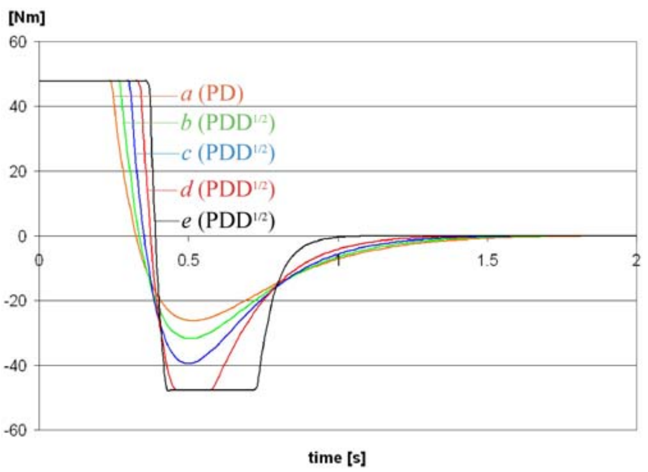

Figure 3 PD-PDD$^{1/2}$ comparison: time histories of τ.

In Figure 3 it is possible to note that with the gain set *e* the torque changes rapidly from $+\tau_{max}$ to $-\tau_{max}$; the control behaviour is very close to the one of a bang-bang control; moreover, the increase of half-derivative gain is coupled with the increase of derivative gain, and the damping ratio of the gain set *e* is high ($\xi = 1.49$); for all of these reasons, it is not convenient to increase further the half-derivative and derivative gains.

The settling times to within 2% associated with the different gain sets are summarized in Table II; it is possible to note that the adoption of the PDD$^{1/2}$ control algorithm allows to lower remarkably the settling time (up to about –39%) using the same maximum torque.

Table II - Settling time comparison between the PD and the PDD$^{1/2}$ controls

Gain Set	*Settling Time* (s)	*Variation*
a (PD)	1.209	0 %
b (PDD$^{1/2}$)	1.115	-7.78 %
c (PDD$^{1/2}$)	1.023	-15.38 %
d (PDD$^{1/2}$)	0.918	-24.07 %
e (PDD$^{1/2}$)	0.74	-38.79 %

Let us note that the system is linear, consequently the gains of systems with different inertia and angular frequency can be tuned similarly imposing the same values for the nondimensional coefficients ξ and γ; therefore the previous results are general and not restricted to the considered set of parameters.

4. PDD$^{1/2}$ CONTROL OF A 2R ROBOT

The PDD$^{1/2}$ control is now applied to the position control of a 2R robot. The scheme of this simple robotic architecture is shown in Figure 4.

The dynamic model of a 2R robot without friction is expressed by the following equation [15]:

$$\boldsymbol{\tau} = \mathbf{H}(\mathbf{q})\ddot{\mathbf{q}} + \mathbf{C}(\mathbf{q},\dot{\mathbf{q}}) + \mathbf{G}(\mathbf{q}) - \mathbf{J}^T(\mathbf{q})\mathbf{F} \tag{10}$$

where $\boldsymbol{\tau} = [\tau_1, \tau_2]^T$ is the vector of the actuator torques, $\mathbf{q} = [q_1, q_2]^T$ is the vector of the internal coordinates, $\mathbf{H}(\mathbf{q})$ is the inertia matrix, $\mathbf{C}(\mathbf{q},\dot{\mathbf{q}})$ is the vector of the centrifugal and Coriolis terms, $\mathbf{G}(\mathbf{q})$ is the vector of the gravity terms, $\mathbf{J}(\mathbf{q})$ is the Jacobian matrix and $\mathbf{F}$ is the force that the environment applies to the end-effector.

Figure 5 shows the scheme of the considered control layout. The output of the trajectory planning is the vector of the reference external coordinates $\mathbf{x}_r = [x_r, y_r]^T$, the reference internal coordinate vector $\mathbf{q}_r = [q_{1r}, q_{2r}]^T$ is obtained by means of the inverse kinematics equations.

ISSN 1590-8844
International Journal of Mechanics and Control, Vol. 10, No. 01, 2009

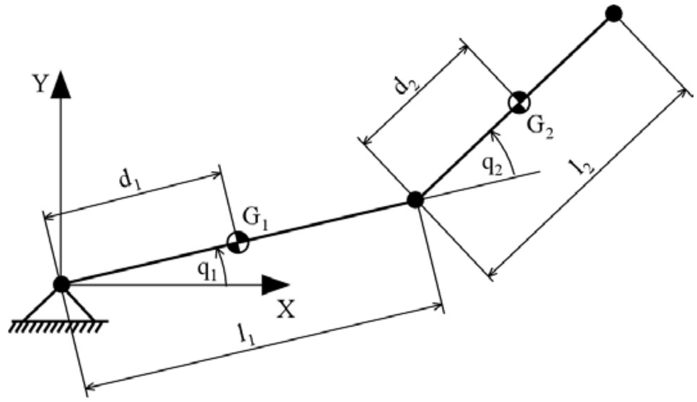

Figure 4 Scheme of the 2R robot.

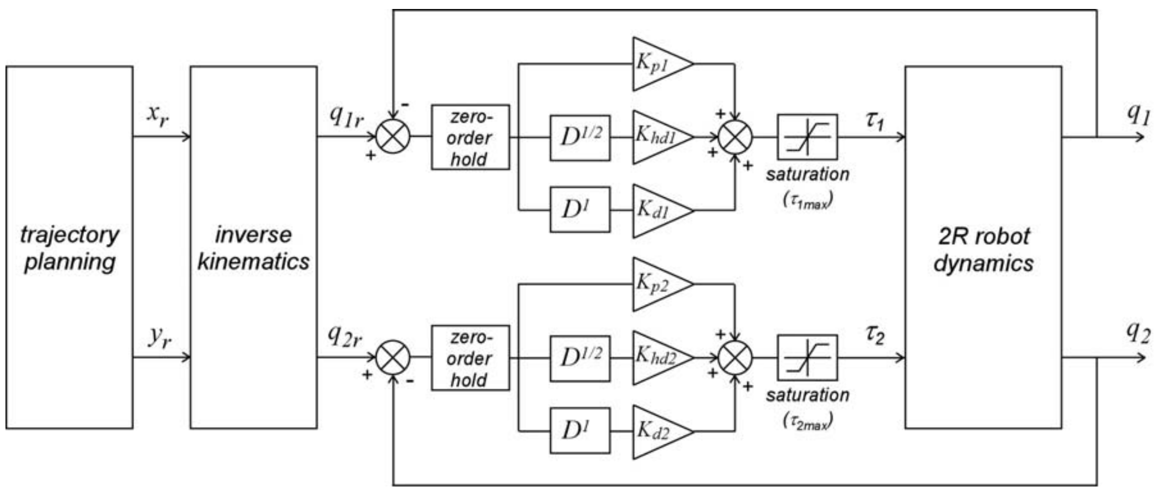

Figure 5 PDD$^{1/2}$ position control scheme of the 2R robot.

Table III - Simulation parameters

<table>
<tr><td colspan="7">Geometrical Parameters</td></tr>
<tr><td colspan="3">Length of link 1 (l_1)</td><td colspan="4">0.5 m</td></tr>
<tr><td colspan="3">Length of link 2 (l_2)</td><td colspan="4">0.5 m</td></tr>
<tr><td colspan="3">Distance of the c.o.m G_1 from the first joint (d_1)</td><td colspan="4">0.25 m</td></tr>
<tr><td colspan="3">Distance of the c.o.m G_2 from the second joint (d_2)</td><td colspan="4">0.25 m</td></tr>
<tr><td colspan="3">Radius of link 1</td><td colspan="4">0.1 m</td></tr>
<tr><td colspan="3">Radius of link 2</td><td colspan="4">0.1 m</td></tr>
<tr><td colspan="7">Inertial Parameters</td></tr>
<tr><td colspan="3">Mass of link 1 (l_1)</td><td colspan="4">20 kg</td></tr>
<tr><td colspan="3">Mass of link 2 (l_2)</td><td colspan="4">10 kg</td></tr>
<tr><td colspan="7">Control Parameters</td></tr>
<tr><td>Gain Set</td><td>K_{p1} (Nm/rad)</td><td>K_{hd1} (Nms$^{1/2}$/ rad)</td><td>K_{d1} (Nms/rad)</td><td>K_{p2} (Nm/rad)</td><td>K_{hd2} (Nms$^{1/2}$/ rad)</td><td>K_{d2} (Nms/rad)</td></tr>
<tr><td>a (PD)</td><td>189.38</td><td>0.00</td><td>72.34</td><td>21.46</td><td>0.00</td><td>8.20</td></tr>
<tr><td>b (PDD$^{1/2}$)</td><td>189.38</td><td>20.00</td><td>77.26</td><td>21.46</td><td>2.20</td><td>8.76</td></tr>
<tr><td>c (PDD$^{1/2}$)</td><td>189.38</td><td>50.00</td><td>83.33</td><td>21.46</td><td>5.60</td><td>9.44</td></tr>
<tr><td>d (PDD$^{1/2}$)</td><td>189.38</td><td>100.00</td><td>90.90</td><td>21.46</td><td>11.60</td><td>10.30</td></tr>
<tr><td>e (PDD$^{1/2}$)</td><td>189.38</td><td>200.00</td><td>113.25</td><td>21.46</td><td>22.70</td><td>12.83</td></tr>
</table>

ISSN 1590-8844
International Journal of Mechanics and Control, Vol. 10, No. 01, 2009

The errors of the two internal coordinates are the inputs of the PDD$^{1/2}$ control loops of the two actuators. Starting from the actuator torques, the robot dynamics determines the time history of the internal coordinates.
The behaviour of this system has been assessed by simulation using the Matlab-Simulink platform; the geometrical, inertial and control parameters are summarized in Table III. The robot links are considered cylinders with uniform density.
The control parameters have been selected using the same criteria adopted for the second-order linear system in section 3:

- the proportional gain K_p of both the PD and the PDD$^{1/2}$ controls is defined as function of the desired natural angular frequency ω_n, see Eq. (6): for the actuator 2 the inertia of the link 2 is considered; for the actuator 1 the inertia of the two links, rigidly connected with q_2=0, is considered; for both the actuators ω_n = 5 rad/s
- the output saturation value τ_{max} is defined by the maximum angular acceleration α_{max} , see Eq. (7); for both the actuators, $\alpha_{max} = 2\pi$ rad/s^2
- once selected the value of K_{hd} the derivative gain K_d is determined choosing its minimum value that provides a stabilization without overshoot in presence of a step of θ_r

Five different gain sets are compared, characterized by the same values of ξ and γ adopted for the one-degree-of-freedom second-order linear system (Table I); the gains of actuator 1 are equal to the case of section 3 because the overall moment of inertia of the two rigidly aligned links is equal to the inertia of the linear system of section 3. The control sampling time is T = 0.01 s. Since the values of ξ, γ, ω_n, α_{max} are common for the two actuators, the time histories of q_1 with q_2 constantly zero (rigidly connected links) and of q_2 with q_1 constantly zero (link 1 fixed to ground) are equal to the one of Figure 2, for the same commanded step.

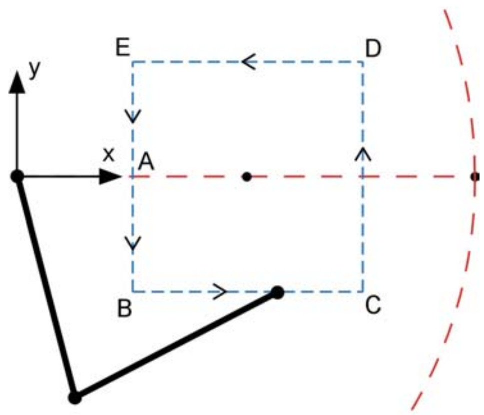

Figure 6 Simulation trajectory

The behaviour of the whole robot is assessed considering the square reference trajectory ABCDEA (Figure 6) with side $l = l_1 = l_2$.
The coordinates of the main trajectory points are collected in Table IV. This trajectory is followed by the robot with constant speed; the tracking error with the five gain sets is shown in Figures 7 to 9 for different end-effector speeds (0.1 m/s, 0.2 m/s, 0.4 m/s).

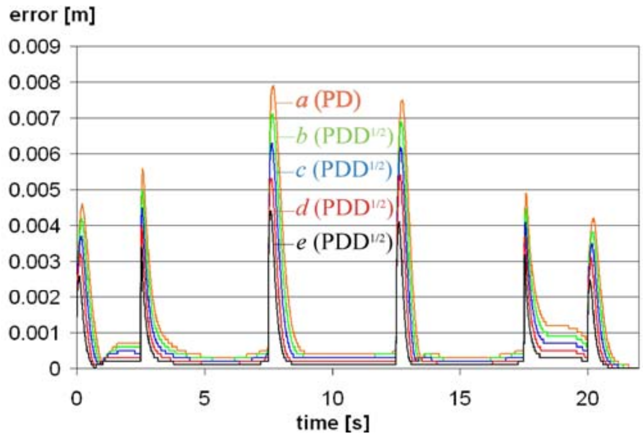

Figure 7 Tracking error (end-effector speed = 0.1 m/s)

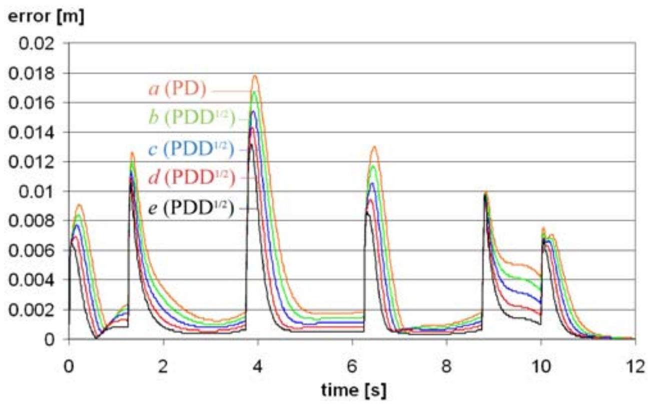

Figure 8 Tracking error (end-effector speed = 0.2 m/s)

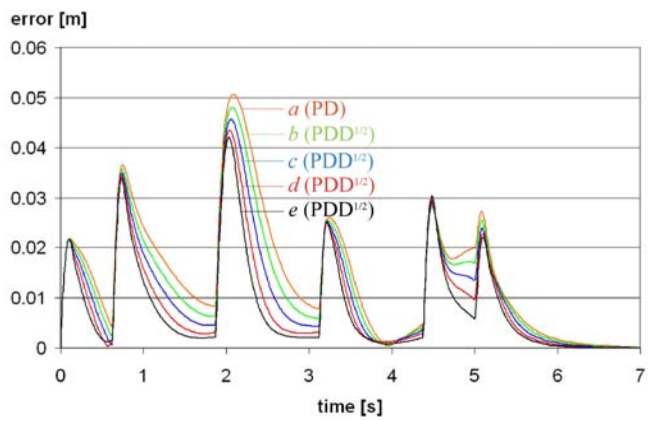

Figure 9 Tracking error (end-effector speed = 0.4 m/s)

Figure 10 shows the time integral of the tracking error along the whole trajectory. It is possible to note that the half-derivative term allows to reduce remarkably the tracking error, thanks to the lower settling time of each actuator.

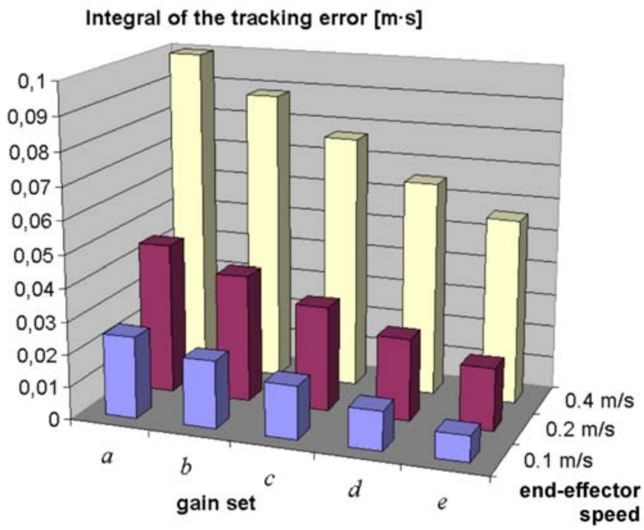

Figure 10 Time integral of the tracking error

5. CONCLUSIONS

The applications of the proposed $PDD^{1/2}$ discrete-time control algorithm to a single d.o.f. second-order linear system and to a 2R robot lead to interesting results. For the single d.o.f. system the introduction of the half-derivative term allows to reduce considerably the settling time with respect to a PD control, under the same limitations of maximum torque and null overshoot; this results in a decrease of tracking error in the position control of the 2R robot.
This preliminary study shows the great potential of the application of the fractional calculus to the control of robots and mechatronic devices. In particular, the proposed $PDD^{1/2}$ algorithm is a simple way to improve the performance of the PD control without revolutionize completely the classical approach.
In the following of the work several issues will be examined: the extension to the $PIDD^{1/2}$ scheme, the application to more complex robotic architectures, the introduction of the $PIDD^{1/2}$ scheme within more complex position and force control schemes, the control stability in presence of disturbances and non-linear friction effects.

6. ACKNOWLEDGEMENTS

The authors would like to acknowledge the precious help of Professor J.A. Tenreiro Machado of the Institute of Engineering of Porto.

7. REFERENCES

[1] Miller K. S. and Ross B., *An Introduction to the Fractional Calculus and Fractional Differential Equations*. John Wiley & Sons, 1993.

[2] Podlubny I., *Fractional Differential Equations*. Academic Press, San Diego, 1999.

[3] Oldham K. B. and Spanier J., *The fractional calculus: theory and application of differentiation and integration to arbitrary order*. Academic Press New York, 1974.

[4] Hilfer R., *Applications of Fractional Calculus in Physics*. World Scientific Singapore, 2000.

[5] Anastasio T.J., *The fractional-order dynamics of brainstem vestibulo-oculomotor neurons*. Biological cybernetics, Vol. 72, No. 1, pp. 69-79, 1994.

[6] Oustaloup A., *Fractional order sinusoidal oscillators: optimization and their use in highly linearFM modulation*. IEEE Transactions on Circuits and Systems, Vol. 28. No. 10, pp. 1007-1009, 1981.

[7] Ozaktas H.M., Arikan O., Kutay M. A. and Bozdagi G., *Digital computation of the fractional Fourier transform*. IEEE Transactions on Signal Processing, Vol. 44, No. 9, pp. 2141-2150, 1996.

[8] Machado J.A.T., *Analysis and design of fractional-order digital control systems*. SAMS Journal Systems Analysis, Modelling, Simulation, Vol. 27, No. 2-3, pp. 107–122, 1997.

[9] Machado J.A.T., *Discrete-time fractional-order controllers*. FCAA Fractional Calculus and Applied Analysis, Vol. 4, No. 1, pp. 47–66, 2001.

[10] Vinagre B. M., Podlubny I., Hernandez A. and Feliu V., *Some approximations of fractional order operators used in control theory and applications*. FCAA Fractional Calculus and Applied Analysis, Vol. 3, No. 3, pp. 231–248, 2000.

[11] Podlubny I., *Fractional-order systems and* $PI^{\lambda}D^{\mu}$*-controllers*. IEEE Transactions on Automatic Control, Vol. 44, No. 1, pp. 208–213, 1999.

[12] Ferreira N.M.F., Machado J.A.T. and Cunha J.B., *Fractional-order position/force robot control*. Journal of Advanced Computational Intelligence and Intelligent Informatics, Vol. 9, No. 4, pp. 379-385, 2005.

[13] Silva M.F. and Machado J.A.T., *Fractional order* PD^{α} *joint control of legged robots*. Journal of Vibration and Control, Vol. 12, No. 12, pp. 1483-1501, 2006.

[14] Machado J.A.T., *Fractional-order derivative approximations in discrete-time control systems*. Journal of Systems Analysis-Modelling-Simulation, Vol. 34, No. 4; pp. 419-434, 1999.

[15] Craig J. J., *Introduction to robotics: Mechanics and Control*. Prentice Hall, Upper Saddle River, NJ, 2005.

ISSN 1590-8844
International Journal of Mechanics and Control, Vol. 10, No. 01, 2009

ROBOTICS TECHNIQUES FOR DATA ACQUISITION IN UNDERWATER ARCHEOLOGY

G. Conte*§ S. M. Zanoli*§ D. Scaradozzi *§ A. Caiti**§

*Dipartimento di Ingegneria Informatica, Gestionale e dell'Automazione, Università Politecnica delle Marche - Ancona, Italy

**Dipartimento Sistemi Elettrici e Automazione, Università di Pisa – Pisa, Italy

§ Interuniversity Centre for Integrated Systems for the Marine Environment (ISME) – Genova, Italy

ABSTRACT

The paper presents a procedural methodology for the cooperation, at various level, of UUV and human operators to extract, in a non invasive way, as much information as possible from an underwater archaeological site with minimal expenditure of time and resources. Traditional methodologies of exploration of underwater archaeological sites have been enhanced thanks to new technologies and the possibility given to the archaeologist to promptly have a global information about the whole area of interest. In particular, in the paper, techniques for constructing augmented maps of the sites are illustrated. In the present approach, augmented maps are made accessible in real time to the archaeologist supervisor by means of a friendly interface. This allows to inform promptly the operators about the actual progresses of the survey, so that corrective actions can be eventually triggered on line. Furthermore, the possibility to contextualize the present survey data on wider scale maps (GIS) significantly enhances the global situation awareness of the archaeologists by pointing out correlations with the territory and with other sites. The experiences gathered on several missions on different archaeological sites have confirmed that the developed procedures guarantee an efficient and cost effective automation of the marine archaeologists' work.

1. INTRODUCTION

Over the past fifty years, underwater archaeology has seen an increasing growth: scuba-diving archaeologists have made many significant discoveries in shallow water, while, more recently, advanced (expensive) technologies has been used to investigate shipwrecks in much deeper water [1], [2], [3], [4]. The emphasis in the present research activity is mainly in developing, testing and validating solutions, based on the use of unmanned robotic vehicles and automatic procedures, that provide the archaeologists with new means for simplifying their work and for making accessible deep water sites that are not reachable by divers. The idea is that of developing procedural methodologies which exploit cooperation between archaeologists and engineers in order to optimize the survey process through automation.

A primary interest of the archaeological investigation is to extract, in a non invasive way, as much information as possible from a site with minimal expenditure of time and resources. In general, this is done by taking photos and measurements of objects and terrain, which are then used to construct representations of the site in form of local maps. In the underwater environment, this activity is traditionally performed by divers, but progressively, thanks to the technological advances divers can be substituted by unmanned underwater vehicles; in particular Remotely Operated Vehicles (ROVs), mainly employed in the off-shore industry, appear to be appropriate for this task, increasing substantially the efficiency of the process and

Contact author: Silvia M. Zanoli, *s.zanoli@univpm.it*

Work partially supported by the European Community under the European Research Network EPOCH (Research Project UPGRADE – Contract N. IST-2002-507382)) and under project VENUS (Contract IST-034924) of the "Information Society Technologies (IST) of the "Information Society Technologies (IST) program of the 6th FP for RTD". The authors are solely responsible for the content of this paper. It does not represent the opinion of the European Community, and the European Community is not responsible for any use that might be made of data appearing therein.

ISSN 1590-8844
International Journal of Mechanics and Control, Vol. 10, No. 01, 2009

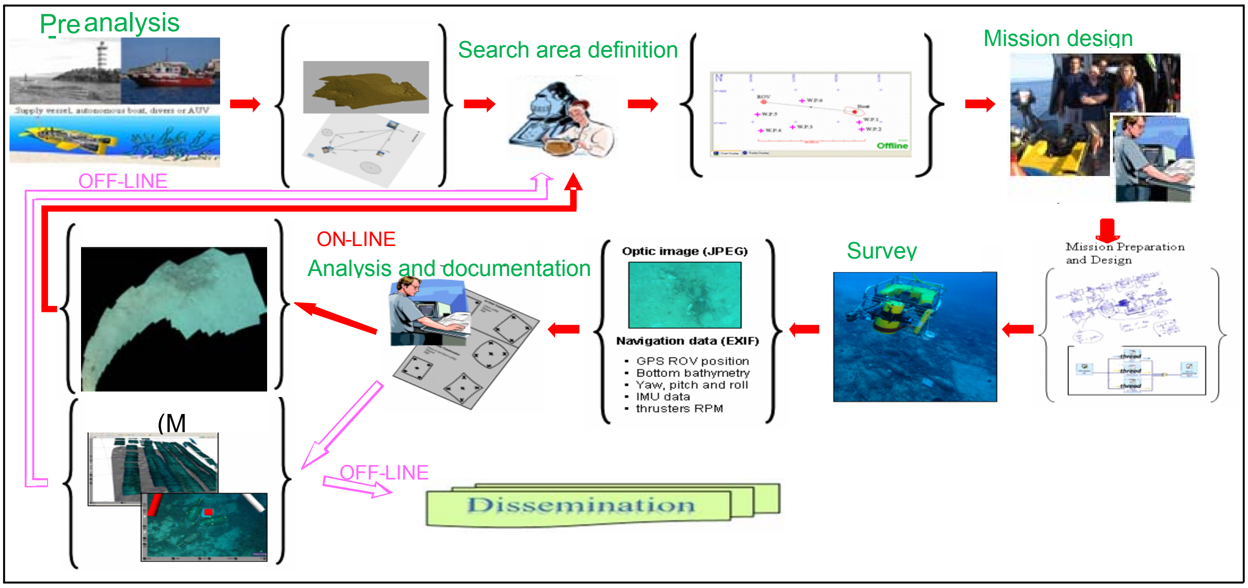

Figure 1 The activities flow diagram characterizing the exploration of an underwater site by cooperating teams of archaeologists and engineers.

reducing, at the same time, costs and risks as described in [5], [6],[7],[8] and [9]. This has particular relevance for deep water archaeological sites, where the use of human divers is unfeasible or highly inefficient and dangerous due to physical constraints. Nevertheless, even in shallow water sites, the development of automated robotic methodology is be of great value, allowing to enlarge the number of better known sites. The main problems to deal with, on archaeological surveys, concern the navigation and guidance of the ROV [10] and the association, integration and fusion of data gathered by heterogeneous sensors (photo and video cameras, sonar, navigation sensors) for constructing informative local maps [5], [11], [12].
In this work, by structuring the data into a coherent set, it had been obtained adequate and sufficient information for accomplishing on-line (that is: during the survey) information transfer to the operators and/or to the archaeology's experts. Availability of information in form of local maps allows the archaeologists to modify, if needed, some of the mission's parameters (e.g. area coverage, point of interest, data density and so on) during operation, saving time and reducing costs (see [13], [14], [15], [16]). In other terms, the use of robotic vehicles and automatic procedures in substitutions of divers allows to implement a logical feedback loop, at the decisional level, in governing the survey process as described in Section 2. A description of the instrumentation adopted in the archaeological survey is given in Section 3. On-line construction of local maps of the explored site is performed by means of photomosaic techniques, which exploit the high data density achievable by employing automatic devices and procedures and the navigation data provided by the ROV's on-board sensors. In addition, the realization of a layered GIS (Geographic Information System) allows to display on-line the position of the ROV on (large) maps of the area, obtained through a Web Map Service, and to integrate into them the local maps constructed by photo-mosaicing. This gives to the archaeologists the possibility to evaluate in short time the results of the survey with respect to large geographical scenarios, facilitating the interpretation of local data and phenomena. The structure of the data processing, organized into three distinct levels which differ on data sets and its computational and time requirements are outlined in Section 4.
The above described procedures have been developed in the framework of the EU research projects VENUS and UPGRADE and further information can be found in [9], [12], [17], [18] [19] and [20] and on the websites www.venus-project.eu, www.epoch-net.org.

2 UNDERWATER SITE EXPLORATION

The major activities that define the work in marine archeological surveys include: pre-analysis of the area, definition of a restricted search area, mission design, local survey, documentation, excavation, post-analysis and final documentation. Our interest in the present research is concentrated on the phases which precede the excavation. Figure 1 depicts the activities flow diagram in case ROVs and automatic data gathering procedures are involved in the process.
The pre-analysis is meant for the specification of the search area. Information about archeological remains, in general, originates from heterogeneous sources and is as vague about the nature of the findings as about their localization, so that a broad area must be covered in this initial phase. In many situations, this is done from the surface, employing acoustic devices of various kinds (like multibeam and sidescan sonar) for scanning the sea bottom. The output of this activity is a preliminary map of the area, whose scale is large or very large in comparison to the objects of (possible) interest, which at this level are termed "anomalies".

From analysis of the preliminary map, archeologists define a more restricted search area and possibly identify waypoints and targets that deserve special attention.
The following phase is devoted to design the survey mission, keeping into account the above information and the characteristics of the system, comprising the robotic vehicle(s), the sensory apparatus and the supply vessel(s), to be used (in terms e.g. of maneuverability, payload capability, degree of autonomy), as well as possible environmental constraints (depth, visibility, presence of current, tides and so on).
Then, local survey takes place, according to the data gathering modalities and to the navigation and control settings defined in the previous phase. In the basic execution mode, the ROV performs a number of transects at a given speed and average distance from the sea bottom, collecting photos, videos and acoustic images of the area. At this level, the relevant feature of the proposed methodology is the possibility of providing a preliminary local map of the site on-line, as indicated in Figure 1, closing a first logical feedback loop in the decisional process that governs the mission execution. In practice, the archaeologists can check the area coverage and the possible presence of unexpected features, which may deserve a deeper investigation, and change accordingly the search modality and/or the parameters of the mission. It has to be stressed that the possibility of providing on-line the results of the survey modifies substantially the standard way to operate in underwater archaeology, increasing largely efficacy and efficiency with respect to the current state of the art. The distinctive feature of the proposed methodology is the activation of a feedback loop, which includes and exploits the domain knowledge of archaeologists. This is obtained by a more profitable use of information through the integration of a number of technologies, which allow the data gathering, handling and online processing of a large amount of data.
A second logical feedback loop is closed off-line, as indicated in Figure 1; more accurate off-line, strict time constraints can be relaxed and more accurate algorithms can be applied. As it will explained in the paper, data gathered from the site are processed at various levels with different techniques which may differ greatly on the processing time and on the data set considered.

3 EQUIPMENT DESCRIPTION

The vehicle used to validate the above described procedure is a small class DOE Phantom S2 Remote Operated Vehicle (ROV), operated from a support vessel. The on-board navigation sensory system consists of a depth meter, a compass and an inertial measuring unit (Crossbow DMU VGX) that evaluates linear accelerations and angular velocities along and around three axes. In the present application, the Inertial Measuring Unit (IMU) has been employed mainly to evaluate the ROV’s pitch and roll. Pitch and roll data have been used on-line to construct an artificial horizon that enhances the situation awareness of the operator and to evaluate the ROV’s attitude while taking pictures. The ROV carries a full HD video camera and an imaging sonar Kongsberg-Symrad MS 1000. Furthermore, in a series of missions, different high precision optical sensors were installed and tested (Nikon D2Hs camera equipped with 4.1 mega-pixels 'JFET sensor', capable of capturing eight frames per second, Nikon 200, Nikon 300).
The ROV position is acquired by an Ultra Short Base Line (USBL) system consisting of a Sonardyne Scout USBL system. In particular, acoustic measurements are used to locate the ROV with respect to the transceiver head of the USBL subsystem, mounted on a supply vessel, whose position in the terrestrial coordinate system is obtained by a Differential GPS subsystem. By combining acoustic measurement and DGPS measurements, the position of the ROV in the terrestrial coordinate system is obtained with an accuracy of about 2.75% of the distance from the supply vessel and with an acquisition rate of 1Hz.
The ROV and its sensory apparatus is governed by a Navigation, Guidance and Control (NGC) system implemented on a PXI/FPGA/PC station. Its structure, by means of a virtual reconfigurable Man/Machine interface, allows switching from manual guidance performed through a console to automatic guidance achieved using navigation sensors data [9]. At low level, an onboard real-time microcontroller (Freescale 68K/Coldfire RISC MicroController) takes care of interfacing the additional optical and acoustic sensors (photo/video-camera and sonar) with the NGC system. The NGC system processes all the data coming from the sensors and from the USBL positioning system and it assists the operator in guiding the ROV, by implementing auto-depth and auto-heading functions.

4 DATA FROM THE ARCHAEOLOGICAL SITE

As described in section two, at each mission the ROV performs a number of transects in accordance with the navigation and control specifications as resulting from the mission tasks and from system and environmental constraints. Typically, it proceeds at low speed in the horizontal plane, maintaining a constant depth while collecting photos, videos and acoustic images of the area. Possible depth corrections can be performed accounting for sea bed morphology so to follow the contour line relative to sea-bottom and acquire images from a constant height with respect to it; both video and high resolution still images are captured. Navigation data from eteroceptive and proprioceptive sensors (compass, depth meter, IMU, imaginig sonar), are acquired and memorized in real time on an industrial PC (National Instrument-PXI) onboard the surface vessel. An acoustic positioning system, a USBL (Ultra Short Base Line) correlated with the global positioning system (GPS) eventually with differential correction (DGPS) allows evaluating position of the vehicle over time. Different acquisition rates apply to each sensor but the internal clocks, which each rate is referred to, are

ISSN 1590-8844
International Journal of Mechanics and Control, Vol. 10, No. 01, 2009

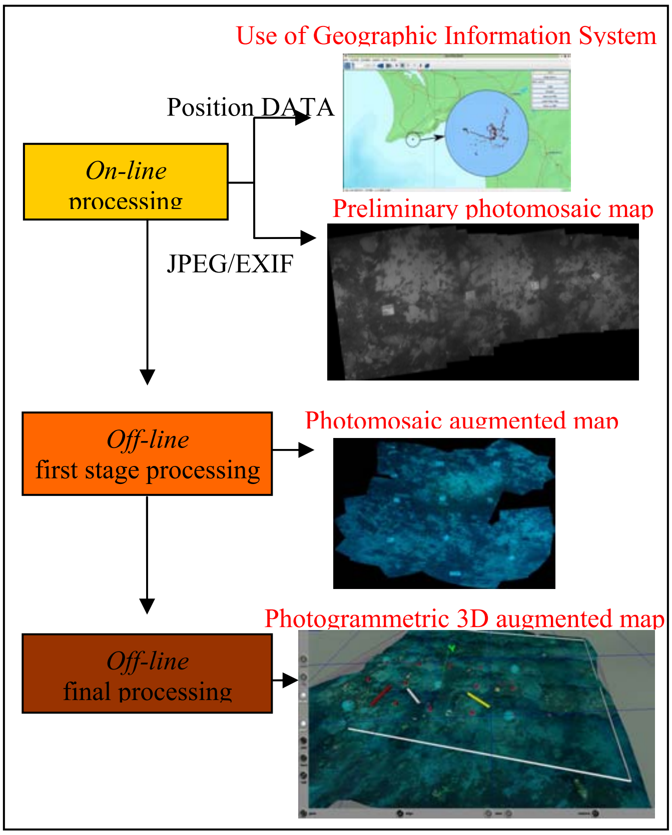

Figure 2 The three levels processing structure.

synchronized to a signal generated by the PCI unit (see section 3) according to the GMT satellite time. In this way, all data can be consistently processed so to extract relevant information about ROV position and attitude and reconstruct its trajectory.
Data processing takes place at three distinct levels (see Figure 2): at the first on-line level, fast processing procedure are performed and draft information of the site is produced (see Figure 3); at the end of each daily survey more accurate algorithms (offline-first stage level) are executed which further elaborate the previous data while considering additional available data stored locally onboard vehicle's memory units; ultimately, the third processing level (offline-final level) takes place only at the completion of the whole mission and considers the entire data set gathered in the various days of surveys (see Figure 4).
The motivations for the first two levels originate from the need to promptly inform the operators and the archaeologists' supervisors on the actual progresses of the survey so that corrective actions can be eventually triggered on line, during the actual ROV survey, from inspection of the online level processing, or eventually on the next survey, after having analysed the data processed on the offline-first stage.
Online output data are in the form of a "snake" photomosaic map and of Geographic Information System (GIS) layers which display ROV survey trajectory data on topological maps area. The possibility to contextualize the

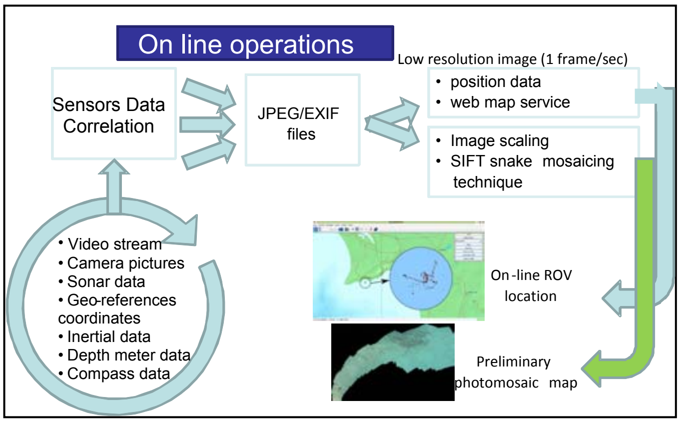

Figure 3 *Online* processing level's operations.

present survey data on wider scale (GIS) maps where additional data from previously explored archaeological sites are possibly displayed, pointing out correlations with the territory and with other sites, significantly enhances the global situation awareness of the archaeologists.
At the offline-first stage processing level, more accurate photomosaic maps are computed. The previous maps can form additional layers of the GIS, which can be completed by inclusion of 3D maps, derived from the mosaic maps with the aid of sonar data and photogrammetric techniques in a further subsequent off-line processing (off-line final processing), which, depending on data quality, may take a relatively long computational time [18], [20]. In this last phase, additional information can be added to generate augmented maps. In general, one can add information gathered on the site (concerning e.g. characteristics of the sea bottom or of specific objects revealed by their acoustic response, or the presence of buried objects eventually detected by sub-bottom profilers) or extracted from databases and libraries (like e.g. information on the characteristics of recognized artefacts).
The three level process which leads from raw data to the final augmented maps is represented in Figure 2; here pictures refer to recent survey missions (in the Atlantic Ocean, at the mouth of Sado River in Portugal, and the Tyrrhenian Sea, near the Island of Pianosa in Italy).

4.1 PHOTOMOSAIC MAPS

Data collected by the different sensors are correlated, by associating pictures together with acoustic images and

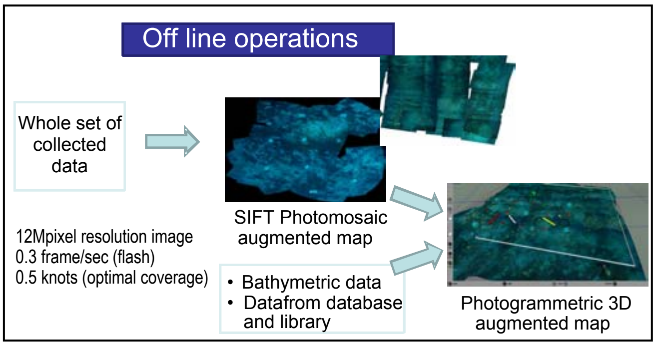

Figure 4 *Offline* (*fist and final stage*) processing operations.

ISSN 1590-8844
International Journal of Mechanics and Control, Vol. 10, No. 01, 2009

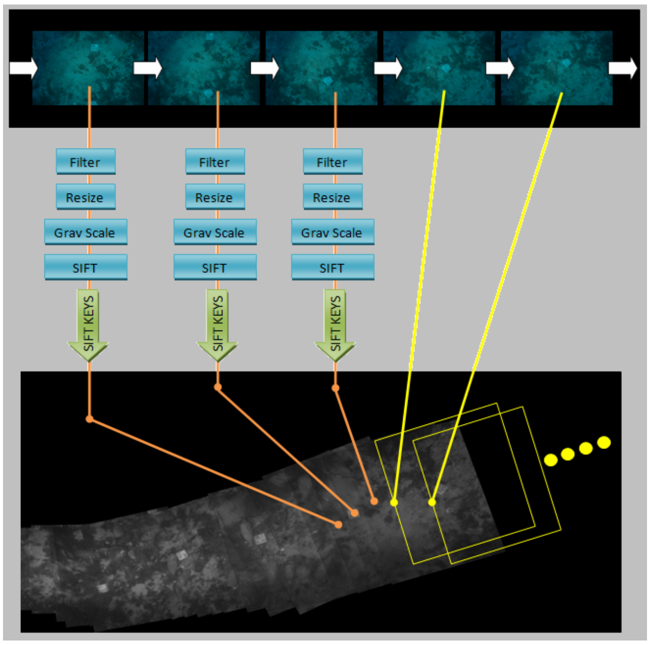

Figure 5: Scale Invariant Feature Transform (SIFT) procedure applied to the temporal-image sequence; pairwise keypoint detection is performed on grayscale subsequent images

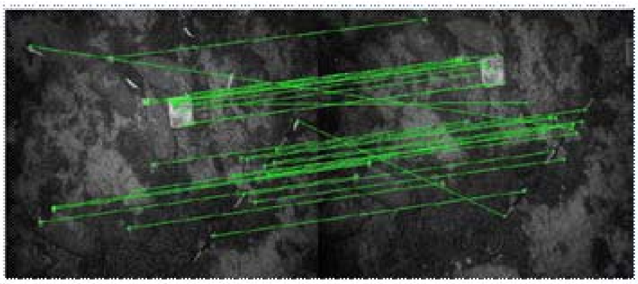

Figure 6: Example of key point matching of two subsequent images.

measures taken by the navigation sensors. In this way, a set of files in JPEG/EXIF format is produced online and made directly accessible to the operators.

The association process is performed *online* accounting for the different acquisition rates of each sensor. Pictures sampled from the video stream (relatively low quality pictures) are associated with sonar's acoustic images that exhibit the closest timestamp. Sonar data are processed in order to enhance signal-to-noise ratio and eliminate false returns. Association with other data, such as geo-referenced coordinates or attitude data, requires supplementary calculations, which may include averaging, interpolation or filtering according to the update rate and other characteristics of the sensor and of the produced signal.

In particular, the position data coming from the USBL positioning system is the result of a Kalman filtering process that produces about one measurement each second with a computable delay d (given by $d=m/v$, where $m=(x^2+y^2+z^2)^{1/2}$ is the slant range and v is the sound's speed

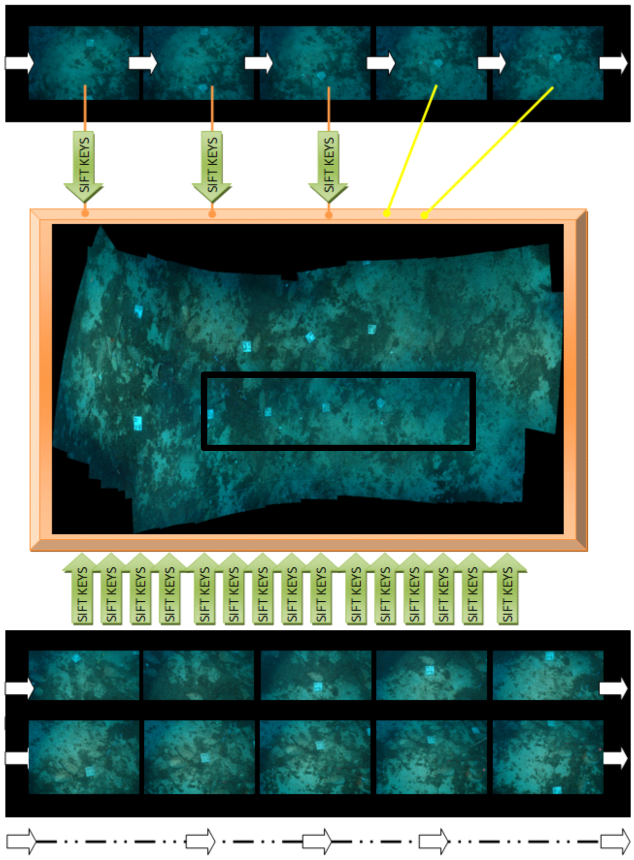

Figure 7: Global Mosaic construction. The rectangle refers to the data shown on Figure 5.

in water). Taking into account the delay and the timestamp, position data are associated to each sampled image.

Attitude data and depth measurements, beside being recorded for possible further processing, are averaged over a short period around each photo's timestamp and the result of the averaging is associated to each photo, in order to describe camera's attitude and depth at the shooting time.

In the local map's construction phase (*on-line* processing), images are processed sequentially, in the same order they are acquired. In particular, a Scale Invariant Feature Transform (SIFT) procedure [21] is first applied to the temporal-image sequence and used to perform pairwise keypoint detection on subsequent images. In order to speed up the processing, position and attitude data contained in the EXIF area, together with the distance from the sea bottom elaborated from the sonar returns, are used to orient and scale the associated image contained in the JPEG area as shown in Figure 5. Furthermore, images are converted to grey scale images not taking into account saturation and hue information. The choice to apply a SIFT operator is motivated by the fact that, been the SIFT detector invariant to image translation, scaling, and rotation, and partially invariant to illumination changes and affine or 3D projection is well suited to underwater images' feature extraction. By comparing SIFT output keypoints of two subsequent images I_k and I_{k-1} it is then possible to create real-time mosaics based on SIFT: common key points are found, as shown in Figure 6, and on each couple of matched keys and relative image points, p_k p_{k-1}, an optimum problem can be formulated as:

$$p_k = \begin{bmatrix} x \\ y \\ 1 \end{bmatrix} \in I_k \quad p_{k-1} = \begin{bmatrix} x \\ y \\ 1 \end{bmatrix} \in I_{k-1} \qquad (1)$$

$$min_T \; T \; p_k - p_{k-1}$$

where T is an image space-transformation matrix. In this way, a growing "snake" mosaic is solved after each new image is added. The inspection of this growing map allows the mission operators to check for the total and correct coverage of the inspected area and the archeologists to verify the validity of the detected findings while possibly discovering new characteristic of the site worthy of further investigation.
At a later stage (offline- first stage processing), all the data previously acquired are processed again, this time by considering their totality, in order to contrast error growth due to sequential processing. Low quality images grabbed from the video stream are replaced by high quality photos downloaded from the camera internal compact flash memory. In this off-line phase of processing, more accurate local maps can be generated by the application of mosaicing techniques which account for all overlap information, including overlap from images that are not consecutive in time. The position and attitude data contained in the EXIF area can be used for establishing correlation between images by grouping those taken (not necessarily sequentially) from close positions and, presumably, depicting overlapping areas of the sea bottom. The result of this processing is shown in Figure 7. Although not performed on-line, this *first-stage* processing takes a relatively short computational time and its product can be made available shortly after the whole set of data has been gathered.

4.2 GIS MAPS

As stated in the previous, from the experience gained from the field activity, it has become evident that to enhance the efficiency of underwater archaeological surveys a crucial role is played by the active *in-the-loop* cooperation of archaeologists. This has motivated the activation of the three different processing levels; in particular, at the *online* processing level, the archaeologist is called for a prompt active interaction during the survey progress. To perceive this scope a Geographic Information System (GIS) [22] has been used which allows to acquire, store and return in graphic and alphanumeric form data referred to a territory. In particular, the open source OpenMap package has been exploited to provides a means to see and manipulate geospatial information.
A new layer on OpenMap has been developed which provides the access to the information acquired during the site inspection and recorded by the Scout USBL/DGPS positioning system, such as the ROV's, the surface vessel's and the archaeological site's position coordinates.

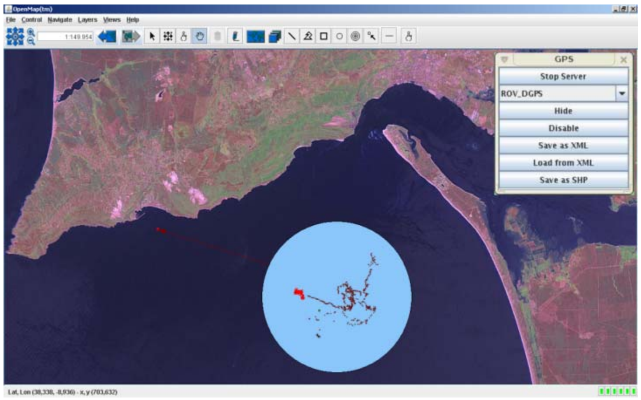

Figure 8: Vessel position (in red) and ROV navigation data (in brown) layer displayed on OpenMAp; data refers the underwater survey held in Sesimbra in October 2007.

USBL data acquired from a RS232 port are exported, elaborated by a tool developed in the Matlab software environment and sent to OpenMap using the XML Client protocol. These acquired data are merged with geographic maps of the area; in particular the NASA world geographic archive (based on WMS protocol) was chosen in the past missions. An example of data displayed by GIS during Sesimbra mission in shown in Figure 8.
One of the main advantages of the GIS is that it helps in locating the site under survey and its archaeological findings in large geographical scenarios, pointing out correlations with the territory and, possibly, with other relatively distant sites.

5 CONCLUSIONS

Traditional methodologies for exploring underwater archaeological sites have been enhanced, in terms of quantity and quality of documentation, thanks to the use of new technologies and to the possibility given to archaeologists to access on-line to a global information about the whole surveyed area. On-line information consists of a preliminary 2D photomosaicing reconstruction of the site and of ROV survey trajectories' locations superimposed on wider area maps taken from the Web Map Service. The decisional process that governs the mission execution is structured with three different logical feedback loops, the first one resulting from the access to the on-line information above. In this respect, efficiency turns out to be greatly enhanced with respect to the traditional modality in which results of the survey are made available only after its conclusion.
ROV's performances in data acquisition differ from that of divers, in terms of data quantity and density, due to the time and depth limitations that affect divers. Physiological constraints limit human dives up to approximately, 60 m in depth; moreover intensification of physical strain, short dive duration, long decompressing time, all make the work inefficient. Furthermore, in contrast with surveys done by divers, the developed robotics procedure produces not only a collection of distinct optical imagines but augmented maps of the archaeological site through the processing and

synchronization of information acquired by different sensors. Finally, a wider and more uniform coverage of the site can be obtained in shorter time by the use of robots.

At the same time, some aspects of the proposed methodology needs to be improved. In particular, the presence of protrusions in rocks or in submersed finds as well of ropes or other floating objects may put at risk ROV integrity and limit its use. Better suited navigation and guidance techniques need to be developed for these particular cases. Moreover efficient procedures and equipment for handling the difficulty of gathering informative data on rough terrain (i.e. finds deployed on heaps) need to be developed.

REFERENCES

[1] Ballard R.D., High-tech search for Roman shipwrecks. *National Geographic Magazine* 193 4, pp. 32–4, 1998.

[2] Ballard R.D., McCann A.M., Yoerger D.R., Whitcomb L.L., Mindell D. A., Oleson J., Singh H., Foley B., Adams J., and Piechota D., The Discovery of Ancient History in the Deep Sea Using Advanced Deep Submergence Technology, Deep Sea Research, Deep Sea Research I, 47, pp 1591-1620, 2000.

[3] Ballard R.D., Stager L.E., Master D., Yoerger D.R., Mindell D., Whitcombe L.L., Singh H. and Piechota D., Iron age shipwrecks in deep water off Ashkelon, Israel. Am. *J. Archaeology*, Vol. II, pp. 151-168, 2002.

[4] Singh H, Adams J., Foley B.P. Mindell D., Imaging for Underwater Archaeology, *American Journal of Field Archaeology*, pp. 319-328, vol 27, no 3, 2000.

[5] Mindell D., Bingham B. New Archaeological Uses of Autonomous Underwater Vehicles. *Proceedings MTS/IEEE Conference Oceans* 2001, 2001.

[6] Mindell D., Recent advances in precision measurements and survey for underwater sites *Proceedings of the Conference on Recent advances in Underwater Detection and Survey Techniques to Underwater Archaeology*, Bodrum, Turkey, 2004.

[7] Vettori G., Gambogi P., Rizzerio A., Casalino G., and Caiti A., Recent experiences in archaeological surveys with Remotely Operated Vehicles in the North Tyrrhemian Sea - *Proceedings of the Conference on Recent advances in Underwater Detection and Survey Techniques to Underwater Archaeology*, Bodrum, Turkey, 2004.

[8] Caiti A., Conte G., Casalino G. and Zanoli S.M., Underwater archaeology: available techniques and open problems in fully automated search and inspection. *Workshop on Innovative Technologies for Underwater Archaeology*, Prato, Italy, 2004.

[9] Caiti A., Conte G., Casalino G. and Zanoli S.M., Innovative technologies in underwater archaeology: field experience, open problems, research lines. *Chemistry and Ecology*, Vol. XXII, pp. S383-S396, 2006.

[10] Conte G, Zanoli S.M., Scaradozzi D. and Maiolatesi S., ROV Positioning by Visual Feedback. *Conf. on Recent advances in Underwater Detection and Survey Techniques to Underwater Archaeology*, Bodrum, Turkey, 2004.

[11] Conte G., Zanoli S. M., Scaradozzi D. and Gambella L., Underwater Archaeological Data Collection by means of ROVs. *IFAC Proceedings CAMS* 2006, Ancona, Italy, 2006.

[12] Conte G., Zanoli S.M., Scaradozzi D., Gambella L., Caiti A., Data Gathering in Underwater archaeology by Means of a Remotely Operated Vehicle. *XXI CIPA International Symposium*, 01-06 October , Athens, Greece, 2007.

[13] Gambogi P., Progetto "Baratti 2001": Uso di tecnologie avanzate nella ricerca di giacimenti archeologici sottomarini. *2nd Nat. Conf. Underwater Archaeology*, Castiglioncello, Italy, 2003.

[14] Vettori G., Gambogi P., Rizzerio A., Casalino G., Caiti A., Recent experiences in archaeological surveys with remotely operated vehicles in the North Tyrrhemian Sea. *Conf. of Recent advances in underwater detection and survey techniques to underwater archaeology*, Bodrum, Turkey, 2004.

[15] Zanoli S., Conte G., Scaradozzi D., Gambella L., Caiti A., Procedures for cooperative human-UUV missions in underwater data gathering, in *UUST International Symposium*, August, Durham, NH, USA, 2007.

[16] Conte G., Zanoli S.M., Scaradozzi D., Gambella L., Calabrò V., Underwater Archeology Missions Design for Data Gathering Automation – *Proceedings MED'08*, Ajaccio, France, 2008.

[17] Drap P., Chapman P., Conte G., Pascoal A.M., Gambogi P., Gauch F., Hanke K., Long L., Loureiro V., Papini O., Richards J., Roussel D., VENUS, Virtual ExploratioN of Underwater Sites, *Proceedings XX CIPA / VAST*, Nicosia, Cyprus, 2006.

[18] Drap P., Scaradozzi D., Gambogi P., Long L., Gauche F., Photogrammetry for Virtual Exploration of Underwater Archeological Sites. In: *XXI CIPA International Symposium*, Athens, Greece, 2007.

[19] Drap P. et al., VENUS – Two years of interdisciplinary collaborations, *Proceedings of VSMM 2008*, Cyprus, 2008.

[20] Drap P. et al., Underwater cartography for archaeology in the VENUS project - *Geomatica*, Vol. 62, 2008.

[21] Lowe D.G., Object recognition from local scale-invariant features, Proc. *ICCV 1999*, Corfu, Greece 1999.

[22] Heywood I., Cornelius S., and Carver S., *An Introduction to Geographical Information Systems*. Prentice Hall. 3rd edition, 2006.

TEMPLATE FOR PREPARING PAPERS FOR PUBLISHING IN INTERNATIONAL JOURNAL OF MECHANICS AND CONTROL

Author1* Author2**

* affiliation Author1

** affiliation Author2

ABSTRACT

This is a brief guide to prepare papers in a better style for publishing in International Journal of Mechanics and Control (JoMaC). It gives details of the preferred style in a template format to ease paper presentation. The abstract must be able to indicate the principal authors' contribution to the argument containing the chosen method and the obtained results. (max 200 words)

Keywords: keywords list (max 5 words)

1 TITLE OF SECTION (E.G. INTRODUCTION)

This sample article is to show you how to prepare papers in a standard style for publishing in International Journal of Mechanics and Control.
It offers you a template for paper layout, and describes points you should notice before you submit your papers.

2 PREPARATION OF PAPERS

2.1 SUBMISSION OF PAPERS

The papers should be submitted in the form of an electronic document, either in Microsoft Word format (Word'97 version or earlier).
In addition to the electronic version a hardcopy of the complete paper including diagrams with annotations must be supplied. The final format of the papers will be A4 page size with a two column layout. The text will be Times New Roman font size 10.

Contact author: author1[1], author2[2]

[1]Address of author1.

[2]Address of author2 if different from author1's address.

2.2 DETAILS OF PAPER LAYOUT

2.2.1 Style of Writing

The language is English and with UK/European spelling. The papers should be written in the third person. Related work conducted elsewhere may be criticised but not the individuals conducting the work. The paper should be comprehensible both to specialists in the appropriate field and to those with a general understanding of the subject.
Company names or advertising, direct or indirect, is not permitted and product names will only be included at the discretion of the editor. Abbreviations should be spelt out in full the first time they appear and their abbreviated form included in brackets immediately after. Words used in a special context should appear in inverted single quotation mark the first time they appear. Papers are accepted also on the basis that they may be edited for style and language.

2.2.2 Paper length

Paper length is free, but should normally not exceed 10000 words and twenty illustrations.

2.2.3 Diagrams and figures

Figures and Tables will either be entered in one column or two columns and should be 80 mm or 160 mm wide respectively. A minimum line width of 1 point is required at actual size. Captions and annotations should be in 10 point with the first letter only capitalised *at actual size* (see Figure 1 and Table VII).

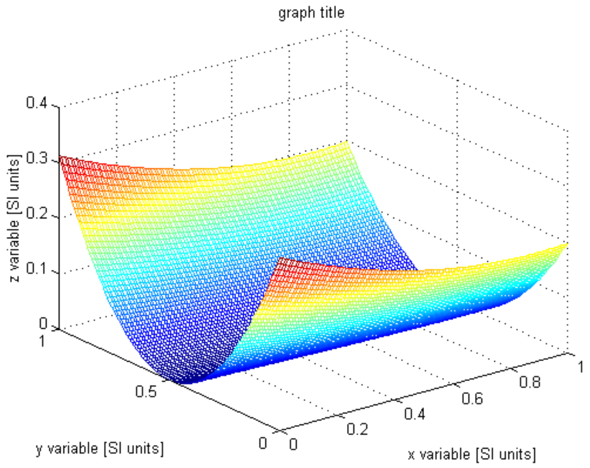

Figure 1 Simple chart.

Table VII - Experimental values

Robot Arm Velocity (rad/s)	Motor Torque (Nm)
0.123	10.123
1.456	20.234
2.789	30.345
3.012	40.456

2.2.4 Photographs and illustrations
Authors could wish to publish in full colour photographs and illustrations. Photographs and illustrations should be included in the electronic document and a copy of their original sent. Illustrations in full colour …

2.2.5 Equations
Each equation should occur on a new line with uniform spacing from adjacent text as indicated in this template. The equations, where they are referred to in the text, should be numbered sequentially and their identifier enclosed in parenthesis, right justified. The symbols, where referred to in the text, should be italicised.

- point 1
    - point 2
        - point 3

1. numbered point 1
    2. numbered point 2
        3. numbered point 3

$$W(d) = G(A_0, \sigma, d) = \frac{1}{T}\int_0^{+\infty} A_0 \cdot e^{-\frac{d^2}{2\sigma^2}} dt \quad (1)$$

3 COPYRIGHT

Authors will be asked to sign a copyright transfer form prior to JoMaC publishing of their paper. Reproduction of any part of the publication is not allowed elsewhere without permission from JoMaC whose prior publication must be cited. The understanding is that they have been neither previously published nor submitted concurrently to any other publisher.

4 PEER REVIEW

Papers for publication in JoMaC will first undergo review by anonymous, impartial specialists in the appropriate field. Based on the comments of the referees the Editor will decide on acceptance, revision or rejection. The authors will be provided with copies of the reviewers' remarks to aid in revision and improvement where appropriate.

5 REFERENCES (DESCRIPTION)

The papers in the reference list must be cited in the text. In the text the citation should appear in square brackets [ ], as in, for example, "the red fox has been shown to jump the black cat [3] but not when...". In the Reference list the font should be Times New Roman with 10 point size. Author's first names should be terminated by a 'full stop'. The reference number should be enclosed in brackets.
The book titles should be in *italics*, followed by a 'full stop'. Proceedings or journal titles should be in *italics.* For instance:

REFERENCES (EXAMPLE)

[1] Smith J., Jones A.B. and Brown J., *The title of the book*. 1st edition, Publisher, 2001.
[2] Smith J., Jones A.B. and Brown J., The title of the paper. *Proc. of Conference Name*, where it took place, Vol. 1, paper number, pp. 1-11, 2001.
[3] Smith J., Jones A.B. and Brown J., The title of the paper. *Journal Name*, Vol. 1, No. 1, pp. 1-11, 2001.
[4] Smith J., Jones A.B. and Brown J., *Patent title*, U.S. Patent number, 2001.

International Journal of Mechanics and Control – JoMaC
Published by Levrotto&Bella
TRANSFER OF COPYRIGHT AGREEMENT

NOTE: Authors/copyright holders are asked to complete this form signing section A, B or C and mail it to the editor office with the manuscript or as soon afterwards as possible.	*Editor's office address:* Andrea Manuello Bertetto Elvio Bonisoli *Dept. of Mechanics* *Technical University – Politecnico di Torino* *C.so Duca degli Abruzzi, 24 – 10129 Torino – Italy* *e_mail: jomac@polito.it* *fax n.: +39.011.564.6999*

The article title:

By:____

To be Published in ***International Journal of Mechanics and Control JoMaC***
Official legal Turin court registration Number 5320 (5 May 2000) - reg. Tribunale di Torino N. 5390 del 5 maggio 2000

A Copyright to the above article is hereby transferred to the JoMaC, effective upon acceptance for publication. However the following rights are reserved by the author(s)/copyright holder(s):
1. All proprietary rights other than copyright, such as patent rights;
2. The right to use, free or charge, all or part of this article in future works of their own, such as books and lectures;
3. The right to reproduce the article for their own purposes provided the copies are not offered for sale.
To be signed below by all authors or, if signed by only one author on behalf of all co-authors, the statement A2 below must be signed.

A1. All authors:

SIGNATURE____________________DATE________ SIGNATURE____________________DATE________

PRINTED NAME________________________ PRINTED NAME________________________

SIGNATURE____________________DATE________ SIGNATURE____________________DATE________

PRINTED NAME________________________ PRINTED NAME________________________

A2. One author on behalf of all co-authors:
"I represent and warrant that I am authorised to execute this transfer of copyright on behalf of all the authors of the article referred to above"

PRINTED NAME________________________

SIGNATURE____________________ TITLE____________________ DATE________

B. The above article was written as part of duties as an employee or otherwise as a work made for hire. As an authorised representative of the employer or other proprietor. I hereby transfer copyright to the above article to Editel-Pozzo Gros Monti effective upon publication. However, the following rights are reserved:
1. All proprietary rights other than copyright, such as patent rights;
2. The right to use, free or charge, all or part of this article in future works of their own, such as books and lectures;
3. The right to reproduce the article for their own purposes provided the copies are not offered for sale.

PRINTED NAME________________________

SIGNATURE____________________ TITLE____________________ DATE________

C. I certify that the above article has been written in the course of employment by the United States Government so that no copyright exists, or by the United Kingdom Government (Crown Copyright), thus there is no transfer of copyright.

PRINTED NAME________________________

SIGNATURE____________________ TITLE____________________ DATE________

CONTENTS

next number scheduled titles:

Dynamic And Energy Analysis of a Production System of Filament Wound Elbows
G. Dionoro, P. Buonadonna and A. Tronci

Design and Simulation of Cassino Hexapode Walking Machine
G. Carbone, M. Suciu, M. Ceccarelli and D. Pisla

Robot Assisted Laser Scanning
C. Rossi, S. Savino and S. Strano

Evaluation of Feasibility of Mechanical Harvesting of Myrtle Berries (Myrtus Communis L.)
F. Gambella and F. Paschino

Nonlinear Elastic Characteristic of Magnetic Suspensions through Hilbert Transform
E. Bonisoli